Dynamic Manipulations of Interacting 1d Bose Gases

Gal Aviv, MSc Phys.

Thesis submitted to the University of Nottingham
for the degree of Doctor of Philosophy

31.08.2013

Head of School
Prof. Richard Bowtell

Advisors
Prof. Peter Krüger
Dr. Thomas Fernholz

Referees
Prof. Igor Lesanovsky
Dr. Dimitri Gangardt

Date of the graduation
03.03.2014

Abstract

Dynamic Manipulations of Interacting 1d Bose Gases

Atom chips are a great tool for creation of low dimensional magnetic trapping geometries via micro-structures on the chip surface. Such structures allow the creation of time-dependent magnetic and electric potentials with highly accurate spatial and temporal dependency.

As part of this thesis we have investigated the coherence dynamics in one-dimensional Bose-Einstein condensate while creating a sudden change in the atomic trapping potential. Such sudden changes create phase perturbations of the wave function, which leads to density perturbations. Analyzing these changes enables studies of the evolution of the coherence in a one-dimensional Bose gas with dynamically changing boundary conditions. Of particular interest is the study of prethermalization which can be understood in an integrable systems as so-called generalized Gibbs state. This state does not decay, but in case that there are perturbations that break integrability, this state relaxes further to a thermal state.

To get a good understanding of such 1D systems we first investigated the transition from 3D to 1D Bose gas by observing both in situ and time of flight density profiles and analyzing the spatial variations in atom number as a function of temperature, geometry, and atomic density.

High quality imaging is essential in these types of atomic physics experiments, and therefore a whole chapter is devoted to a new optimization method of absorption imaging. In this method we have taken into account the quantum nature of both the atomic medium and imaging light.

Last, we have outlined an experiment that utilizes one-dimensional Bose-Einstein condensate as an analogue model of quantum field theory, in particular the dynamical Casimir effect and Hawking radiation. We do so by dynamically splitting a condensate along its long axis to a Y-like shape and measure the differential phase between the branches.

Acknowledgments

Many people have been involved in the challenging work described in this thesis, and just simple gratitude is not enough for all their help and support. First, I want to start with my advisor and friend Peter Krüger for the opportunity and guidance. He knew when to advise, and when to let me go off my own. His way of looking at complex systems and simplifying them is a great virtue and through our deep discussions he opened for me a door to this exciting field of science. My co-advisor Thomas Fernholz for his help and guidance, his ability to drill deep into the very core of things was very helpful on so many occasions. And of course to Igor Lesanovsky, the man who has an answer to all theoretical questions.

Building the lab was possible only with the joint work with Anton Piccardo-Selg, who has been a friend and partner in carrying out all the little steps on the way to the lab, from learning the basics together, to discussing ideas or just having a cold beer after a long day (the time where our best ideas appear).

To Fedja Orucevic our wonderful post-doc who joined us later on and now continues the lab work with great dedication and care, it has truly been fun to work with him. And to wish a lot of luck to Thomas Barrett who lately joined the lab.

I also want to thank the cold atom team: Lucia, Sonali, Asaf, Matthew, Simon, Thomas L, Thomas M, Cristian, Steffano, Jessica, Samanta, Weibin, Beatriz, Cenap, and last but not least Mark Fromhold. It has truly been a pleasure working in such a wonderful and challenging environment.

I want to give special thanks to Romina Davoudi and Maria Hall, who allowed us just to work, and dealt with all the lab and student administration for us.

Special thanks goes to my collaborators Susanne Pielawa and Ehud Altman from the Weizmann Institute, and Serena Fagnocchi, with whom I had the pleasure to collaborate on the Zipper and quench experiments and opened for me the door to the world of quantum gravity analogue models.

To Shimon Machluf, Ran Salem, Tal David, David Groswasser, Meni Givon, Yonni Japha, and Ron Folman from the BGU Atom Chip Lab with whom I worked on the quench and 1d system experiments. Thank you so much for the trust, friendship, and support.

To my ISR-555 “Ghost” The sailing team who allowed me to continue sailing although I could show up just for the races; it has been a bright spot every time things went wrong in the lab.

I found it hard to explain the support I got from my parents, Doron and Orly, and my brothers Boaz and Erez, who pushed me constantly for achievements and providing such strong shoulders. I also owe them my tendency to explore and my urge to comprehend. Finally, none of this could be done without the support of my beloved wife Sivan, thank you so much for being by my side through this long process.

To my wife, Sivan, and daughter, Emily.

Contents

Introduction

The emergence of laser cooling and trapping opened the door to one of the most exciting and rapidly evolving fields of science, where ensembles of atoms and molecules can be cooled below the recoil limit down to quantum degeneracy[1, 2] and act as highly sensitive sensors or exploration tools in fundamental physics.The tremendous technical progress of the last few decades perfected laser cooling and magnetic trapping to a very robust level, such that repetitive experiments using Bose-Einstein condensation (BEC) [3, 4, 5] as well as degenerate Fermi gases [6] can be done on the very statistical nature of quantum physics. Such experiments confirmed many of the theoretical predictions made in the early days of quantum mechanics [7, 8].

As part of world effort to study the behavior of quantum systems many tools for external and internal manipulation, and probing of atoms were developed. Consequently, many new fields such as quantum simulations, sensing, interferometry, analogue models, metrology, and interferometry become reachable. The wish that this knowledge will lead in the near future to development of quantum-technology-based commercial applications is large and backed by many funding agencies [9]. Another important use of quantum degenerate gases is as quantum simulation devices in solid-state and many-body physics. Using cold atoms in optical lattice experiments can mimic the periodic potential structure found in crystalline matter [10], realize the Bose-Hubbard-model [11], or a bosonic Josephson junction and the observation of tunneling in this system [12]. Using gases of fermionic atoms one can explore the BEC-BCS crossover [13]. Exploiting these fermionic systems one can also explore high-T_C superconductivity [14, 15]. The response of a quantum system to time dependent changes in the trap geometry is an issue that attracts large amounts of attention. A wide range of theoretical and experimental work is done in the context of quantum quenches [16, 17, 18, 19, 20, 21]. Such quenches are not limited just to geometry, but also to changes in the interaction strength between particles [22] or temporary abrupt changes [23]. In this thesis we have investigated different types of quenches theoretically and experimentally. A new and exciting use for BEC is as a gravitational analogue model [24, 25], where as part of this thesis we simulate an experiment together with its theoretical analysis in which condensed cloud acts as a simulation device for the Dynamical Casimir Effect and Hawking radiation.

Atom chips [26, 27] brought a new and promising approach to manipulate and control quantum systems at small and large scales. An atom chip is an array of micro structures over gold-covered silicon wafers that lie inside the vacuum such that atoms

can be trapped a few microns from the chip surface [28]. Through these structures we pass an alternating or constant currents that produce steady or rf magnetic fields, or electric fields by acting as electrodes. As part of this work we mainly used atom chips to apply dynamic manipulations on atoms such as interaction quenches by abruptly changing trap parameters. Also we have simulated the creation of time-dependent rf splitting of a condensate by atomochip [29]. As a first stage, we have developed a unique atom chip that can apply dynamic manipulations on an atomic sample using time and spatially dependent rf dressed potentials. Using these potentials we can dynamically split a condensate to a Y shape and investigate changes of the sub-cloud's differential phase (see chapter 6).

The majority of the PhD work was done at the Cold Atoms and Quantum Optics Group at The University of Nottingham and was devoted to building a BEC machine from scratch (BEC1 setup). This work was done together with my lab-mate Anton Piccardo-Selg and later on with our postdoc Fedja Orucevic. The experimental system was designed both as an atom chip BEC experimental platform and as a sand box for ideas that relate to the EC iSense gravimeter project [9]. As a result, a unique chip under-structure was designed to allow atomic trapping without external coils. A new team is now working to reach condensation with the setup. Exhaustive review of our experimental system and the iSense project can be found in the thesis of Anton [30], where in this thesis we focused on experiments that were done on the Nottingham system and other collaborative projects. Two collaborative projects are presented here. The first, which relates to the experimental work on quasi-1d BECs, was done in Ben-Gurion University, in Ron Folman's Atom chip Lab. The work there was mainly done together with Shimon Machluf and Yonni Japha. Another collaboration was done in relation to the gravitation analogue model with Serena Fagnocchi and Ehud Altman based on previous work that was done with Eugene Demler.

Thesis outline

This thesis is organized as follows: in chapter 1 we give a brief summary of "the way to BEC", which incorporates the theory behind laser cooling and magnetic trapping; also we review magnetic trapping using atom chips and evaporative cooling.

Chapter 2 "Optimisation of Atomic Imaging", deals with how to maximize the signal to noise ratio in atomic absorption imaging systems. We start with a short review of the Nottingham and BGU imaging systems, then we go in depth on the theory of absorption imaging. We review the different noises that reduce the quality of atomic imaging. Later a theoretical analysis shows the influence of the major quantum phenomena that change the image quality, such as spontaneous emission, atomic saturation, and light detuning. We exhibit both theory and experimental results on how to maximize the SNR in absorption imaging on large spectra of intensities and atomic densities.

Chapter 3 “One dimensional BEC,” is both theoretical and experimental and deals with Bose gas in anisotropic traps. We review the theory both from the Bogoliubov approach for weakly interacting Bose gas, and the Luttinger liquid theory. A large part of the chapter deals with phase coherence and its effect on the atomic density both in situ, and as a function of time of flight. We review the experimental system we used and the atom chip setup at BGU. The experimental part of this chapter starts with the cooling process of an atomic sample in anisotropic trap. Later we demonstrate the translation of phase fluctuations to density perturbation as a function of time of flight for the case of BEC in the 3d/1d crossover regime. We measured the translation using two experimental techniques and present new interesting initial results.

Chapter 4 “Density fluctuations in a quasi-1d BEC” explores the quantum behavior of Bose gas in extremely anisotropic traps. This chapter explains the theory of (no) BEC in 1d and the effect of phase and density fluctuations on the atomic coherence in 1d Bose gas. In this chapter we also present some technical aspects of atom chip experiments. Later we calculate the variance in atom number as a function of the mean atomic number per pixel in the in situ density profile.

Chapter 5 “Interaction Quenches in One-Dimensional Bose Gas”. In this chapter we research the effect of interaction quench on Bose gas in highly anisotropic traps. We apply the quench by abruptly changing the radial trapping frequency of a Bose condensate, which by doing so changes the interaction parameter. We investigated the change in the in situ density profile before and after the quench where quantum effects as prethermalization appear. We look into the changes in the bunching behavior of the condensate by seeking shifts in the atom number variance and in the Fourier space as a function of time.

Chapter 6 “Zippers and Quantum Mechanics: A proposal for measuring the dynamical Casimir effect”. In this chapter we investigate what would happen if we apply time-dependent spatial manipulation on a 1d quasi-BEC. Using spatially and time-dependent rf dressed potentials we “unzip” a condensate to a Y shape, where after some time of flight we investigate the given interference pattern from the Y legs. Treating the condensate as a 1d Minkowski space, and phonon modes as vacuum Modes, allows us to use the condensate as an analogue model for quantum field theory. Given different effects, the Dynamical Casimir Effect or Hawking radiation can be simulated.

1 The Way to BEC

1.1 Introduction

One of the most exciting phenomena nowadays in physics is Bose Einstein Condensation (BEC). In this relatively new field of research, a window of opportunity has opened to investigate experimentally different quantum phenomena that were considered unreachable until the realization of BEC in cold atoms.The first predication of BEC was in 1925 when Einstein extended Bose's idea for photons [7, 31] and predicted that below a critical (finite) temperature, a macroscopic population of the ground state of the system occurs [8, 32]. The first "pure" BEC was created by Eric Cornell, Carl Wieman, et al. at JILA in 1995 [3], where about four months later Wolfgang Ketterle et al. at MIT also created a BEC of sodium-23 [5]. The achievement could not have be done without powerful laser cooling [1, 33, 2] and evaporative cooling [34, 35]; both were new techniques at that time.

Bose Einstein Condensate raises great interest since it exhibits quantum phenomena on a microscopic scale. Therefore the study of BEC is spread over many sub-fields in physics, including atomic, condensed matter, nuclear, magnetism, quantum physics, and quantum field theory.

In this introductory chapter we will briefly review the theoretical aspects of BEC starting with build-up of a knowledge base for the following chapters of the thesis. To begin, we will review the basics of laser cooling, Magneto-Optical Trapping (MOT), magnetic trapping, and evaporative cooling [36, 37]. Later we will review the theory of a BEC in a magnetic trap [38, 39, 27].

1.2 Laser Cooling and Trapping

At the very heart of our experiment we cool ^{87}Rb below the recoil limit down to the nano-Kelvin region. To begin, using an Rb dispenser we fill our vacuum chamber with a mixture of ^{85}Rb and ^{87}Rb atoms at an average temperature of 1000 K [40]. From such a high temperature ^{87}Rb atoms need to be decelerated rapidly so they could be trapped. Decelerating and trapping can be done by an elegant and important tool called magneto-optical trap (MOT) [41]. This technique combines laser light and zero-crossing gradient magnetic field. Laser light, when tuned close to an atomic resonance, can apply significant force on an atom. The deceleration

comes from the sum of the energy of absorbed photon ($\hbar\omega$) times the total sum of absorbed photons by the atom, and can reach levels as high as $10^4 \cdot g_{gr}$, where g_{gr} is the gravitational acceleration. The light can cool the ^{87}Rb atoms to about $15\,\mu$K, and a combination of six-way laser and zero-crossing gradient magnetic field can trap the atoms at densities up to $10^{17}\,\mathrm{m}^{-3}$. Such high phase-space density is essential for the next stages of cooling.

The process of laser cooling works as follows; once an atom absorbs a photon it gets momentum "kick" $\Delta\vec{p}$, where $\Delta\vec{p} = m\Delta\vec{v} = \hbar\vec{k}$, where $\Delta\vec{v}$ is the change in the atomic velocity, and $\vec{k}$ is the wave vector of the incident photon ($2\pi/\lambda$), i.e., the momentum "kick" is in the direction of the incident beam. The energy of the photon goes into an internal state of the atom where the atom is promoted to an excited state. We must also account for spontaneous emission where the atom decays to its ground-state and the florescence photon will be emitted in a random direction given by the symmetric dipole radiation pattern. Therefore, after many realizations the total net momentum due to spontaneous decay will be zero and the atom will gain momentum only in the direction of the incident beam. If the wavelength of the light is slightly red detuned from the atomic resonance, the absorption cross-section of the incoming atoms towards the laser light will be greater compared to the stationary atoms. As a result, we can also disregard the atoms' velocity component in the direction of the laser beam where the cross-section will be negligible. Therefore, shining red-detuned laser beams from six opposite directions can act as an effective friction force slowing the atom's velocity. The equation for the average force of two counter-propagating laser beams on a two-level atom (known as optical molasses) is [37]

$$\vec{F} = \hbar\vec{k}\frac{\Gamma}{2}\left[\frac{s_0}{1+s_0+\left[2\left(\Delta-kv\right)/\Gamma\right]^2} - \frac{s_0}{1+s_0+\left[2\left(\Delta+kv\right)/\Gamma\right]^2}\right] \approx -\alpha\vec{v}, \quad (1.1)$$

where $\Gamma = 2\pi/\tau$ is an angular frequency corresponding to the decay rate of the excited state, $s_0 = I/I_s$ is the laser intensity normalized by the saturation intensity of the atom (for ^{87}Rb $I_s = 1.6\,\mathrm{mW/cm^2}$), and $\Delta = \omega_0 - \omega_{laser}$ is the laser detuning from resonance. For $v \to 0$, one can apply linear approximation, which manifests the damping coefficient in a friction-like way $\alpha \simeq 8\hbar k^2 s_0 \frac{\Delta/\Gamma}{\left(1+s_0+(2\Delta/\Gamma)^2\right)^2}$, where therms of order $(kv/\Gamma)^4$ in the denominator of (Equation 1.1) have been neglected [37].

The molasses force can be reduced down to a non-zero value that relates to the natural line-width of the transition Γ. This is known as the Doppler limit, where the recoil from stochastic absorption-emission events becomes significant relative to the force applied by light. This Doppler limit is presented as follows $T_D = \hbar\Gamma/2k_B \sim 147\,\mu$K, for $\Delta = \Gamma/2$. But it was experimentally shown that using laser cooling it is possible to get much below this limit; this is due to the actual many level structure of the alkali atoms and polarization of light, and can be illustrated as follows.

A more realistic picture is given by a many-level atom model rather than two-level one. By Doppler distribution all the atomic ground-state Zeeman levels are

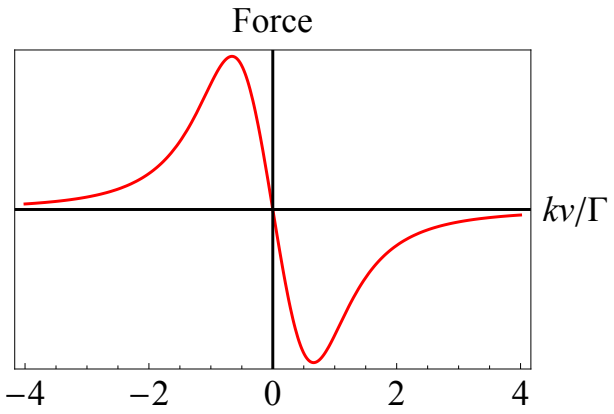

Figure 1.1: Velocity-dependent force for one-dimension optical molasses (Equation 1.1). The horizontal axis is the normalized velocity kv/Γ, where k is the wave-vector of the laser beam and Γ is the line-width of the atomic resonance. We used the values $s_0 \to 2$ and $\Delta \to -\Gamma/2$. For illustrative reasons Γ and $\hbar$ were normalized to one.

populated equally, and one can see that there is an induced atomic orientation that appears at the ground state as a result of the atomic motion. Such phenomena can be illustrated as atomic dipole, which is relative to the polarization of the light field. Once the atom moves through rotating linearly polarized light, this induced orientation tries to follow the light's rotation. This process has a given pumping time. Light from two counter-propagating circular polarized beams can have a rotating linear polarization pattern, where the pumping time is longer than the shift in the polarization of light. This causes the two counter-propagating waves to be absorbed with different Efficiencies; this absorption imbalance creates unequal radiation pressure and as a result a net friction force. Such effective friction gives rise to the sub-Doppler cooling effect. This effect is also known as polarization gradient cooling [42]. Our MOT counter-propagating beams have opposite circular polarization ($\sigma^+ - \sigma^-$ configuration) such that the superimposed polarization is linear everywhere, but the vector rotates spatially about its axis with a periodicity of $\lambda/2$ (see Figure 1.2). Once the atom tries to follow the light orientation it scatters more photons from the opposite beam to its velocity direction; hence it slows down below its Doppler velocity. Using such a scheme we can cool our atomic sample below the Doppler limit, but there is a boundary that we cannot cross with any light-related cooling. This is the temperature that is given by the last spontaneous emission and hence the last recoil event that sets the recoil limit $k_B T_r \equiv \hbar^2 k^2/m \sim 348.66\,\mathrm{nK}$.

So far we have been discussing cooling using a dissipating light force but without the presence of any spatial confinement. During cooling, the atoms go through a series of random "kicks" as in random walk from the spontaneous emission process. This random walk can easily diffuse the atoms from the overlap region of the laser beams so they will be lost. A quadrupole magnetic field, with respect to the laser beam

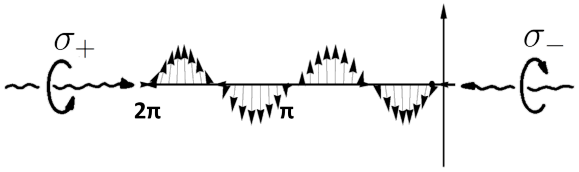

Figure 1.2: The polarization gradient in a 1d molasses while using $\sigma_+ - \sigma_-$ configuration. The two circularly polarized laser beams create a linear polarization that rotates in space around the quantization axis [42].

polarization and the laser cross-point, can create a spatial confinement around a minimum. In a 1d MOT the magnetic field can be illustrated as $B(z) = Az$, since it has been created by a magnetic quadrupole field. For the simplest scheme of atomic transition $J_g = 0 \rightarrow J_e = 1$, the excited state, J_e, has three Zeeman components in the presence of a magnetic field (see Figure 1.3).

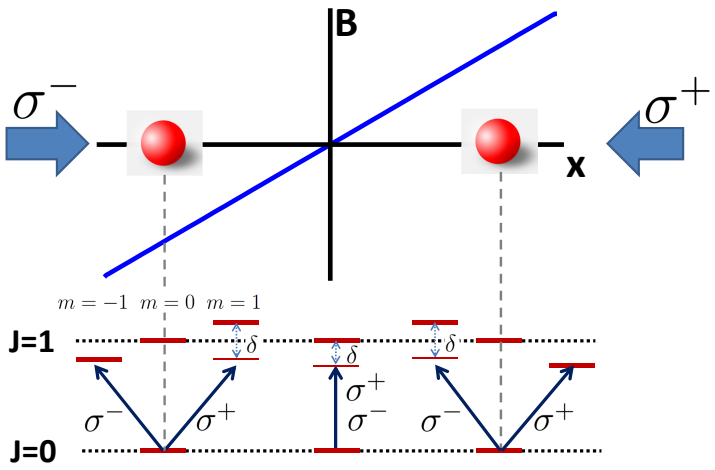

Figure 1.3: MOT. Illustration of one-dimensional MOT showing the position dependence forces applied on the atoms. The zero crossing magnetic field breaks the degeneracy in $J = 1$ excited state and creates preferred absorption of light towards the centre where the magnetic field is zero. Therefore a position dependent force pushes the atoms towards the field minimum [43].

The magnetic field spatial dependence shifts the level spacing such that the probability to absorb a photon with a given circular polarization is greater than any other polarization. The light is set such that the atoms will be pushed to the center of the trap where the magnetic field is zero. In order to achieve further cooling at the end of the MOT phase one can either turn off the magnetic fields, i.e., start optical

molasses, or further detune the light to reduce the dipole moment between the light and atoms.

1.2.1 Further cooling processes

To reach BEC the atomic sample needs to be cooled below the critical temperature. Given that the minimal phase space density of a BEC transition is $\phi = \zeta(3/2) = 2.612$, extreme laser cooling allows cooling of the sample up to $\phi \approx 10^{-5}$ at most, which is five orders of magnitude lower than needed for BEC. This is due to the recoil momentum and radiation pressure inside the cloud, which limits the density of the cloud. To overcome this limit the atoms need to be trapped in a conservative potential such as a dipole or magnetic trap. We will consider the latter in this section. Once the atoms are magnetically trapped they need to be further cooled; we do that using forced rf evaporative cooling. Evaporative cooling is the same as cooling a hot cup of coffee by blowing across its surface. In the case of the coffee, there is a temperature gradient where the hotter particles are higher (reaching higher potential energy); blowing air on the top of the cup means throwing out the hot particles, which carry more than the average energy per particle. The rest of the sample will then thermalize to a new lower average temperature. In the experiment we couple the hottest atoms to rf radiation tuned to the transition frequency between the Zeeman levels. This resonance effect spin-flips the atoms to a non-magnetic state, and expels them from the trap. The atoms reach a new average temperature by elastic collisions that redistribute the energy between the atoms. The rf frequency ('knife') is tuned down during the evaporation process to increase cooling. The rate of reducing the 'knife' depends on the time needed for the system to thermalize, i.e., elastic collision rate. The higher the density of the atoms, the higher the good collision rate will be and cooling will more efficient. Bad collisions are collisions with the background gas that heats, decoheres, and kicks out atoms from the atomic sample. This rate ratio, $R = \gamma_{el}/\gamma_{loss}$, between the good and bad collisions is an important number to notice. The elastic collision rate can be deduced by a simple calculation [35]

$$\gamma_{el} = n_0 \sigma_{el} v_{MB}, \tag{1.2}$$

where $\sigma_{el} = 8\pi a_s^2$ is the s-wave cross-section for elastic collision, and v_{MB} is the mean relative velocity of the Maxwell-Boltzmann distribution.

$$v_{MB} = \sqrt{\frac{8 k_B T}{\pi m}}. \tag{1.3}$$

To achieve sustained evaporation the rf frequency, f_{rf}, should be tuned above the trap bottom such that the frequency change rate will maintain or increase the elastic collusion rate. The truncation parameter, η, defines the energy above the trap bottom for the evaporation process by

$$\eta = \frac{h f_{rf} - \mu_B g_F m_F B_{ip}}{1/2 k_B T}. \tag{1.4}$$

For an efficient evaporation the parameter η should kept constant throughout the sweep, while low η allows a fast sweep, and high η allows a slow one. Slow sweep means low loss rate and more efficient cooling. The downside is that the cooling process takes longer.

An explanation of the sweep we used in the experiment will be given in subsection 3.2.3.

1.2.2 Magnetic Trapping of Neutral Atoms

Once the atoms reach a temperature of about 150 μK they are cold enough to be magnetically trapped. Magnetic trapping is possible only if there is a dipole moment between the atoms and the magnetic field. And since it is beneficial to have a quadrupole field with a minimum at the position of the atoms (by the Earnshaw theorem it is not possible to create a maxima in a 3d magnetic field without a source at the maximum), the dipole moment between the field and atoms should be negative, hence the atoms are at a "low field seeking" state. The coupling potential is the atom's magnetic dipole and in 1$^{\text{st}}$ order is

$$V = -\vec{\mu} \cdot \vec{B} \approx \mu_B g_F m_F \left|B\right|, \tag{1.5}$$

where $\vec{\mu}$ is the atomic momentum, $\mu_B = 9.274 \cdot 10^{-24}\,\text{J/T} = 1.4\,\text{MHz/G}$ is the Bohr magneton, g_F is the atomic Landé g-factor for the hyperfine level F, and m_F is the magnetic Zeeman sub-level. Once an atom is in a magnetic field its spin precess is around the magnetic field vector. The precession frequency is called Larmor frequency and is described as follows $\omega_L = \mu_B g_F m_F B/\hbar$. In the case of $B \to 0$ the atom can lose its spatial orientation and spin flip to another m_F state, such as a "high field seeking" state. This phenomenon is known as Majorana spin flips and its rate scales as T^{-2} in a quadrupole magnetic trap [44]. One way to suppress these spin flips is to add an orthogonal offset magnetic field to the quadrupole field, so the minimum of the trap would have non-zero value. We would call this orthogonal magnetic field the Ioffe-Pritchard field [26, 45]. For such a case, the Majorana loss rate would then be written as [26, 46]

$$\gamma_{\text{Majorana}} = \frac{\pi\omega}{2\sqrt{e}} \exp\left(-\mu_{\parallel} B_{ip}/\hbar\omega_{\perp}\right), \tag{1.6}$$

where the atom magnetic moment $\mu_{\parallel}$ is set along the offset field B_{ip}, which defines the quantization axis, and $\omega_{\perp}$ is set as the tightest confinement (the radial trapping frequency in our case). From the exponential nature of this calculation we can assume that even for an Ioffe-Pritchard field of a few mG the loss rate will be negligible for the timescale of our experiment.

The Larmor frequency also sets the adiabatic condition for a "well behaved" field such that $\frac{1}{\left|\vec{B}(x(t),t)\right|}\frac{d\vec{B}(x(t),t)}{dt} < \omega_L$. As long as we satisfy this term we can say that a change in potential is adiabatic.

1.2.3 Magnetic trapping using an atom chip

In this section we will explore the basic concept behind magnetic trapping and the benefits of using atom chips.

The magnetic field that is created by a rectangular slab can be written using the Bio-Savart law as

$$\vec{B}(r) = \frac{\mu_0}{4\pi} \int\limits_{volume} \frac{d\vec{J} \times \Delta\hat{r}}{\Delta r^2}, \tag{1.7}$$

where $\mu_0 = 4\pi \cdot 10^{-7}\,\mathrm{N/A^2}$ is the vacuum permeability constant, and $\vec{J} = \begin{cases} in & J_0\hat{x} \\ out & 0 \end{cases}$ is the current density vector for a current in the $\hat{x}$ direction, while $J_0 = I/(W\,H)$. The latter represents the total current divided by the width and height of the slab (Figure 1.4).

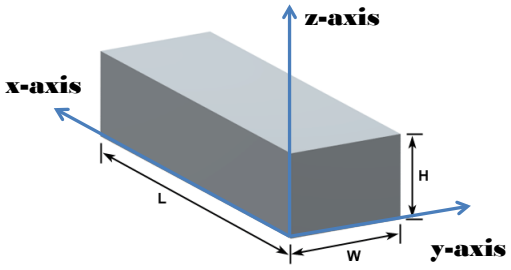

Figure 1.4: Presentation of a current carrying slab. The $x-$axis is the quantization axis and the direction of current, the $z-$axis is the height from the chip. We call the x and the $y-z$ direction, longitudinal and transverse directions, respectively.

We start by looking at the simple case of a magnetic field at a point r given by an infinitely long and thin wire, where the Bio-Savart law reduces to

$$\vec{B}(r) = \frac{\mu_0 I}{2\pi r}\hat{e}_\phi, \tag{1.8}$$

where $\hat{e}_\phi$ is the azimuthal unit vector. The field gradient is represented by $B^{(1)}(r) = \frac{\mu_0 I}{2\pi r^2}$. From the latter we can see that in order to create tight trapping confinement it is beneficial to be as close as possible to the trapping wire since the gradient reduces quadratically with distance. A zero magnetic field at a point r_0 can be created by adding a bias magnetic field $\vec{B}_b = -\vec{B}(r_0)$. This will set the trapping point where the field is minimal. This Bias field can be created by many sources such as external anti-Helmholtz coils, additional chip wires, current sheet, or a combination

of a few. In order to avoid spin flips due to the zero magnetic field as previously explained, a weak orthogonal magnetic field is added, i.e., an Ioffe-Pritchard (IP) field (Figure 1.5). So now the total magnetic field can be written as follows

$$\vec{B}_T(r) = \left(\frac{\mu_0 I}{2\pi r} + B_b\right)\hat{e}_\phi + B_{ip}\hat{e}_r. \tag{1.9}$$

After expansion of $\left|\vec{B}_T(r)\right|$ around r_0 using Taylor up to second order, one gets

$$B_T(r) \sim B_{ip} + \frac{B_b^2}{2r_0^2 B_{ip}}(r - r_0)^2 + O\left[r - r_0\right]^3. \tag{1.10}$$

Using Equation 1.5 on Equation 1.10 one gets the atom's potential energy, while oscillation about a stable equilibrium point, from which we can calculate the harmonic trap transverse frequency $\omega_\perp^2 = \frac{\mu_B g_F m_F}{m}\frac{B_b^2}{r_0^2 B_{ip}}$, where m is the atomic mass. Using the harmonic potential in the case of thermal atoms we can calculate the cloud size as $\sigma_\perp = \sqrt{\frac{k_B T}{m\omega_\perp^2}}$, i.e., one standard deviation of the Gaussian profile.

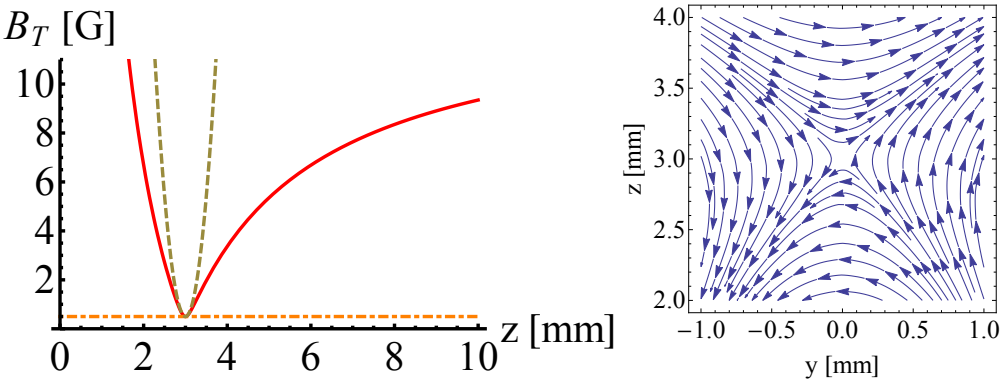

Figure 1.5: Illustration of a magnetic trap created by a single wire and external coils. Left: The red line presents the total magnetic field as in Equation 1.9 $\left(B_T = \left|\vec{B}_T(r)\right| = \left|\left(\frac{\mu_0 I}{2\pi r} + B_b\right)\hat{e}_\phi + B_{ip}\hat{e}_r\right|\right)$. The orange dot-dashed line presents the bias field $\left|\vec{B}_b\right|$. And the green dashed line is the approximation to harmonic oscillator that was done by expanding the magnetic field equation around the trap bottom to second order. Right: The vector field of the same magnetic trap. A current of 30 A is pushed through the wire while a bias field of 13.3 G shifts the trap minimum to $z = 3\,\text{mm}$, $y = 0\,\text{mm}$. A IP field at 0.5 G applied along the quantization axis (x); an additional magnetic field in the z direction will shift the trap along y.

So far we have checked the magnetic field by a single wire, but in order to create longitudinal confinement we need to create a 3d trapping potential. Such potential can be created by adding perpendicular wires (legs) to the chip axis. The combination of the confining wires and the central trapping wire can come in many forms,

the most known ones are the H and Z shape traps (with 90° at the turn points). There the confining potential can also create the IP field. Using the $Z-$trap is straight forward, where the legs are designed with a given distance from each other and the current passes from the edge of one leg via the central wire to the edge of the other leg. Such a trap will create both the confining potential and IP field. Since $\omega_\perp \sim 1/\sqrt{B_{ip}}$ for a given distance and current, in some cases we will have to increase or reduce the IP field using the external bias coils in order to achieve the wanted trapping frequency and depth. The ability to fabricate double layer chips extends the variety of traps, since the currents in the different structures can be independent. One of the more successful types is the $H-$trap. There the current in the legs can be different from the main trapping wire. It is possible to pass current in both legs in the same direction so a confining potential plus IP field will be created, or in opposite directions where a confining potential is created but also zeros the IP field at the center. The atomic cloud follows the minimum magnetic field line; this minimum field line has bends in a banana-like shape due to the imposed legs field over the central wire magnetic field (see Figure 1.6). Another advantage of the $H-$traps over the Z is the ability to create box-like longitudinal potential by passing low currents through the legs. Since the bend is directly related to the field strength ratio between the central wire and the legs, a high ratio will create an almost negligible bend.

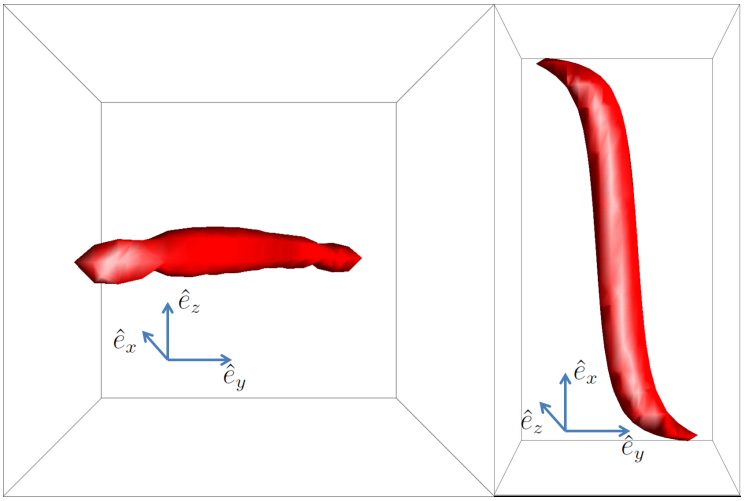

Figure 1.6: Illustrations of an atomic cloud in a magnetic Z-trap. The magnetic fields vector from the trap legs and central wire has field component, $\hat{z}$, in either opposing or similar direction therefore the trap minimum has a banana like shape. Left: the cloud along the quantization axis. Right: top view of the same cloud. One can see on the left image a banana like bend towards the chip, and and s-like shape in the right image (top view).

The limit to the approximation done in (Equation 1.8) is when $W, H \geq r$. Once the scale of the slab is in the order of r, we should calculate the field directly using

(Equation 1.7), and the gradient will be reduced. Hence the trapping frequency will be lower.

The extremely tight and large variety of trapping potentials is one of the key advantages in using atom chips [26]. Having the atoms in close proximity to the chip surface allows trapping geometries where the trap depth and frequency are much higher than the thermal energy. But as the trap is lowered toward the chip surface, finite size effects start become significant. Here we will calculate the magnetic field of a current-carrying slab with finite width, length, and height

$$\begin{gathered} B_x = 0 \\ B_y(x,y,z) = -J\left[\arctan\frac{(L-2x)(W-2y)}{2z\sqrt{(L-2x)^2+(W-2y)^2+4z^2}} + \arctan\frac{(L+2x)(W-2y)}{2z\sqrt{(L+2x)^2+(W-2y)^2+4z^2}} + \right. \\ \left. \arctan\frac{(L-2x)(W+2y)}{2z\sqrt{(L-2x)^2+(W+2y)^2+4z^2}} + \arctan\frac{(L+2x)(W+2y)}{2z\sqrt{(L+2x)^2+(W+2y)^2+4z^2}}\right] \\ B_z(x,y,z) = \frac{J}{2}\left[\mathrm{Log}\frac{-L+2x+\sqrt{(L-2x)^2+(W-2y)^2+4z^2}}{L-2x+\sqrt{(L-2x)^2+(W-2y)^2+4z^2}} + \mathrm{Log}\frac{-L-2x+\sqrt{(L+2x)^2+(W-2y)^2+4z^2}}{L+2x+\sqrt{(L+2x)^2+(W-2y)^2+4z^2}}\right. \\ \left. \mathrm{Log}\frac{L-2x+\sqrt{(L-2x)^2+(W+2y)^2+4z^2}}{-L+2x+\sqrt{(L-2x)^2+(W+2y)^2+4z^2}} + \mathrm{Log}\frac{-L-2x+\sqrt{(L+2x)^2+(W+2y)^2+4z^2}}{L+2x+\sqrt{(L+2x)^2+(W+2y)^2+4z^2}}\right] \end{gathered} \tag{1.11}$$

where $J = \frac{\mu_0}{4\pi}H\cdot j = \frac{\mu_0}{4\pi}\frac{I}{WL}$, and the slab height, width, and length are H, W, and L, respectively. For simplicity we took $H \ll z$ and current flow in the $\hat{e}_x$ direction. For current flow in the $\hat{e}_y$ direction, such as at the trap legs, the following conversion needs to be applied

$$\left(\begin{array}{c} B'_x \equiv -B_y,\ B'_y \equiv 0,\ B'_z \equiv B_z \\ x' \equiv -y,\ y' \equiv x,\ z' \equiv z \end{array}\right). \tag{1.12}$$

If greater precision than (Equation 1.11) is needed, finite element modeling (FEM) solutions can calculate the magnetic field distribution, taking into account edge effects, flow around corners, and non-uniform current density.

Energy consideration

After looking at the fundamentals of magnetic trapping, we look at the energy scales that are involved with magnetic trapping. First we inspect the minimal trap depth for ^{87}Rb atoms at a temperature of 1 K. We would consider atoms to be in the magnetic trappable state $|F=2,\ m_F=2\rangle$ where we know the following values: $\mu_B = 9.274\cdot 10^{-24}\,\mathrm{J/T}$ $g_F = 1/2$. By using Equation 1.5 we can calculate the field temperature ratio $\frac{B}{T} = \frac{k_B}{2\mu_B g_F m_F} = 0.671\,\mathrm{T/K} \approx 10\,\mathrm{mG}/\mu\mathrm{K}$. Typical magnetic field values in an atom chip experiment would be $1-10^2$ G, so atoms need to be pre-cooled drastically to the micro-Kelvin region at the MOT stage. Further cooling processes such as evaporative cooling will be explained in section 1.3, for which it is important to achieve maximal phase-space density before loading a magnetic trap.

1.3 Bose-Einstein Condensation

The possibility of having a macroscopic population of the ground-state was first introduced by Bose, addressing the statistic of photons [7, 31]. Later after discussions with Einstein, the theory was extended to particles in free space. Einstein found that below a finite critical temperature such macroscopic Population also happens in ideal gas particles [8, 32]. Bose-Einstein Condensation (BEC) was only considered in non-interacting particles up to the first experiments in ^{4}He where super-fluidity was observered. It was London at that time who connected this super-fluidity with condensation, although the system was a strongly interacting one [47, 48]. In 1995 BEC was demonstrated by JILA and MIT groups in atomic vapor [3, 5]. For this achievement, the Nobel Prize in Physics was awarded in 2001 to Eric A. Cornell, Wolfgang Ketterle, and Carl E. Weiman [49, 50, 51]. This was a beginning of a world-wide effort to understand this remarkable Phenomenon; the outcome of this research spread over numerous review papers and books (e.g., [52, 34, 53, 54, 55]). The first BECs using an atom chip were achieved in the Tübingen, Münich, Heidelberg, and Sussex groups [56, 57, 58, 59].

1.3.1 Theoretical overview

In the case of room temperature atoms the number of accessible states for each atom is enormous; therefore the probability of having two atoms in the same state is extremely low. When temperature goes down the number of accessible states decreases until, at a certain low temperature, T_c, a large fraction of the bosonic population occupies the lowest energy quantum state. When the deBroglie wavelength, λ_{dB}, is in the order of the inter-particle distance the number of quantum state is in the order of the number of atoms. Once this is the case it is possible to describe these condensate atoms using a single wave-function. The deBroglie wavelength can be written as

$$\lambda_{dB} = \frac{2\pi\hbar}{mv} \approx \sqrt{\frac{2\pi\hbar^2}{mk_BT}}, \tag{1.13}$$

where m is the atomic mass, v is the atomic velocity, and T is the temperature of the gas. Since condensation starts when the deBroglie wavelength is in the order of the inter-particle separation of the gas we can calculate the critical temperature as follows: the critical $\lambda_{dB} \approx \left(\frac{N}{V}\right)^{-1/3}$, where N is the number of atoms and V is the occupied volume. Substituting this value in (Equation 1.13) gives the critical temperature [54]

$$T_c = \frac{2\pi\hbar^2}{k_Bm}\left(\frac{N/V}{g_{3/2}(1)}\right)^{2/3}, \tag{1.14}$$

where $g_{2/3}(1) = 2.612$.

Another interesting phenomenon relates to the chemical potential of the system. Since the average number of atoms in the ground state, $\langle N_0\rangle$, becomes large as

function of temperature. As temperature reduces below the critical temperature, T_c, N_0 grows rapidly, and the average number of thermal atoms, $\langle N_T \rangle$, is fixed by temperature (Figure 1.7). This leads to a noteworthy phenomenon; the chemical potential μ, which represents how much the energy of the system changes when the number of particles in the system changes, is close to zero for BEC. Using the grand canonical ensemble, and setting $\mu \to 0$, the thermal part as a function of temperature yields

$$N_T = \left(\frac{T}{T_c}\right)^{3/2} N, \tag{1.15}$$

and the number of particles in the condensate

$$N_0\left(T\right) = N\left[1 - \left(\frac{T}{T_c}\right)^{3/2}\right]. \tag{1.16}$$

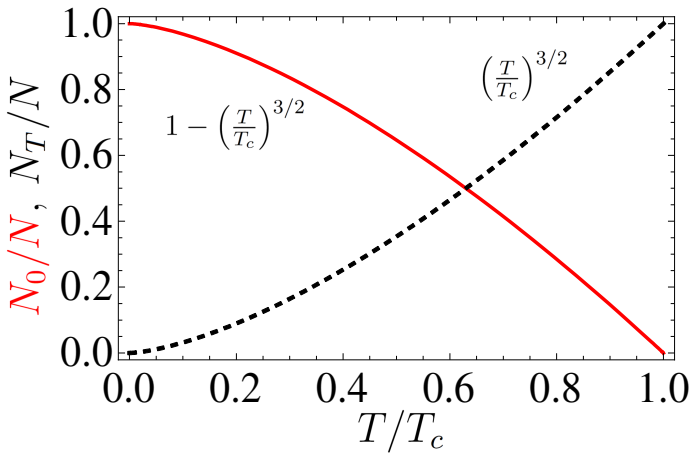

Figure 1.7: Condensate (red) and thermal (dashed) fractions versus temperature. As temperature goes below the critical value ($T/T_c \leq 1$) the condensate part, N_0, grows rapidly and the system starts to condense.

Another highly important quantity, which describe the physics behind BEC, is the phase-space density, ϕ, which is defined as the number of atoms in a box with sides of one thermal deBroglie wavelength [60]

$$\phi = n_0 \lambda_{dB}^3, \tag{1.17}$$

where the atoms' peak density is $n_0 = \frac{N}{(2\pi)^{3/2}\sigma_{0,x}\sigma_{0,y}\sigma_{0,z}}$, and $\sigma_{0,i}$ is the in situ size of the cloud in its $i-$th direction. Using the same method as in (Equation 1.13), we

find that the transition starts when $\phi = \zeta(3/2) = g_{3/2}(1) = 2.612$, i.e., the inter-particle distance is in the order of the extensions of the particle's wave function [54].

1.3.2 BEC in harmonic trap

In the presence of a harmonic three-dimensional trapping potential

$$V_{ext}(\mathrm{r}) = \frac{m}{2}\left(\omega_x x^2 + \omega_y y^2 + \omega_z z^2\right), \tag{1.18}$$

the solution of the GP equation would be solved numerically. We first ensure that the Thomas-Fermi approximation holds by setting $\mu_{TF} > V_{ext}(\mathrm{r})$ and zero elsewhere. Using (Equation 1.34) the chemical potential would be [54]

$$\mu_{TF} = \frac{\hbar\omega_{ho}}{2}\left(\frac{15Na_s}{a_{ho}}\right)^{2/5}, \tag{1.19}$$

where $a_{ho} = \sqrt{\hbar/(m\bar{\omega})}$ is the oscillator length using a geometrical average for the trapping frequency, $\bar{\omega} = (\omega_x\omega_y\omega_z)^{1/3}$. The chemical potential can be derived as $\mu = E_{N+1} - E_N \approx \partial E/\partial N$. Integrating over this thermodynamic relation we can obtain the total TF energy per particle

$$\frac{E_{TF}}{N} = \frac{5}{7}\mu_{TF}. \tag{1.20}$$

Another difference that needs to be noted relates to the critical temperature. For non-interacting atoms in a harmonic trap, the chemical potential needs to be set as the trap ground state energy, $\mu = \epsilon_0$, and not to zero. Resolving the thermodynamic equation $N = \sum_{n_x,n_y,n_z\neq 0} \frac{1}{\exp[\beta(\epsilon_i-\mu)]-1}$ for $N = N_T$ gives [54]

$$k_B T_c^{trap} = \hbar\bar{\omega}\left(\frac{N}{\zeta(3)}\right)^{1/3} = 0.94\hbar\bar{\omega}N^{1/3}, \tag{1.21}$$

where $\zeta(3) = 1.202$. And the temperature dependence of the condensate fraction becomes

$$\frac{N_0}{N} = 1 - \left(\frac{T}{T_c^{trap}}\right)^3. \tag{1.22}$$

It is noticeable that (Equation 1.22) derives from (Equation 1.16), since here T behaves like T^3 rather than $T^{3/2}$.

In a harmonic external potential the condensate shape becomes an inverted parabola. This shape is very different than the Gaussian profile given by thermal distribution, or the very narrow final width TF parabola.

It is important to note that in common atom chip traps once atoms are trapped close to a chip surface the trapping frequency becomes so high that $\mu < \hbar\omega_\perp$ and the TF approximation ceases to be valid. In such cases the full GP equation treatment should be done. A more detailed explanation of this phenomenon will be given in the following chapters while explaining the transition from 3d to 1d regime.

1.3.3 Order parameter and many body Hamiltonian

To describe a field operator for a system of interacting Bosons, first we need to identify the single-particle wave functions, $\varphi_i(\mathrm{r})$, for both interacting and nonuniform systems. The field operator creates or annihilates a particle in position r,

$$\hat{\Psi}(\mathrm{r}) = \sum_i \varphi_i(\mathrm{r})\,\hat{a}_i, \tag{1.23}$$

where $\hat{a}_i$ $\left(\hat{a}_i^\dagger\right)$ are the annihilation (creation) operators of a particle in the state φ_i and follows the commutation relations

$$\left[\hat{a}_i,\,\hat{a}_j^\dagger\right] = \delta_{ij}, \quad [\hat{a}_i,\,\hat{a}_j] = 0. \tag{1.24}$$

The time-dependent many body Hamiltonian can be written by means of the field operator [54]

$$\begin{aligned} i\hbar\tfrac{\partial}{\partial t}\hat{\Psi}(\mathrm{r},t) = \left[\hat{\Psi},\hat{H}\right] = \Big[-\tfrac{\hbar^2\nabla^2}{2m} + V_{ext}(\mathrm{r},t) \\ + \int d\mathrm{r}'\hat{\Psi}^\dagger(\mathrm{r}',t)\,V_{int}(\mathrm{r}-\mathrm{r}')\,\hat{\Psi}(\mathrm{r}',t)\Big]\,\hat{\Psi}(\mathrm{r},t)\,, \end{aligned} \tag{1.25}$$

where the first two terms are the kinetic energy and external potential, respectively, while the last term, $V_{int}(\mathrm{r}-\mathrm{r}')$, is the two-body inter-atomic potential.

It is useful to separate the condensate field operator, $i = 0$, from the thermal components in (Equation 1.23)

$$\hat{\Psi}(\mathrm{r}) = \varphi_0(\mathrm{r})\,\hat{a}_0 + \sum_{i\neq 0}\varphi_i(\mathrm{r})\,\hat{a}_i, \tag{1.26}$$

following that we will introduce the Bogolyubov approximation, which replaces the operators $\hat{a}_0$ and $\hat{a}_0^\dagger$ with the $c-$number $\sqrt{N_0}$ [54]. This approximation holds well in BEC since $N_0 = \left\langle \hat{a}_0^\dagger\hat{a}_0 \right\rangle \gg 1$. Therefore we can rewrite the field operator as a classical field

$$\hat{\Psi}(\mathrm{r}) = \sqrt{N_0}\varphi_0(\mathrm{r}) + \sum_{i\neq 0}\varphi_i(\mathrm{r})\,\hat{a}_i, \tag{1.27}$$

where we will define for very low temperatures our field operator as a classical object $\Psi_0(\mathrm{r}) = \sqrt{N_0}\varphi_0(\mathrm{r})$. And since $\Psi_0(\mathrm{r})$ is a complex quantity we can separate it to modulus and phase [54]:

$$\Psi_0(\mathrm{r}) = |\Psi_0(\mathrm{r},t)|\,\mathrm{e}^{\mathrm{iS(r)}}, \tag{1.28}$$

where the modulus determines the diagonal density, $n(\mathrm{r})$, $\left(N = \int d\mathrm{r}\,\mathrm{n}(\mathrm{r})\right)$. While $S(\mathrm{r})$ presents the phase, which plays an important role in the coherence of the BEC. Therefore the order parameter is now reduced to a number and a phase.

1.3.4 The role of interaction

The inter-atomic interaction potential $V_{int}(\mathrm{r}-\mathrm{r}')$ is given by a combination of short- and long-range potentials. The short-range $\left(|\mathrm{r}-\mathrm{r}'| \lesssim 5\,\mathring{\mathrm{A}}\right)$ is due to repulsive interaction of the atom's electron clouds, while the long-range interaction is due to the van der Waals term. This can give rise to bound states and Feshbach resonance [61, 62].

In a cold atomic sample the deBroglie wavelength is much larger than the interaction potential. Therefore the potential can be replaced with a simpler and elegant form of a zero range pseudo-potential with the same properties as s-wave scattering [54]

$$V_{int}(\mathrm{r}-\mathrm{r}') = g_{3d}\delta(\mathrm{r}-\mathrm{r}'), \tag{1.29}$$

where g_{3d} is the three-dimensional coupling constant. Applying (Equation 1.29), the interaction term in (Equation 1.25) becomes

$$\frac{4\pi\hbar^2 a_s}{m}\int d\mathrm{r}'\hat{\Psi}^{\dagger}(\mathrm{r})\,\hat{\Psi}^{\dagger}(\mathrm{r})\,\hat{\Psi}(\mathrm{r})\,\hat{\Psi}(\mathrm{r}) = g_{3D}\left|\Psi_0(\mathrm{r},t)\right|^4. \tag{1.30}$$

The coupling constant is [54]

$$g_{3d} = \frac{4\pi\hbar^2 a_s}{m}, \tag{1.31}$$

where a_s is the s-wave scattering length who is positive for repulsive interaction and negative for attractive interaction. In the case of ^{87}Rb, the $|F=2,\, m_F=2\rangle$ and $|F=1,\, m_F=-1\rangle$ magnetic trappable states of ^{87}Rb, the s-wave scattering length was measured $a_s = 5.45 \pm 0.26\,\mathrm{nm}$ [63]. In some atoms it is possible to manipulate the scattering length by means of Feshbach resonance [61, 62].

1.3.5 The Gross-Pitaevskii equation

In (Equation 1.28) we have replaced the operator $\hat{\Psi}_0(\mathrm{r},t)$ with the classical field $\Psi_0(\mathrm{r},t)$; such replacement is feasible only if we assume that the function $\Psi_0(\mathrm{r},t)$ varies slowly within the distance range of the inter-atomic force; using the same argument one can also substitute r′ for r. Applying these changes to (Equation 1.25) using (Equation 1.30) gives

$$i\hbar\frac{\partial}{\partial t}\Psi_0(\mathrm{r},t) = \left(-\frac{\hbar^2\nabla^2}{2m} + V_{ext}(\mathrm{r},t) + g_{3d}\left|\Psi_0(\mathrm{r},t)\right|^2\right)\Psi_0(\mathrm{r},t), \tag{1.32}$$

where the density of the condensate is $n(\mathrm{r}) = |\Psi_0(\mathrm{r},t)|^2$. Now we can define a phase of the the order parameter

$$\Psi_0(\mathrm{r},t) = \sqrt{n(\mathrm{r},t)}\mathrm{e}^{\mathrm{i}S(\mathrm{r},t)}, \tag{1.33}$$

where the velocity of the condensate flow can be defined as $\mathrm{v}_s(\mathrm{r},t) = \frac{\hbar}{m}\nabla S(\mathrm{r},t)$, which turn out to be irrational ($\mathrm{curl}\,\mathrm{v}_s = 0$).

Inserting (Equation 1.33) into (Equation 1.32) would give explicit equation for the phase out of the order parameter

$$\hbar\frac{\partial}{\partial t}S + \left(\frac{1}{2}m\mathrm{v}_s^2 + V_{ext} + gn - \frac{\hbar^2}{2m\sqrt{n}}\nabla^2\sqrt{n}\right) = 0, \tag{1.34}$$

the right hand side containing the gradient of the density. This term is called the 'quantum pressure' term and is a direct consequence of the Heisenberg uncertainty principle.

In the case of stationery solutions, the Gross-Pitaevskii equation (GP) can be reduced to much simpler form if we set the time dependence of the wave-function as [54]

$$\Psi_0(\mathrm{r},t) = \Psi_0(\mathrm{r})\exp\left(-\frac{\mathrm{i}\mu t}{\hbar}\right), \tag{1.35}$$

then we can rewrite the GP equation as

$$\left(-\frac{\hbar^2\nabla^2}{2m} + V_{ext}(\mathrm{r}) - \mu + g_{3d}\left|\Psi_0(\mathrm{r})\right|^2\right)\Psi_0(\mathrm{r}) = 0 \tag{1.36}$$

where we assume that the external potential is time independent. The GP equation is a non-linear version of the Schrödinger equation. This non-linearity arises from the interaction among particles and introduce analogy between BEC in atomic gases and and non-linear optics [54].

1.3.6 The Thomas-Fermi limit

When the density of the gas changes slowly in space the quantum pressure term in (Equation 1.34) proportional to $\hbar^2$ and can be neglected. We can introduce a parameter, R, which characterize the density variation in the system. In the case of the ground state R can be the size of the condensate, or the wavelength of the density oscillation in the case of time dependent configurations. The quantum pressure term scales as $\nabla^2\sqrt{n}/\sqrt{n} \sim R^{-2}$ and, becomes negligible if R becomes much larger than the healing length

$$\xi = \frac{\hbar}{\sqrt{2mgn}}, \tag{1.37}$$

which is the distance over which the wave function tends to be at its bulk value when subjected to a localized perturbation [64]. Comparing the healing length with the average distance between particles, $d = n^{-1/3}$, gives an interesting result

$$\frac{\xi}{d} = \frac{1}{\sqrt{8\pi}}\frac{1}{\left(na_s^3\right)^{1/6}}. \tag{1.38}$$

The ratio increases as the volume of the gas decreases [54]; this is due to the quantum nature of the condensate. Another interesting phenomenon that relates to this limit is seen by looking at the spatial density of the condensate. If we neglect the quantum pressure term in the in (Equation 1.34) the equation for the gradient of the phase would be

$$m\frac{\partial}{\partial t}\mathrm{v}_s + \nabla\left(\frac{1}{2}m\mathrm{v}_s^2 + V_{ext} + gn\right) = 0. \tag{1.39}$$

Using the classical Euler equation for potential flow of a non-viscous gas, the pressure would be $P = gn^2/2$ and the sound velocity would be

$$c = \sqrt{gn/m}. \tag{1.40}$$

In the Thomas-Fermi approximation, if we take v_s to be zero or we would neglect the kinetic term in (Equation 1.36) the GP equation would reduces to [54]

$$gn\left(\mathrm{r}\right) + V_{ext}\left(\mathrm{r}\right) = \mu, \tag{1.41}$$

where μ is the ground state chemical potential. In the absence of an external field the chemical potential would be given by the Bogolyubov relation $\mu = gn$.

2 Optimisation of Atomic Imaging

2.1 Introduction

The way we perceive the world is largely dominated by a very complicated organ called eyes. Differently than other methods, vision allow us to understand complicated shapes and structures in a glimpse of an eye. BEC in dilute atomic gases allows a great amount of quantitative information to be extracted by a simple spatial image. Therefore a high quality imaging system is important so that all needed information can be extracted. As in any other measurement device, the signal to noise ratio (SNR) has fundamental importance once it comes to details, especially in very dense atomic samples such as in in situ images. In this chapter we will begin with the theory of imaging (sec. 2.2), continue with atom light interaction (sec. 2.3), we will understand the different noises that relate to atomic imaging (sec. 2.3.1), and investigate theoretically (sec. 2.3.2) and experimentally (sec. 2.4) what should be the optimum light intensity for each atomic density. The latter will show surprising results.

2.2 The Imaging System

High quality imaging allows us to gather more data out of the atomic cloud. Having reliable density distribution of the atomic cloud either while trapped, i.e., in situ imaging or during a ballistic expansion (time of flight, TOF), is a crucial aspect in high-end experiments [65]. In this section we would learn about our imaging system both in Nottingham and in BGU and look at the advantages of each of the systems.

Technical implantation

Our imaging setup is shown in (Fig. 2.1). The probe beam is along the $\hat{y}$ axis, which is orthogonal to the long axis of the cloud, so we image the $\hat{x}$ and $\hat{z}$ axes. This allows us to get the density distribution along the quantization axis. The imaging beam shines through the chamber and the atomic sample is then directed via a lens system to a CCD Camera. We have the flexibility to choose a different magnification by

easily changing the lens system. The imaging technique we are using is absorption imaging [65]. This is the most common method to image ultra-cold atomic clouds, where a coherent and resonant light is shone on an atomic sample while the detection is done by comparing the shadow left by the cloud to an identical beam without that shadow.

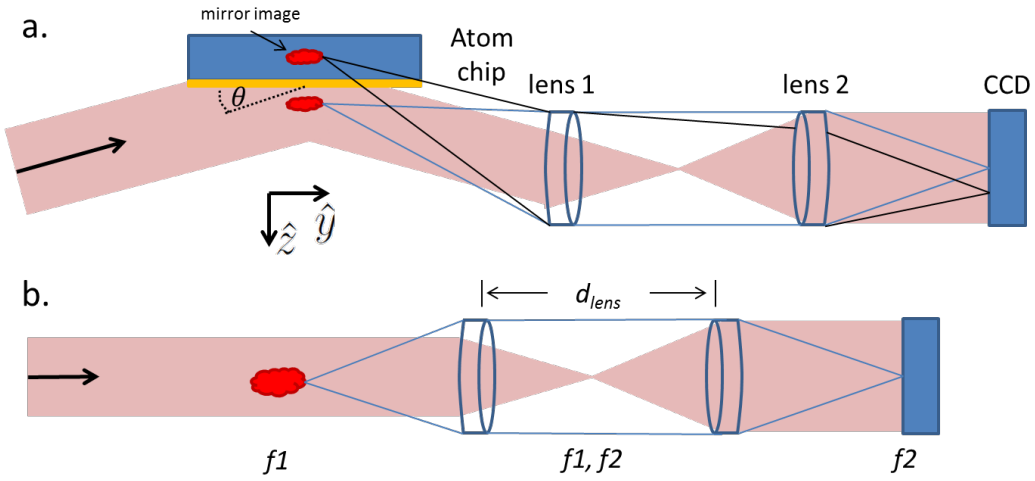

Figure 2.1: The imaging system design (not to scale). The pink line represents the probe beam while the lines show the shadow created by the atomic cloud. (a) "Grazing Incidence Imaging", The probe beam has two paths, the direct one where the probe beam reflects from the chip through the atomic cloud. While the second is the mirror image path where the first incidence of the probe beam in the cloud is then reflected by the atom chip surface. The distance between the two shadows on the CCD, d, gives the cloud's distance from the atom chip $\left(h = \frac{d}{2\cos\theta}\right)$. (b) "Time of Flight Imaging" is mainly used where the atoms are farther away from the chip as in TOF imaging where the atoms' distance is measured from the chip structure directly.

In our system the cloud is set at the focal point of the first lens ($f1$) where the distance between the two lenses is the sum of the focal distances ($d_{lens} = f1 + f2$). The CCD is exactly at the focal point of the second lens ($f2$). By using ray geometry one can see that while keeping the atoms at the focal point of the first lens and the CCD at the focal point of the second, any given distance between the lenses, d_{lens}, would give the same magnification both for the shadow and the probe beam without the shadow. The problem in setting $d_{lens} \neq f1 + f2$ is that the probe beam is uncollimated and its image is blurred (a projection of a circular wave-front over a straight screen and the numerical aperture of the system).

In Nottingham we used "Time of Flight Imaging", where the atomic cloud is at the order of 1 mm; therefore we use the imaging system to reduce the cloud size on the CCD screen to half of its size. The minimal distance between the cloud and

the first lens is limited by the vacuum chamber to minimum 100 mm. Therefore the first lens we used is Thorlabs AC508-150-B $f_1 = 150$ mm, Ø50.8 mm Near IR Achromat, while the second lens is Thorlabs AC508-075-B$f_2 = 75$ mm, Ø50.8 mm Near IR Achromat. These lenses are designed to be near diffraction limited at 780 nm. In the given demagnification case the image maximal numerical aperture, NA, is limited by the view-port and distance from the chip, which reduces the resolution, to $NA_1 \approx \frac{D}{2f} = \frac{18}{2 \cdot 100} = 0.09$ in air, where D is the clear view diameter (see our imaging Fig. 2.2).

The BGU setup is well presented in the thesis of Shimon Machluf from Ron Folman's Atom-Chip Lab [66]. In the experiment that was done there we imaged BEC clouds in close proximity to the chip surface; therefore we used Grazing Incidence Imaging system. The incident beam was calibrated to about $\theta \approx 1.5°$ (see Fig. 2.1). The first lens used is Thorlabs AC508-200-B $f_1 = 200$ mm, Ø50.8 mm Near IR Achromat, while the second lens is Thorlabs AC508-300-B $f_2 = 300$ mm, Ø50.8 mm Near IR Achromat, and the maximal numerical aperture is similar.

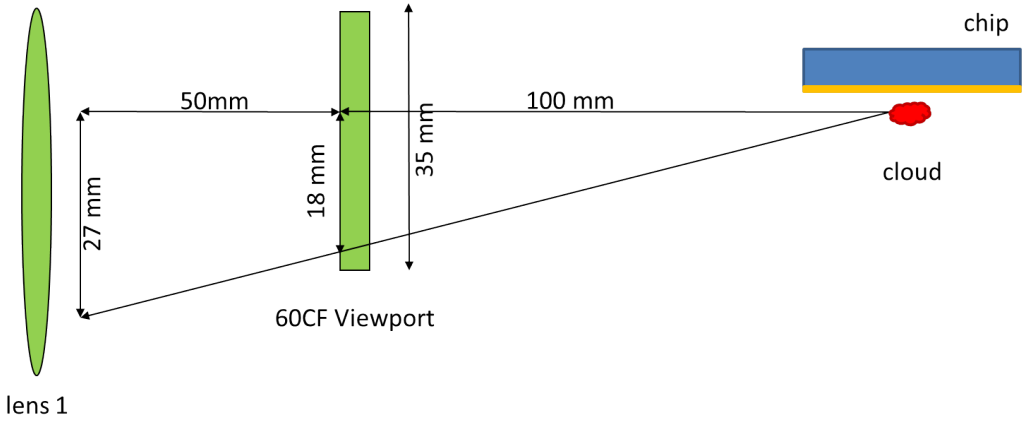

Figure 2.2: A sketch of the apparatus in Nottingham (not to scale). While imaging from the vacuum chamber side view-port the chip and view-port limit the maximal numerical aperture of the system. The maximal numerical aperture that can be achieved under these conditions is $NA_1 \approx \frac{D}{2f} = \frac{18}{2 \cdot 100} = 0.09$ in air, from which the minimal diffraction limit would be $r = 0.61\frac{\lambda}{NA} = 5.28\,\mu$m. This limit reduces the ability to perform experiments that demand very high resolution. Current novel techniques, such as light sheet imaging, allow single atom imaging ability in similar UHV apparatus [67].

Characterization of the imaging system

The resolution of an imaging system is defined by the minimal possible distance to resolve two points using a circular aperture. This minimal distance is called the Abbe diffraction limit and is defined by the Rayleigh criterion. The criterion

is satisfied when the central maximum of the Airy Disk of one imaged point falls below the first minimum of the other, i.e., $r = 1.22\frac{\lambda f}{D} = 0.61\frac{\lambda}{NA}$, where λ is the radiation wavelength. In many cases the effective pixel size (pixel size divided by the magnification) is larger than the diffraction limit; therefore it will set the resolution limit. In our system the minimal diffraction limit is $r \approx 5.28\,\mu$m (see Fig. 2.2).

Camera

The camera we used in Nottingham is The Image Source DMK 21BU04, which Is an 8 bit camera with pixel size of $5.6 \times 5.6\,\mu$m. The quantum efficiency is not directly specified in the chip data sheet [68]. Given the magnification the effective pixel size is $11.2 \times 11.2\,\mu$m.

In BGU we used a Prosilica GC2450 camera with pixel size of $3.45 \times 3.45\,\mu$m [69]. It has a bit depth of 12 bits and quantum efficiency at 780 nm of 17%. With magnification of $^{300}/_{200}$ the effective pixel size is $2.3 \times 2.3\,\mu$m. For both cameras further data can be found in the chips data sheet [68, 69]. Also for both cameras the dark current and noise levels are much higher than with cryogenic cameras such as the Andor iXon.

2.3 Theory of Imaging

In this section we will first explain the basics of absorption imaging, later we will explore the effect of quantum noise on our imaging system and how to optimize the imaging light intensity.

Absorption of light in a dilute matter

The decay of light through atomic medium can be illustrated as

$$\frac{dI}{dy} = -n\left(y\right)\sigma\left(y\right)I, \tag{2.1}$$

where $n\left(y\right)$ is the density of atoms and $\sigma\left(y\right) = \sigma_0/\left[1 + s\left(y\right) + \delta^2\right]$ is the cross-section that can be defined as the power radiated by the atom divided by the incident energy flux. The cross-section includes the saturation parameter $s\left(y\right)$; this parameter has dependency in y since it becomes smaller with distance inside the cloud [70]. The resonant cross-section $\sigma_0 = \frac{\alpha_{CG}3\lambda^2}{2\pi}$ [71] to which we add the prefactor α_{CG} obtained by the average squared Clebsch–Gordan coefficients. The relevant Clebsch–Gordan coefficients are determent by the populated and excited Zeeman sublevels and light polarization.

If we are only interested in the initial and transmitted light (while neglecting fluorescence effects) we can simplify the formula to the transmission, $T_{in} = I_{in}/I_0$, of the column density n so [70]

$$T_{in} = \frac{1+\delta^2}{s_0} W\left[\frac{s_0}{1+\delta^2}\exp\left(\frac{s_0 - n\sigma_0}{1+\delta^2}\right)\right], \tag{2.2}$$

were W is the Lambert function of the first kind (gives the principle solution for w in $z = we^w$), $\delta = \frac{\omega-\omega_0}{\Gamma/2}$ is the normalized detuning, and $s_0 = I_0/I_{sat}$ is the normalized initial intensity (see Fig. 2.3). For either $s_0 \ll 1$ or $n\sigma \ll 1$ we can reduce (2.2) to the Beer-Lambert law $n = -\frac{1}{\sigma}\ln(T)$.

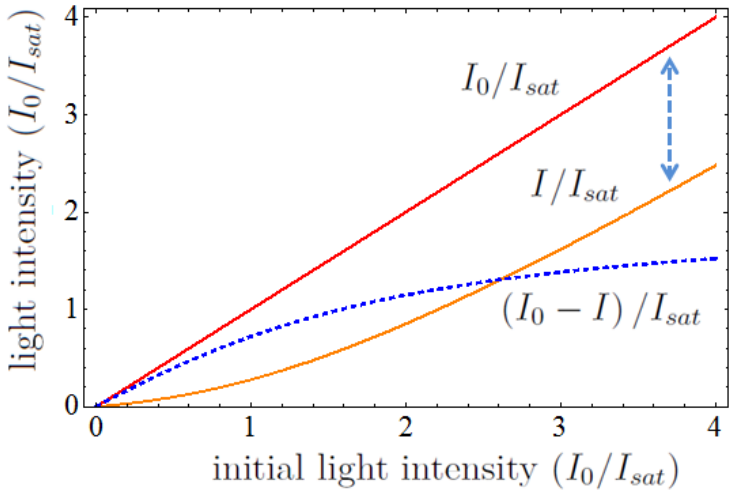

Figure 2.3: The light intensity before and after a ^{87}Rb atomic cloud at the ground-state as calculated by (2.2). The light was considered as resonant and the atomic column density was set to $n\sigma_0 = 2$. In red is the initial light intensity normalized by the saturation intensity I_0/I_{sat}. In Orange is the normalized light intensity after the atomic cloud, I/I_{sat}, while in dashed blue is the difference between the two intensities $(I_0 - I)/I_{sat}$. Due to the quantum nature of matter the transmission of light is not linear but increases with intensity. Once the light intensity reaches the local saturation value we cannot approximate the absorption as linear and need to calculate by the full derivation given in (2.2).

Absorption imaging

Absorption imaging is the workhorse of atomic physics. Using this technique we take three images using a CCD camera through a lens system. Once one decides to image the atomic cloud a resonance laser light is shone via the atomic cloud towards the camera. The cloud absorbs some of the light and creates a shadow in the original

laser profile; this shadow can be presented as a source (absorption image). As a function of the laser pulse duration and intensity a momentum kick is given to the atoms. After some time a second laser pulse is shone, this time the atoms are gone due to the previous heating process and an image of the laser beam profile (flat-field) is taken. A third background image is taken after some time without shining the laser light as a reference of the environment (dark-field).

During the absorption image a small fraction of the of the fluorescence emitted by the atoms is shone at the solid angle of the CCD, θ_{im}. Since we image the light intensity dip, the fluorescence would reduce the absorption dip, also this light won't be coherent with the imaging beam. Each of the photons that is absorbed by the atoms is emitted spontaneously; therefore we can rewrite (2.1) as $\frac{dI_T}{dy} = (\theta_{im} - 1)\, n(y)\, \sigma(y)\, I_T$. Solving this equation would give a corrected result for (2.2)

$$T = \frac{1+\delta^2}{s_0} W\left[\frac{s_0}{1+\delta^2} \exp\left(\frac{s_0 - n(1-\theta_{im})\,\sigma_0}{1+\delta^2}\right)\right], \tag{2.3}$$

for $NA = 0.09$ the spontaneous emission would give a factor of $(1 - \theta_{im}) = 0.82$. The corrected transmission would be related to the three images taken in the following way:

$$T = \frac{I - I_{bg}}{I_0 - I_{bg}}, \tag{2.4}$$

where the normalized initial intensity will be redefined to its real value $s_0 = \frac{I_0 - I_{bg}}{I_{sat}}$. The background light, I_{bg}, is an imaging artifact due to the stray light that shines on the CCD; it is not related to the imaging laser light, therefore it needs to be subtracted. From (2.3) we can extract the column density per pixel (for any cloud that is larger than the diffraction limit) as

$$n = \frac{1+\delta^2}{(1-\theta_{im})\,\sigma_0}\left[\frac{s_0}{1+\delta^2}(1-T) - \ln(T)\right]. \tag{2.5}$$

In relation to (2.1) the light intensity at the absorption image, I, is

$$I(x,z) = I_0(x,z)\, e^{-OD(x,z)}, \tag{2.6}$$

where $I_0(x,z)$ is the laser profile obtained by the second image (without atoms), and $OD(x,z)$, the optical density, is given by

$$OD(x,z) = \sigma n(x,z), \tag{2.7}$$

where $n(x,z) = \int dy\, n(x,y,z)$ is the integrated density of the cloud along the laser path and $\sigma = \frac{\sigma_0}{1 + I_0/I_{sat} + \delta^2}$. For near resonant light in ^{87}Rb, $I_{sat} = 1.6\,\mathrm{mW/cm^2}$.

The optical density can be subtracted from the three images

$$OD(x,z) = \frac{I_0(x,z) - I(x,z)}{I_{sat}} - \ln\frac{I(x,z) - I_{bg}(x,z)}{I_0(x,z) - I_{bg}(x,z)}, \tag{2.8}$$

and from which we can calculate the atomic density by dividing the result by the cross-section, σ_0. Optical density above four means that the transparency is below 2%, which is the too low for most imaging systems. Finding the optimal light intensity taking into account quantum noise effects will be explained in the following section.

2.3.1 Noise calculations

In this section we will review the different noises that affect absorption imaging and review their effect. First we will define the noise from the camera and later the noise that relates to the atoms' light interaction.

Photon noise

Photon noise, also known as photon shot noise, comes from the quantum nature of light. For a given steady source of photons the total number of photons emitted in a given time interval varies according to a Poisson distribution[1], so the noise is equal to the square root of the signal. Since the noise is part of the quantum nature of light this noise will always be present in the imagining system.

Preamplifier noise

Preamplifier noise is also known as read noise and is generated by the on-chip output amplifier. Choosing the right operating condition of the camera can drastically reduce this noise.

Dark current

The source of this noise is thermal and usually appears in photosensitive and charged coupled devices. This noise becomes significant when no photons enter the device and a pattern of noise appears. The pattern can be removed but a temporal noise will remain since the dark current in nature is shot noise. Dark current can be reduced drastically by cooling the CCD to reduce thermal effects. This effect is less significant in short exposure times.

[1] Technically squeezed light would behave differently, such as in amplitude squeezed light where the photon number distribution is sub-Poissonian and the phase distribution is wider.

Spurious Charge

Spurious charge is usually generated on the leading edge of the drive clock when binning is required, when the drive clock[2] phase assumes the non-inverted state[3], and holes are forced back to the channel stop regions[4]. Only the leading edge of the clock (raising signal) and not the falling edge (fallng signal) generates this noise in the CCD. The noise increases exponentially when the clock rise time and voltage vary since it sends holes back to the channel stop. Also, clocks that move fast in high amplitude would increase impact ionization.

To avoid this noise all the drive clocks need to be optimized so the holes will be able to go back to the channel stop as slowly as possible, and the horizontal clocks in the CCD need to be operated in non-inverted mode if we can ignore dark current in the system.

Atomic noise

In cold atomic samples the variance of the atomic number is comparable to shot noise and the bunching behavior of Bosons [71]. To measure the variance in atom number, first we need to acquire a large number of shots in similar experimental conditions. For large amounts of shots the technical noise of the experiment is averaged down. The variance in measured atom number per pixel, which incorporates the atomic noise and photon shot noise, is

$$\delta n\left(x,z\right)_{atom}^{2}=\left[n_{i}\left(x,z\right)-\alpha_{i}\bar{n}\left(x,z\right)\right]^{2}, \tag{2.9}$$

where $\bar{n}$ is the mean value of atoms, and α is a normalization factor. Since every shot has a bit different atom number we use α to to deduce from the measured atom number only the average atom number. This is done by measuring the total number of atoms in the image, N, divided by the average total atom number $\alpha = N/\bar{N}$. The corrected atomic variance is achieved after abstracting the photon shot noise per image than all images are binned.

In the case of non-degenerate quasi-1d gas $\left(\frac{n}{A}\lambda_{dB}\ll 1\right)$, where A is the pixel area, the variance due to atomic noise would be [71]

$$\left\langle n^{2}\right\rangle -\left\langle n\right\rangle ^{2}=\left\langle n\right\rangle +\left\langle n\right\rangle ^{2}\frac{\lambda_{dB}}{\sqrt{2}A}\tanh^{2}\left(\frac{\hbar\omega_{\perp}}{2k_{B}T}\right). \tag{2.10}$$

[2]Multiple timing signals ("clocks") transport electrical charge across the CCD array to a sense amplifier for conversion into image data. The parameters of these clocks (clock rate, pulse width, pulse amplitude, rise- and fall-times, etc.) greatly influence the behavior and performance of the imaging device.

[3]In inverted mode two of the three electrodes defining a pixel are driven into inversion to drastically reduce the dark current.

[4]Channel stop regions isolate the charge packets in one column from those in another.

The first term on the right-hand side is due to shot noise, and the second term is due to bunching. The bunching term in the non-degenerate gas case decays rapidly because of the Gaussian decay nature of correlation. We should remember that this equation is true as long as the effective pixel size is bigger than the correlation length.

If the sample is "hot", i.e., the bunching term is negligible; the main contribution to the variance would come from the atomic shot noise fluctuations. That means that the variance would increase linearly with mean atom number. From experiments we found that the slope of the variance is not one as expected but rather smaller [71]. This reduction happens if the pixel size is smaller than the resolution of the imaging system. Full explanation on the nature of atomic noise and coherence is given in (chapter 3).

2.3.2 Optimized light levels in absorption imaging system

The photon shot noise is the main source of noise per shot, since atoms have nonlinear response to light while measuring noise levels in absorption imaging, we should use (2.5) and not a shorter version of it. Also, while summing many shots we should account for the atom noise donation to the variance (2.9). Since the main goal of this section is to find the optimal light intensity, I_0, for absorption imaging, in this section we will ignore the atom-related noise (i.e., treat the atom number as constant) and concentrate only on light related noise.

In absorption imaging we take three shots: absorption image, flat-field, and dark-field. In the first two shots we shine light with supposedly identical intensity and profile, while in the latter we don't shine any light; therefore we will ignore it in the theory part. Since the distribution of light per pixel is Poissonian in nature, the photon shot noise is the square root of the photon number. We will derive the error in the measured atom number (2.5) due to the light shot noise in the absorption image after the atoms, I, and at the flat-field image I_0

$$\delta n = \sqrt{\left[\left(\frac{\partial n}{\partial I_0}\Delta I_0\right)^2 + \left(\frac{\partial n}{\partial I}\Delta I\right)^2\right]}, \tag{2.11}$$

where the light intensity per pixel is converted to photon number and ΔI_0 and ΔI equal $\sqrt{I_0}$ and $\sqrt{I}$, respectively. The solution of (2.11) for resonant light and no fluorescence is $\delta n = \frac{1}{\sigma_0}\sqrt{\left(\frac{1}{I_{sat}} + \frac{1}{I_0}\right)^2 I_0 + \left(\frac{1}{I_{sat}} + \frac{1}{I}\right)^2 I}$, where for the theoretical calculation we take $I = I_0 T$ (2.3). We set the SNR per pixel to be the atom number divided by the variance (see Fig. 2.4)

$$SNR = \frac{n}{\delta n^2}. \tag{2.12}$$

The maxima of the SNR represent the optimal light intensity for a given density. In Fig. 2.5 the red line represents the optimal image light intensity as a function

of the atomic density, $n\sigma_0$; for low densities the ratio is linear and can be fitted numerically.

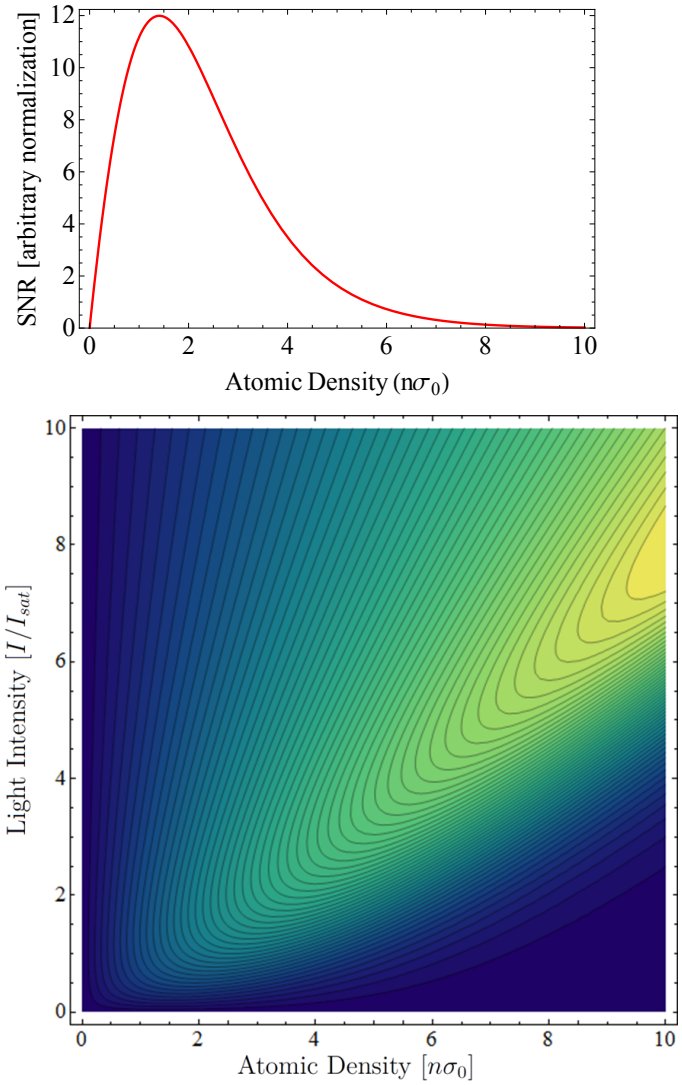

Figure 2.4: On the top axis is the SNR for a fixed resonant light intensity of $I_0 = 0.1I_{sat}$; the maxima is at $n\sigma_0 = 1.42$, the optimal atomic density for the given light intensity. On the botom is a contour plot of the SNR as a function of the atomic density and light intensity. The ridge in the plot maps the optimal SNR line; a trace over the optimal value given by this plot is presented in Fig. 2.5.

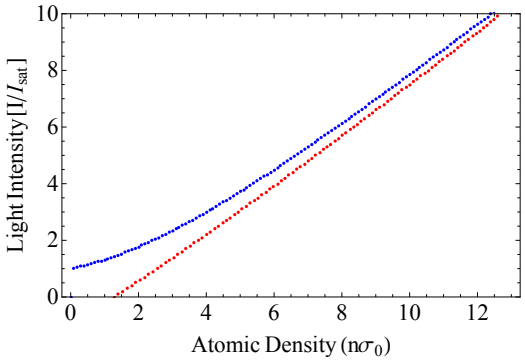

Figure 2.5: In this plot we present the optimal SNR for either chosen light intensity or atomic density. The blue line shows the optimal light intensity for a given atomic density while tracing the SNR ridge in Fig. 2.4. From this calculation it is seen that even for minimal atomic density (single atom) the optimal light intensity is about I_{sat}. The red line shows the optimal atomic density for a chosen light intensity. For many camera types it is impossible to use imaging light at saturation intensity or above due to technical limits; therefore we wanted to see what would be the optimum SNR while limiting the light level. The red line is linear and intersects with the blue curve at an atomic density of about five as expected. The linear line follows the equation $n\sigma_0 = \frac{I/I_{sat}+1.0434}{0.8044}$. One should remember that we took the cross-section to be $\sigma_0 = \frac{3\lambda^2}{2\pi}\alpha_{CG}\,(1-\theta_{im})$ as explained in sec. 2.3.

2.4 Experimental Results

Camera calibration

Calibrating the camera is an important aspect in any imaging-dependent experiment. In this section we will explain the ways we have used to perform this calibration.

The first important part in any calibration is to find the ratio of photo-electrons to grey-index, a good technique to use is by means of photon shot noise. A coherent flat-field light beam follows Poisson distribution, so $\delta N^{ph} = \sqrt{\bar{N}^{ph}}$, where $\bar{N}^{ph}$ is the average photon number in that volume (pixel). This statement is not sufficient in the case of a thermal light source that follows Bose-Einstein distribution. The standard deviation for such light is [72]

$$\delta N^{ph} = \sqrt{\bar{N}^{ph}\left(1+\frac{\bar{N}^{ph}}{t/t_c}\right)}, \tag{2.13}$$

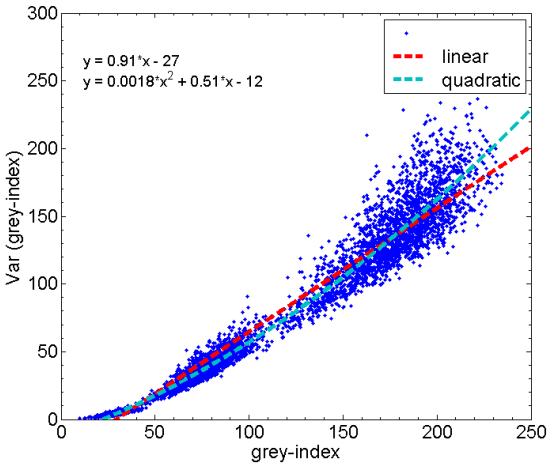

Figure 2.6: Noise measurement with pulsed laser beam. Half the variance of the difference vs. mean value in grey levels. Fit function gives the conversion coefficient from grey-index to photo-electron number. A linear and quadratic fit is presented where the quadratic fits better.

where t is the imaging time and t_c is the coherent time of the light source. In our experiment $t = 100\,\mu$s and $t_c \approx 1\,p$s for a narrow band light source. Since in our experiment $\frac{\bar{N}^{ph}}{t/t_c} \ll 1$, we can treat light as Poissonian.

We measured the flat-field light intensity per pixel over many shots and found the average intensity and the standard deviation per pixel in gray-index values.

$$N^{ph} = \sigma_{camera} I, \tag{2.14}$$

where I is the gray-index and σ_{camera} is the photon-electron conversion factor (which incorporates the quantum efficiency). The Poissonian noise is $\delta N^{ph} = \sigma_{camera}\sqrt{I}$, and therefore $\left(\delta N^{ph}\right)^2 / \bar{N}^{ph} = \sigma_{camera}$ (see Fig. 2.6). In the presented figure the camera conversion is quadratic instead of linear as if at higher intensities of light, i.e more electrons per well, the technical noise increses. Superior quality cameras won't have such behavior.

The second stage of calibration is a full conversion between photons to grey-index, which includes the quantum efficiency of the camera. To do so we have put an out-cuppler, which produces a beam-waist half the size of the CCD size. We have measured the out-cuppeled light from the fiber in constant mode and during the duty cycle ($100\,\mu$s imaging pulse). We have found a 20% difference in intensity between the two for the same in-cuppled laser intensity. This is due to difference in performance of the AOM in pulsed or continues mode. We have averaged about 50 shots per intensity to find a correct grey-scale to photon rate and repeated the experiment over several intensities. For each light intensity we have converted the total intensity to photon number as follows, $N_T = I_T \frac{\lambda t}{hc}$, where $t = 100\,\mu$s is the

pulse duration and $\lambda = 780.4\,\mathrm{nm}$. Later we used these ratios in an averaged way as a conversion rate. Since the camera is non-linear in intensity and we could only use the total light intensity per image to get a conversion factor, an error in calculated photon and atom number is expected.

Experimental procedure

Our imaging system is built as presented in (Fig. 2.7). The imaging laser light comes from polarized maintaining optical fiber that guides light to a collimating out-coupler that increases the Gaussian shape of light to a diameter of $1'\emptyset$. We can measure the total light intensity from the out-coupler and also modify the light intensity using a $\lambda/2$ plate and polarizing beam splitter that are set before the fiber coupler.

First we measure the total light intensity from the fibre. Knowing that the beam waist is $\omega_0 = 10.15\,\mathrm{mm}$, we can integrate over a Gaussian wavefront with such waist to calculate the total light intensity on the CCD. We have taken 7 series of 300 images at total light intensity between $630\,\mu\mathrm{W}$ and the intensity edge of the camera $3.90\,m\mathrm{W}$; these values gave rise to minimum and maximum intensities per pixel of $0.1 \times I_{sat}$ to $1.9 \times I_{sat}$, respectively.

We used a MOT cloud of 1×10^8 atoms at a temperature of $40\,\mu\mathrm{K}$, and distance of 4 mm from the chip surface. About 300 shots were taken for each light intensity, where the imaging beam and camera were centred directly on the atomic cloud. Later we filtered out all the shots that the light intensity difference between the absorption image and flat-field, at a region without atoms, was greater than 5%. For each shot we took a line vector at the center of the cloud that binned three pixels ($33.6\,\mu\mathrm{m}/3$) in the vertical direction. The mean atom number was calculated per pixel on the line vector. Due the short sequence time long-term drifts are negligible.

Given the approximate cross-section, σ_0, the atom number per pixel is

$$N = \frac{\Delta^2}{\sigma_0}\left(\frac{I_0 - I}{I_{sat}} - \log\left(\frac{I}{I_0}\right)\right), \tag{2.15}$$

where σ_0 incorporates the relevant spontaneous emission factors and Clebsch–Gordan coefficients. For each image variance we can form a quantity that is due to the photon shot noise

$$\delta N\left(x\right)_{ph}^2 = \sum_z \left[\left(\frac{1}{N_{sat}} + \frac{1}{N_1^{ph}}\right) + \left(\frac{1}{N_{sat}} + \frac{1}{N_2^{ph}}\right)\right]\left(\Delta^2/\sigma_0\right)^2, \tag{2.16}$$

where $\Delta \times \Delta$ is the pixel area in the object plane, and N_{sat} is the photon number per pixel at saturation intensity (see Fig. 2.8 left). The signal to noise ratio as set in (2.12) is (see Fig. 2.8 right)

$$SNR\left(x\right) = \left\langle N\left(x\right)/\delta N\left(x\right)_{ph}^2 \right\rangle \tag{2.17}$$

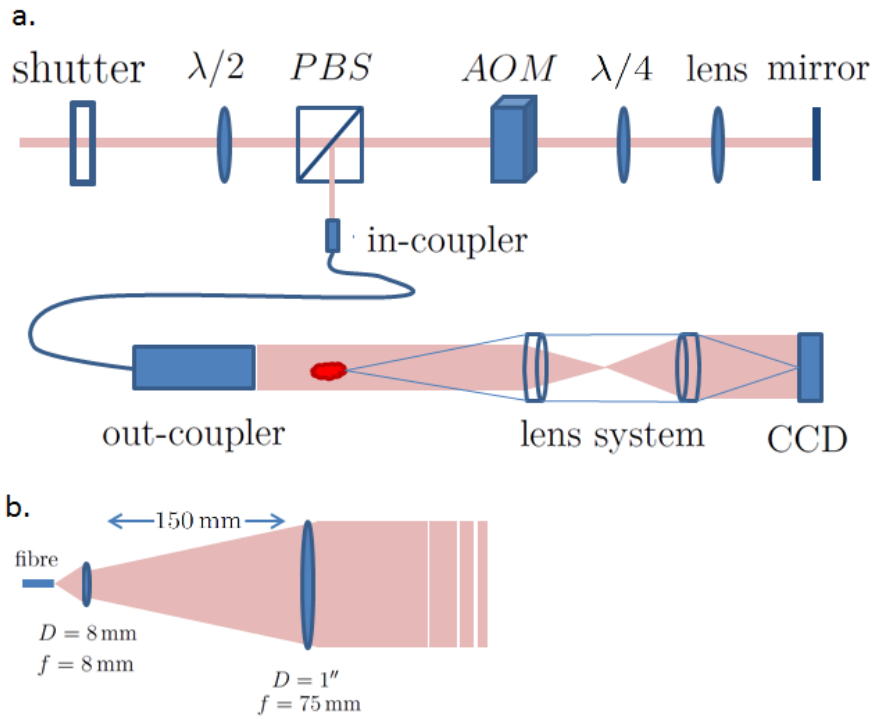

Figure 2.7: A sketch of our imaging system. a. The laser light is split from the cooler laser beam to the imaging system; we can set the imaging beam intensity and its frequency using the double pass AOM and PBS. The light is coupled to a polarization maintaining fiber where its out-coupled collimated beam waist is $1''$ in diameter, the beam shines via the atoms through a lens system to a CCD camera. b. A scheme of the fibre out-coupler where we increase the beam size to $1''\,\emptyset$ with waist of $\omega_0 = 10.15\,\text{mm}$. A full explanation of our lens system and absorption imaging is given in sec. 2.2 and sec. 2.3.

In both plots the top $x-$axis is the atom number per pixel, N, as shown for on-resonant light, while the bottom one represents the atomic density $AD = N\sigma_0/\Delta^2$. As seen by (2.17) the SNR was calculated per line vector and only after an average over all the line vectors was done.

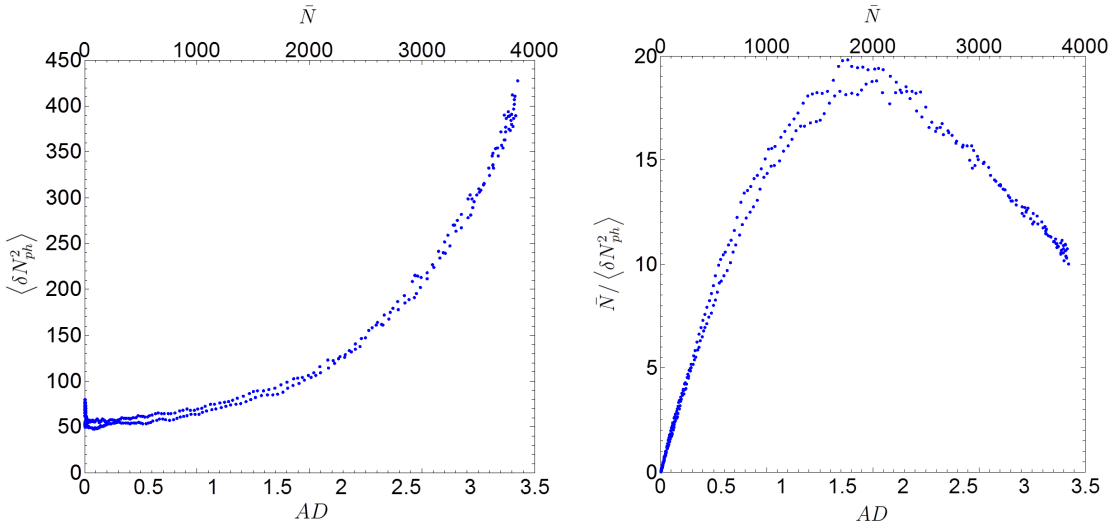

Figure 2.8: Plots of variance of calculated atom number and SNR as a function of top-axis: the mean atom number per pixel. Bottom-axis: the atomic density. The atom number is set as $N = \frac{\Delta^2}{\sigma_0}\left(\frac{I_0 - I}{I_{sat}} - \log\left(\frac{I}{I_0}\right)\right)$ where the relevant pixel area in the object plane is given by Δ. The cross-section, σ_0, includes the relevant Clebsch–Gordan coefficients and reduction due to spontaneous emission of the atoms to the imaging solid angle. The average light intensity was $\frac{\bar{I}_0}{I_{sat}} = (30.8 \pm 5.7)\,\%$ where the fluctuations in both plots are mainly due to constant spatial differences in light intensity. Left: the variance of the calculated atom number (2.16) as a function of the mean atom number per pixel. Where $N_{1,2}^{ph}$ are the number of photons in the absorption image and flat field image (per pixel), respectively, where x represent a given pixel on a line vector, i.e., mean atom number. As expected, for a given light intensity the variance increases with the atomic density. Right: the signal to noise ratio $SNR = \bar{N}/\left\langle \delta N_{ph}^2 \right\rangle$ as a function of the mean atom number. The plot shape is similar to that in Fig. 2.4, where the maxima is around $n\sigma_0\,(max) \approx 1.67$ (from a polynomial fit), which is about the theoretical value for the optimal value for this light intensity found in Fig. 2.4 ($n\sigma_0 = 1.68 \pm 0.07$).

The average light intensity was set to $\bar{I}/I_{sat} = (30.8\pm)\,\%$, where the fluctuations seen in both plots are due to spatial constant variations in light intensity. Also, when setting the $x-$axis as AD we actually trace the cloud from one side to the other so if the light intensity is lower at one of the sides we would see the double line figure that is highly visible in the right plot and repeated in the left one. In Fig. 2.9 we present the SNR at two light intensities $\bar{I}/I_{sat} \approx (30.8 \pm 5.7)\,\%$ and $(19.6 \pm 3.6)\,\%$. To find this ratio, I/I_{sat}, we first had to calculate the index value of the saturation intensity; knowing the saturation index, we found the mean light intensity of the line vector over hundreds of shots and from which we took the given ratios. When the ratio is known we could use the linear ratio $n\sigma_0 = \frac{I/I_{sat} + 1.0434}{0.8044}$ to find the theoretical optimal optical density. Along the whole MOT cloud there is a large variety of light intensities and atomic densities; we have analyzed our experimental data in a way

that would allow us to extract the full range of given light intensities and atomic densities for three different data sets, each with a different mean light intensity. In Fig. 2.10 we present the SNR As a function of this data in a three-dimensional plot.

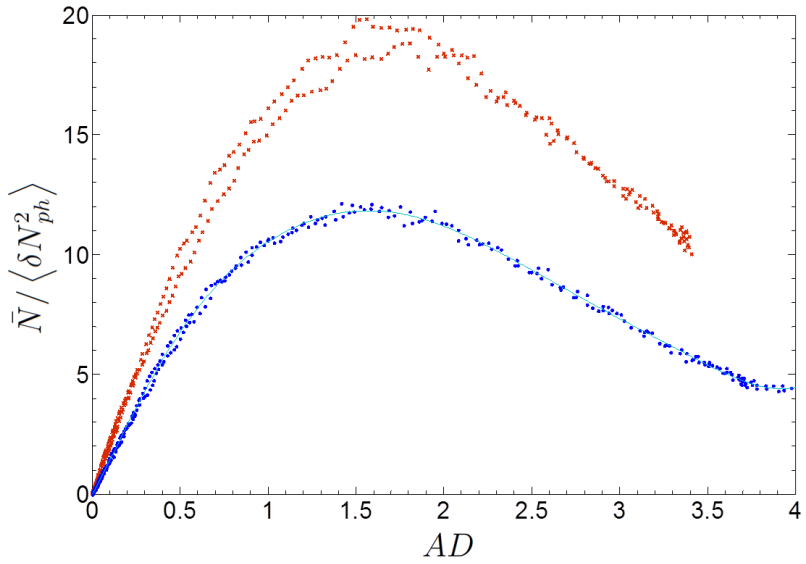

Figure 2.9: Plot of the SNR as explained in Fig. 2.8 at two different light intensities. In red, $\times$, the average light intensity ratio is $\bar{I}/I_{sat} = (30.8 \pm 5.7)\,\%$; in blue, $\bullet$, the average light intensity ratio was $\bar{I}/I_{sat} = (19.6 \pm 3.6)\,\%$. The peak of the SNR was measured to be around $n\sigma_0 \approx 1.67$ and 1.54 (from a polynomial fit) for the red and blue lines, respectively, where the theoretical values are $n\sigma_0 = 1.68 \pm 0.07$ and 1.53 ± 0.05, respectively. From here we can see that there is a good agreement with theory at these light intensities.

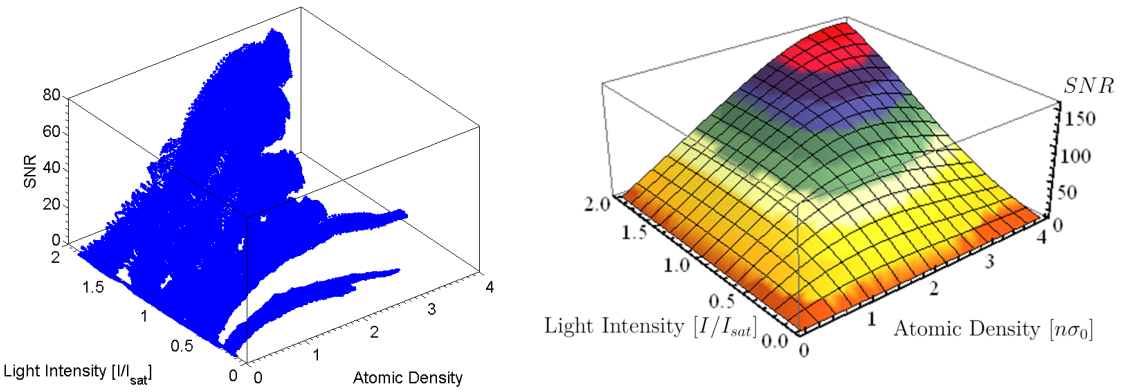

Figure 2.10: A three-dimensional plot of the SNR as a function of light intensity and atomic density. Our experimental data are presented on the left while the theoretical calculation is on the right. It is seen that at the given range the behavior of the experimental data is similar to the theoretical one. We suspect that the difference in SNR value, not shape, is due to technical noises as was observed in Fig. 2.6. Two factors can mainly contribute to the difference in SNR between theory and experiment, first is camera non-linear response as explained in sec. 2.4, where the second is technical noise that add up to the variance of photon number.

Conclusions

In this chapter we aim to find an optimal ratio between the imaging light, I_0, intensity and the atomic sample optical density, $n\sigma$, for absorption imaging. To do so we looked at the theory of absorption imaging and analyzed the Nottingham and BGU imaging systems. In order to reach a formula for optimal light intensity first we had to find the different noise parameters that affect the calculated atom number. Second we had to calibrate our imaging system to take into account the quantum nature of the atomic sample, i.e., saturation effect. Third we found the variance and signal to noise ratios. Knowing the following we have developed a theoretical model that takes into account the different parameters of our experiment, such as the magnification, solid angle of spontaneous emission, the real atomic cross-section, saturation light intensity, and the experimental procedure. From the theoretical model we have found a linear optimal ratio between the given atomic density and light intensity. We took experimental data of about two thousand shots at varied intensity and analyzed the results statistically. We presented the SNR plot at different light intensities and matched its maxima with the theoretical data. A good agreement between the theoretical data and experimental values was found.

3 One dimensional BEC

In this chapter we begin with a brief literature review of low-dimensional Bose gas and introduce important concepts and methods used in this thesis. Later we will realize a 1d system experimentally while investigating different phenomena that are the fingerprints of low dimension condensate.

To begin, in sec. 3.1 we present the theory of (no) BEC in one-dimensional (1d) systems while presenting two important approaches, one is the Bogoliubov frameworks (sec. 3.1) and the other is the complimentary Luttinger liquid approach (sec. 5.1). We explore the effect of dimensionality over the coherence in mean field (sec. 3.1.2) and behind mean field (sec. 3.1.4). Later we investigate the 3d/1d cross over (sec. 3.1.5) and explain how to realize quasi-1d BEC experimentally (sec. 3.2.1).

Further experimental study of quasi-1d BEC is presented in sec. 3.2. To begin, we give a quick overview of the experimental framework (sec. 3.2.2), then we show the effect of evaporative cooling on an elongated BEC (sec. 3.2.3). Later we study the occurrence of phase fluctuations due to thermal excitations in BEC, and the translation of phase perturbations to density ripples as a function of time of flight (TOF), temperature, trap parameters, and atom number (sec. 3.2.4).

In the final sec. 3.2.4, we present the TOF data from the previous section in a unique way, looking at the variance in atom number as a function of the mean atom number per pixel for different flight times. These results show the translation of phase fluctuations to the density profile in a very direct way.

3.1 Theory of BEC in Low Dimensions

Reduction of dimensionality in ultra-cold atomic gases can be achieved by using highly anisotropic trapping potentials. These potentials should have sufficient strong confinement in one or two directions to reduce the motion of the atoms to zero-point oscillations, and as a result the system can be treated kinetically as 1d or 2d. The trapping potential in the remaining directions limits the system's size and changes the level structure of the many body system. In this section we explain the basic theory of Bose condensate in one dimension and go over both theoretical and experimental aspects.

3.1.1 Mean field theory in one-dimension

Mean field theory can be applied to an interacting Bose gas if the atomic density is high enough such that the average distance, d, between atoms is smaller than the healing length, $\xi = \frac{1}{\sqrt{8\pi n a_s}}$ (see 1.37). If the ratio ξ/d is larger than one, the order parameter can be treated classically as in the GP approach to mean field [54]. The mean inter-particle distance in three dimensions is $d_{3d} = n^{-1/3}$, where n is the three-dimensional density. Given the latter, the ratio can be defined as $\xi/d \approx (n a_s^3)^{-1/6}$, which is larger than one only for sufficiently small densities $\left(n < \frac{1}{a_s^3}\right)$.

For regions of lower dimensionality, such as a harmonic cigar shape trap with tight radial trapping frequency, we can treat the atoms as trapped in a cylinder of length L and radially trapped by an harmonic potential $V(r_\perp) = (m/2)\,\omega_\perp^2 r_\perp^2$. In such case the density would reduce to $n_{1d} = N/L$, where N is the total atom number and L is the cloud length. Then $n_{1d} = n\pi a_\perp^2$, where n is the three-dimension density and $a_\perp = \sqrt{\hbar/m\omega_\perp}$ is the radial oscillator length. For this low dimensional case the ratio can be written as

$$\frac{\xi}{d} = \sqrt{\frac{a_\perp^2}{8a_s} n_{1d}}, \tag{3.1}$$

in contrast to the three-dimension case where the ratio reduces with density; this points to the fact that the classical picture based on the mean field theory becomes inadequate for very dilute samples.

In such cylindrical geometry the order parameter can be written as $\Psi = \sqrt{n_{1d}} f(\rho_\perp)/a_\perp$ where $\rho_\perp = r_\perp/a_\perp$ is the dimensionless radial coordinate. The GP equation can be now recast in dimensionless form [54]

$$\left(-\frac{1}{2}\frac{\partial^2}{\partial\rho_\perp^2} - \frac{1}{2\rho_\perp}\frac{\partial}{\partial\rho_\perp} + \frac{1}{2}\rho_\perp^2 + 4\pi a_s n_{1d} f^2\right) f = \frac{\mu}{\hbar\omega_\perp} f, \tag{3.2}$$

where the normalization condition of the function f is $2\pi \int |f(\rho_\perp)|^2 \rho_\perp \mathrm{d}\rho_\perp = 1$.

The equation defines two important regions; the first is where $a_s n_{1d} \gg 1$, which is called the Thomas-Fermi region, i.e., Three-dimension cigar. In this region excitations happen in both the longitudinal and radial directions and the kinetic term in the GP equation can be neglected. The density will take the typical shape of inverted parabola and the normalized chemical potential will be

$$\frac{\mu}{\hbar\omega_\perp} = \sqrt{4 a_s n_{1d}}. \tag{3.3}$$

We can also define the Thomas Fermi radius (where the density vanishes) to be $R_\perp = 2a_\perp (a_s n_{1d})^{1/4}$.

The second case is where $a_s n_{1d} \ll 1$; we will call this case a one-dimensional mean field, here the first correction to the non-interacting value of the chemical potential is linear with density

$$\frac{\mu}{\hbar\omega_\perp} = 1 + 2 a_s n_{1d}. \tag{3.4}$$

We would consider the linear term as the chemical potential, while the constant term in the equation originating from the zero point motion in the radial direction can be emitted.

A good way to define the two regions is by looking at the ratio $N\frac{a_s a_\perp}{a_x^2}$, where the longitudinal oscillator length $a_x = \sqrt{\hbar/m\omega_x}$. The radial Thomas-Fermi limit is reached when $N\frac{a_s a_\perp}{a_x^2} \gg 1$, then the equilibrium linear density equation reads

$$n_{1d}(x) = \frac{1}{16a_s}\left(\frac{15Na_s a_\perp}{a_x^2}\right)^{4/5}\left(1-\frac{x^2}{X^2}\right)^2, \tag{3.5}$$

with $X = (a_x^2/a_\perp)\left(15Na_s a_\perp/a_x^2\right)^{1/5}$.

In the opposite case where the radial motion freezes the equilibrium, linear line density would be

$$n_{1d}(x) = \frac{1}{4a_s}\left(\frac{3Na_s a_\perp}{a_x^2}\right)^{2/3}\left(1-\frac{x^2}{X^2}\right)^2, \tag{3.6}$$

where $X = (a_x^2/a_\perp)\left(3Na_s a_\perp/a_x^2\right)^{1/3}$. The difference between the two density profiles reflects the divergence in behavior of the two regimes. But for both geometries, three-dimension cigar and one-dimension mean field, the radial frequency should be much larger than the longitudinal one, hence $\omega_\perp t \gg 1$ and $\omega_z t \ll 1$. This gives rise to the dynamics during time of flight where the longitudinal size would be frozen while the radial size would expand according to

$$R_\perp(t) = R_\perp \omega_\perp t. \tag{3.7}$$

The difference between the two regions can be found while looking at the ratio between the time-dependent radial and longitudinal expansion

$$\frac{R_\perp(t)}{X(t)} = \frac{R_\perp}{X}\omega_\perp t. \tag{3.8}$$

For Thomas Fermi gas, $R_\perp/X = \omega_z/\omega_\perp$; hence the ratio in expansion will mainly depend on the geometry and not atom number, where for the one-dimension mean field regime $R_\perp \sim a_\perp$ where $X \sim N^{1/3}$; hence there will be tight relation in this region between TOF expansion to the atom number [6].

3.1.2 Introduction to Coherence in mean-field

We defined mean-field to be as long as the ratio (3.1) is larger than unity and by evaluation (3.6) at $x = 0$. These two arguments give rise to two conditions

$$n_{1d}\frac{a_\perp^2}{a_s} \gg 1, \text{ and } N\frac{a_\perp^4}{a_s^2 a_x^2} = \frac{N}{\lambda}\left(\frac{a_\perp}{a_s}\right)^2 \gg 1, \tag{3.9}$$

where $\lambda = \left(\frac{a_x}{a_\perp}\right)^2 = \frac{\omega_\perp}{\omega_x}$ is the aspect ratio. For extremely low temperatures ($T \to 0$) the condensate is coherent and can be well described by an effective single-particle wave function occupied by a large number of atoms [73]. The coherence of phase in a condensate was shown by an imaging interference pattern of two independent condensates that were overlapping [74]. A BEC also has a uniform spatial phase that can be seen by interference techniques [75], hence the coherence length of a BEC is limited by the condensate length. Further experiments in a cigar-shape BEC showed the radial momentum distribution using Bragg spectroscopy techniques [76].

Although in extremely low temperatures the BEC has a uniform phase, it is not obvious at finite temperature. At finite temperature the condensate is 'fragmented' into independent condensates with random fluctuating relative phase. This process was often discussed in the context of nucleation of a condensate [53]. There, the equilibrium state of the system was assumed to be 'pure' condensate without phase fluctuations. However, before the condensate is completely formed, phase fluctuations between the different regions of the cloud are expected so even density fluctuations are suppressed.

But even at the equilibrium state at low dimensions quantum systems show great differences in their coherence properties from the $3d$ case with respect to statistical and phase-correlation properties [77]. In low dimension systems, phase fluctuations of the order parameter are expected to destroy the off-diagonal long-range order. This happens at temperatures that are well below the critical temperature, T_c, but above a certain characteristic temperature T_ϕ [78]. In the range $T_\phi < T < T_c$, the cloud is a "quasi-condensate" whose incomplete phase coherence is due to thermal excitations of the longitudinal (axial) mode with wavelength larger than its radial size. This phase coherence decay can be explained by the Mermin–Wagner–Hohenberg theorem [79, 80] suggests that for $d \leq 2$ true long-range order is destroyed by thermal fluctuations at any finite temperature and as a result T_ϕ should go to zero. Although so a "quasi-condensate" can be created below a certain finite critical temperature [81].

The behavior of quasi-1d condensates is still an open question, therefore a wide theoretical and experimental effort is done to understand these systems. In 2001 Dettmer et al. measured the conversion of phase fluctuations to ripples in the density profile during free expansion of the cloud (TOF measurement) [78, 82]. Later, using Bragg spectroscopy, Richard et al. measured the axial momentum distribution in an elongated cloud at the Thomas Fermi region, where the outcome of phase fluctuates in the condensate [83]. For the case of high anisotropic traps density fluctuations cannot be suppressed by the mean field interaction; this effect, which was measured by Esteve et. al. [71] and discussed by Schumm and Hofferberth et al. [29, 84], will be investigated later.

In the case of Thomas Fermi condensate, the cloud won't look fragmented in the trap; however after expansion, density ripples start to appear. These can be explained quantitatively as follows. While the condensate is in equilibrium the density

distribution remains largely unaffected even if the phase fluctuates [77]. The reason is that the mean-field inter-particle interaction prevents the transformation of local velocity fields provided by the phase fluctuations into modulations of the density. However, after switching off the trap, the mean-field interaction decreases, which gives rise to conversion of the axial velocity fields into density distribution [78].

For elongated BEC in the Thomas Fermi region the phase can be represented as follows [78]

$$\phi_j(x) = \left[\frac{(j+2)(2j+3)g_{3d}}{4\pi R_{TF}^2 L \epsilon_j (j+1)}\right]^{1/2} P_j^{(1,1)}\left(\frac{x}{L}\right)\frac{\left(\alpha_j + \alpha_j^*\right)}{2}, \tag{3.10}$$

where $\epsilon_j = \hbar\omega_x\sqrt{j(j+3)/4}$ is the spectrum of low energy axial excitation [85], $P_j^{(1,1)}$ are the Jacobi polynomials, $g_{3d} = \frac{4\pi\hbar^2 a_s}{m}$ is the coupling constant, and $R_{TF} = \sqrt{2\mu/m\omega_\perp^2}$, $\frac{1}{2}L = \sqrt{2\mu/m\omega_x^2}$ are the Thomas Fermi radius and length, respectively [82]. Where the quasi-particle creation and annihilation operators have been replaced by the complex amplitudes α_j and α_j^*, such that $\left\langle|\alpha_j|^2\right\rangle = 1/\left(\exp\left(\epsilon_j/k_BT\right)-1\right)$ is the occupation number of the quasi-particle in mode j. The formation of the stripes during TOF expansion for times, t, which are in the interval $\mu/\hbar\omega_x^2 \gg t \gg \mu/\hbar\omega_\perp^2$, are given by (see Fig. 3.1)

$$\frac{\delta n(x)}{n_0(x)} = 2\sum_j \sin\left[\frac{\epsilon_j^2 t}{\hbar\mu\left[1-\left(\frac{x}{L}\right)^2\right]}\right]. \tag{3.11}$$

Here $n_0(x)$ is the Thomas-Fermi density fit profile of an unperturbed cloud. The mean squared density fluctuation $\left(\frac{\sigma_{BEC}}{n_0}\right)^2$ is given by averaging $\left(\frac{\delta n(x)}{n_0(x)}\right)^2$ over many realizations, such that the central part of the cloud ($x = 0$) would give rise to

$$\left(\frac{\sigma_{BEC}}{n_0}\right)^2 = \frac{T}{\lambda T_\phi}\sqrt{\frac{\ln(\omega_\perp t)}{\pi}}\left(\sqrt{1+\sqrt{1+\left(\frac{\hbar\omega_\perp^2 t}{\mu\ln(\omega_\perp t)}\right)^2}}-\sqrt{2}\right), \tag{3.12}$$

where $k_BT_\phi = 15(\hbar\omega_x)^2 N_0/32\mu$ is the characteristic temperature, and N_0 is the averaged total atom number. The coherence length in such a region is $L_\phi = 2\hbar n_{1d}/(k_BTm)$ [77].

3.1.3 Beyond mean field

When the atomic line density becomes very small such that $n_{1d}\frac{a_\perp}{a_s} \leq 1$ and also $N\lambda\left(\frac{a_\perp}{a_s}\right)^2 \leq 1$ (3.9), the mean field GP equation fails and one should take into account beyond mean field effects. In 1963 Lieb and Liniger obtained an exact

solution to the many-body problem of $1d$ uniform BEC interacting with repulsive zero-range force [86]. The form of this equation while considering a $1d$ system of N interacting bosons in the absence of a trapping potential is

$$H_{1d}^{0} = -\frac{\hbar^2}{2m}\sum_{j=1}^{N}\frac{\partial^2}{\partial x_j^2} + g_{1d}\sum_{i=1}^{N}\sum_{j=i+1}^{N}\delta\left(x_i - x_j\right), \tag{3.13}$$

where the left term is the kinetic term and the right is the interaction term. $g_{1d} = \frac{2\hbar^2}{m}\frac{a_s}{a_\perp^2} = \frac{2\hbar^2}{ma_{1d}}$ where $a_{1d} = a_\perp^2/a_s$ is the relevant interaction length as long as $a_\perp \gg a_s > 0$. The Hamiltonian can be diagonalized exactly via a Bethe ansatz [86] such that for any positive coupling constant, g_{1d}, the energy per particle at zero temperature would be

$$\epsilon\left(n_{1d}\right) = \frac{\hbar^2}{2m}n_{1d}^2 e\left(\gamma\left(n_{1d}\right)\right), \tag{3.14}$$

The function $e\left(\gamma\right)$ is given by $e\left(\gamma\right) = \frac{\gamma^3}{\lambda^3(\gamma)}\int_{-1}^{+1} g\left(x,\gamma\right)x^2 dx$, where $g\left(x,\gamma\right) - \frac{1}{2\pi} = \int_{-1}^{+1}\frac{2\lambda(\gamma)}{\lambda^2(\gamma)+(x-y)^2}g\left(y,\gamma\right)dy$, and $\lambda\left(\gamma\right) = \gamma\int_{-1}^{+1} g\left(x,\gamma\right)dx$ [54].

γ is a dimensionless parameter that reflects interaction and is defined as the energy per particle $\epsilon_{int} = n_{1d}g_{1d}$, divided by the characteristic kinetic energy of two particles at a mean separation distance of $1/n_{1d}$ between them, $\epsilon_{kin} \approx \frac{\hbar^2 n_{1d}^2}{m}$ [54]. Therefore γ would be

$$\gamma = \frac{\epsilon_{int}}{\epsilon_{kin}} = 2/\left(n_{1d}a_{1d}\right). \tag{3.15}$$

The value of gamma gives rise to two very interesting regions

$$\gamma \ll 1, \quad \epsilon\left(n_{1d}\right) \to \frac{g_{1d}n_{1d}}{2}, \tag{3.16}$$

and

$$\gamma \gg 1, \quad \epsilon\left(n_{1d}\right) \to \frac{\pi^2\hbar^2}{6m}n_{1d}^2. \tag{3.17}$$

The first equation presents the high density limit, where $n_{1d}a_{1d} \gg 1$; this gives rise to a weak coupling constant, g_{1d}, and weak interaction. This result coincides with the condition of one-dimension Thomas Fermi gas, $n_{1d}a_\perp^2/a_s \gg 1$, but although so there won't be a true BEC in $1d$ due to low-energy excitation, which reduces the long-range phase coherence at $T = 0$.

The second case (3.17) is when the atomic line density is very low, then surprisingly the gas behaves as a chain of strongly interacting bosons. In this region, known as Tonks-Girardeau gas, the interaction is so strong, $g \gg 1$, that the atoms start to behave like fermions [87, 88].

3.1.4 Coherence beyond mean field

For low dimension systems the coherence length is limited due to low-energy excitations that perturbed the long range order. We will deal now with the case of

weak interactions where $\gamma \ll 1$, and mainly follow Petrov for this derivation [89]. The field operator is made of two terms, phonon modes ($\epsilon \ll \mu$) and free particles ($\epsilon \gg \mu$). To use the Bogolyubov approximation we first need to make sure that the temperature is low enough that it would be possible to omit fluctuations originating from high energy excitations ($\epsilon \gg \mu$). The total field operator that includes both density and phase is

$$\hat{\Psi} = \exp\left(i\hat{\phi}\right)\sqrt{\hat{n}},\ \hat{\Psi}^{\dagger} = \sqrt{\hat{n}}\exp\left(-i\hat{\phi}\right), \tag{3.18}$$

where the density and phase operators are real and satisfy the commutation relation

$$\left[\hat{n}\left(\mathrm{r}\right), \hat{\phi}\left(\mathbf{r}'\right)\right] = i\delta\left(\mathbf{r} - \mathbf{r}'\right). \tag{3.19}$$

Now we can use the Bogolyubov approximation to separate the density and phase in the field operator and simplify even more by writing the density as uniform and small fluctuations, and phase as phonon and particle-like excitations (which are omitted in $1d$)

$$\hat{n}\left(x\right) = n_0\left(x\right) + \delta\hat{n}, \tag{3.20}$$

$$\hat{\phi}\left(x\right) = \hat{\phi}_s\left(x\right). \tag{3.21}$$

Such that the new field operator will be

$$\hat{\Psi} = \sqrt{n_0}\exp\left(i\hat{\phi}_s\right). \tag{3.22}$$

In a uniform gas the signature of a BEC is the long-range order in the system; hence the one-particle density matrix would have a finite value, i.e., $\rho\left(\mathbf{r}, \mathbf{r}'\right) = \left\langle\hat{\Psi}\left(\mathbf{r}\right)\hat{\Psi}\left(\mathbf{r}'\right)\right\rangle$ remains finite at $|\mathbf{r} - \mathbf{r}'| \to \infty$. Using (3.22) the $1d$ density matrix would be [89]

$$\rho\left(x, x'\right) = n_0\left\langle e^{-i\left[\hat{\phi}_s(x) - \hat{\phi}_s(x')\right]}\right\rangle = n_0 e^{-\frac{1}{2}\left\langle\left[\hat{\phi}_s(x) - \hat{\phi}_s(x')\right]^2\right\rangle}. \tag{3.23}$$

So the phase correlator yields (see Fig. 3.1)

$$\left\langle\left[\hat{\phi}_s\left(x\right) - \hat{\phi}_s\left(0\right)\right]^2\right\rangle \approx \underbrace{\frac{k_B T}{\sqrt{\mu T_d}}\frac{x}{\xi_{1d}}}_{thermal} + \underbrace{\frac{1}{\pi}\sqrt{\frac{\mu}{T_d}}\ln\left(\frac{x}{\xi_{1d}}\right)}_{vacuum}, \tag{3.24}$$

where $T_d = \hbar^2 n_{1d}^2/m$ is the temperature of quantum degeneracy, and consequently $\xi_{1d} = \hbar/\sqrt{m n_{1d} g_{1d}}$ is the $1d$ healing length. In (3.24) the first term comes from the thermal part where the second comes from the vacuum part of the phase fluctuations.

This equation proves rigorously that there is no true BEC in $1d$, since if we take finite T the long-range order is destroyed by long-wave fluctuations of the phase leading to exponential decay of the density matrix, while at $T = 0$ there will be power-law decay due to quantum fluctuations. For very low temperatures the decay length can become large compared to the healing length; hence the system will be coherent for length given by the decay length. This situation was called quasi-condensate by Popov [90].

3.1.5 The $3d/1d$ cross-over regime

Atom chips allow the creation of tight confining potential, understanding the cross-over between a coherent $3d$ BEC to a $1d$ quasi-condensate is important for any experimental application. The cross-over region was investigated by Gerbier in 2004 [91]; it was found that the transition is very smooth. A nice example comes from the phase fluctuations at infinite temperature; in an elongated BEC phase fluctuations start to appear as the aspect ratio increases, but as long as the atomic line density is high the mean-field interaction is strong enough to prevent translation of phase gradients to density fluctuations. Once the trap becomes more isotropic and the atomic line density decreases the mean field weakens and density fluctuations start to appear; this shows a smooth transition (see Fig. 3.1).

Gerbier in his calculation used a local density approximation (LDA) to describe the cross-over regime and to smoothly connect the $3d$ and $1d$ regimes, in which $\mu \gg \hbar\omega_\perp$ and $\mu \ll \hbar\omega_\perp$, respectively.

He introduced the parameter $\alpha = 2\left(\mu/\hbar\omega_\perp - 1\right)$, knowing that the local equilibrium chemical potential has a dependence on x through

$$\mu_{l.e.}\left[n\left(x\right)\right] + V\left(x\right) = \mu, \tag{3.25}$$

where μ is the global chemical potential of the cloud in the trap, $V\left(x\right) = \frac{1}{2}m\omega_x^2 x^2$ is the longitudinal harmonic potential, and $\mu_{l.e.}\left[n\right] = \hbar\omega_\perp\sqrt{1 + 4a_s n\left(x\right)}$. Hence for $x = L$ (i.e. $n\left(L\right) = 0$) 3.25 would be $\hbar\omega_\perp + \frac{1}{2}m\omega_x^2 L^2 = \mu$ and would be given by

$$L = \frac{a_x^2}{a_\perp}\sqrt{\alpha}. \tag{3.26}$$

The parameter that gives the ratio of interaction energy to the radial zero point energy is [92]

$$\chi = N a_s a_\perp / a_x^2. \tag{3.27}$$

Using this parameter in the solution of the integral $\int_{-L}^{L} n\left(x\right) dx = N$, one can define a closed equation for the static properties of the condensate at any confining strength [91]

$$\alpha^3\left(\alpha + 5\right)^2 = \left(15\chi\right)^2. \tag{3.28}$$

At $\chi \gg 5$ the mean-field interaction dominates the transverse confinement, which fits the $3d$ Thomas-Fermi cloud, $\alpha \approx \alpha_{3d} = \left(15\chi\right)^{2/5}$, where for $\chi \ll 5$ the transverse motion is strongly confined and $\alpha \approx \alpha_{1d} = \left(3\chi\right)^{2/3}$. The tangent point of the two parameters ($\alpha_{3d} = \alpha_{1d}$) gives the crossover value where $\chi_{cross} \approx 3.73$.

3.2 Experimental realization of $1d$ system

In this section we explore the transition between $3d$ BEC to a $1d$ quasi-BEC. We look at the effect of phase fluctuations and explore the difference between mixed $3d/1d$ where density fluctuations are suppressed by the mean field energy to where the density is too low to suppress such density fluctuations.

3.2.1 Realizing $1d$ experimentally

Experimentally, $1d$ quasi-BEC state can be reached by using highly anisotropic traps such as strongly confined optical traps [93] or highly anisotropic harmonic magnetic traps, as achieved by atom chips [26]. In such harmonic traps the longitudinal trapping frequency, ω_x, is much lower than the transverse one ($\omega_\perp = \omega_y = \omega_z$), so that $\omega_x \ll \omega_\perp$. Add to that in cases where the chemical potential and temperature are smaller than the transverse single particle ground-state wave function energy, μ, $T \leq \hbar\omega_\perp$, the radial motion will be 'frozen'. This inequality leads to an interesting limit that connects the atomic line density and dimensionality.

Equation (3.4) $\left(n_{1d} \approx \frac{\mu}{2a_s\hbar\omega_\perp}\right)$ relates the line density to the chemical potential and trapping frequency, substitution of the inequality $\mu \leq \hbar\omega_\perp$ gives

$$n_{1d} \leq \frac{1}{2a_s} \approx 90\, atoms/\mu\text{m}. \tag{3.29}$$

The absence of vorticity, which is one of the main characteristics of $1d$ Condensate, also poses an interesting limit. The radius of a vortex is the healing length, a connection between this radius to the wave function radial extension and the healing length can be found. The healing length is given by $\xi = \sqrt{\frac{a_\perp^2}{8a_s n_{1d}}}$, now replacing the one-dimensional density with its limiting value $\left(n_{1d} \leq \frac{1}{2a_s}\right)$ gives a limiting value for the wave function extension

$$a_\perp \leq 2\xi. \tag{3.30}$$

Although it is mathematically identical to (3.29) this is a very interesting result since it links the absence of vortices in the $1d$ case to the actual ratio between the vortex radius and the condensate radial size.

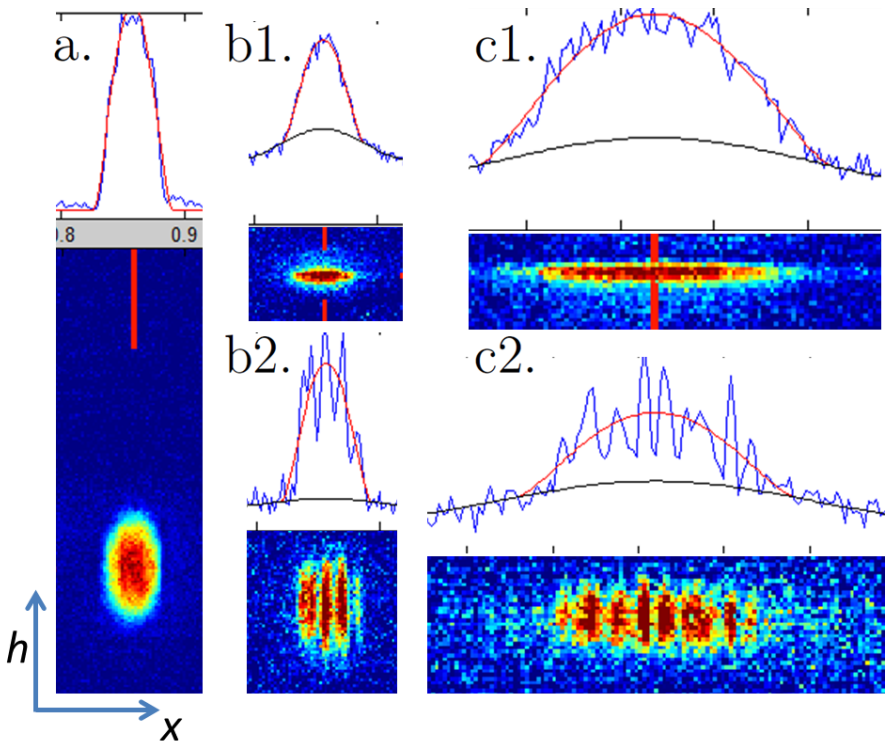

Figure 3.1: A density profile picture of a BEC in different regions, above each image the longitudinal line density profile is shown. a. A TOF image of a coherent 3d BEC. One can see that the line density profile is not perturbed since the phase is coherent (at any reasonable TOF). b1. An in situ image of a BEC in the mean field regime ($\lambda \approx 24.5$); at this stage there are almost no density gradients since the mean field energy is strong enough to forbid translation of phase gradients into density gradients. b2. A TOF image after 7 ms originated from a similar trap as the later image. Here one can see that the phase gradients have translated to the density profile as explained in sec. 3.1.2. c1. An in situ image of a quasi-BEC in extremely tight trap ($\lambda \approx 132$). Here the density profile is perturbed since beyond mean field effects accrue and the long-range order is destroyed. c2. A TOF image after 7 ms originating from a similar trap as the later image. Here one can see a combination of phase and density gradients that translate to the density profile.

3.2.2 The experimental system

The following experiments were done as part of a joint project with Ron Folman's Atom Chip Lab in Ben-Gurion University on their BEC2 setup in collaboration with Simon Machlof (BGU) and Anton Picardo-Selg (Nottingham). We thank Ron and Shimi for the opportunity to use their labs and share their knowledge.

As part of this joint project we loaded the BGU2 atom chip setup from the under structure to a chip wire for the first time (see Fig. 3.2).

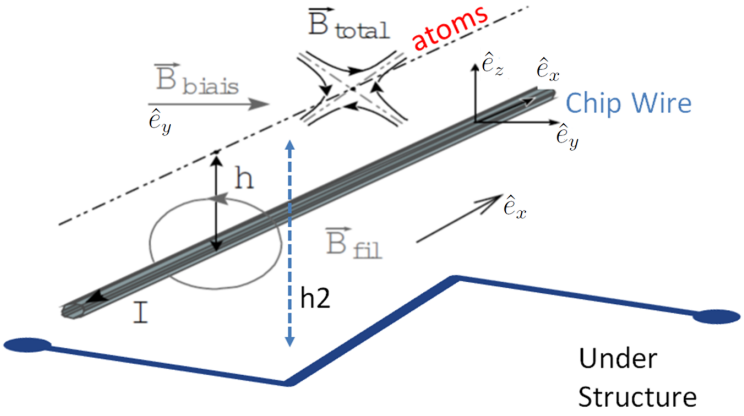

Figure 3.2: Sketch of the BGU2 setup. In blue is the under structure IP Z trap sitting at a distance $h_2 = 1.2\,\text{mm}$ from the atoms. The chip wire is a 4 mm long, $w = 200\,\mu\text{m}$ wide structure at a distance of about $h = 100\,\mu\text{m}$ from the atoms. The longitudinal ($\hat{e}_x$) confinement is done using the under structure IP trap where the transverse ($\hat{e}_y - \hat{e}_z$ plane) confinement is a combination of the chip wire and IP trap. Due to the large differences in distance from the atoms in the two traps, the radial confinement can be dominated by the chip wire if needed.

The experimental procedure was as follows: First, using the under structure Z Ioffe-Pritchard trap we magnetically trapped and RF cooled an atomic cloud of ^{87}Rb atoms in their $|F = 2, m_F = 2\rangle$ state. We could cool down the atoms to a 3d BEC of about 12 K atoms or load them to a 200 μm width and 4 mm long chip wire (see Fig. 3.3). In the case of chip loading we slowly increased the current in the chip wire and trapped the atoms by both the atom chip and under structure. Then we applied final evaporation reaching $3d/1d$ BEC of about 4.2×10^3 atoms or a quasi-BEC of about $2,000$ ^{87}Rb atoms at their $|F = 2,\ m_F = 2\rangle$ state. The longitudinal confinement was done solely by the under structure Z wire, while the transverse (radial) confinement is a joint product of both the chip wire and the under structure trap. The current ratio between the chip wire and the under structure Z wire sets the radial trapping frequency and hence the BEC regime. We gave names to the different traps: the *Copper trap* confines a 3d BEC just with the under structure IP trap, the *mid-trap* is at the cross-over region between 3d to 1d, and the *final trap* holds a 1d quasi-BEC. The trapping frequencies, aspect ratios, and atom numbers of the traps are as shown in Tab. 3.1. Where the transverse trapping frequencies were measured by applying a small magnetic kick to the cloud and the longitudinal trapping frequencies were calculated theoretically.

Trap	$\omega_\perp$	ω_L	$\bar{N}$	L_x	λ
Copper	$2\pi \cdot 600\,\mathrm{Hz}$	$2\pi \cdot (60)$ Hz	$12\,k$	$60\,\mu$m	11
Mid	$2\pi \cdot 1125\,\mathrm{Hz}$	$2\pi \cdot (46)$ Hz	$4.2\,k$	$50\,\mu$m	24.5
Final	$2\pi \cdot 1190\,\mathrm{Hz}$	$2\pi \cdot (9)$ Hz	$4.5\,k$	$300\,\mu$m	132

Table 3.1: Measured (theoretical) trapping frequencies and atom numbers for the three magnetic traps. L_x represents the typical full longitudinal length and $\lambda = \frac{\omega_\perp}{\omega_x}$ is the aspect ratio.

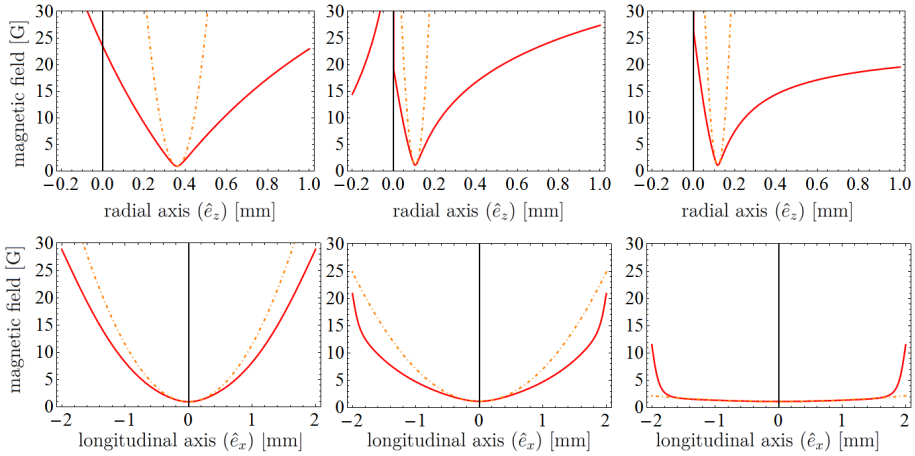

Figure 3.3: A simulation of the magnetic field at the three traps. The point $z = 0$ represents the chip where $x = 0$ is the center of the under structure IP z trap. In red is the total magnetic field and in orange is the harmonic approximation. Left: a cooper trap. Centre: the mid trap, here the combination between the chip and under structure magnetic field reduce the harmonicity of the trap. Right: the final trap, one can see that in the longitudinal direction more of a box kind of a potential appears.

3.2.3 The cooling process

The cooling to BEC is done using RF evaporative cooling which is well explained in the literature[28, 66] and sec. 1.2.1. In Fig. 3.4 one can see a series of TOF images of the cooling process. The initial cloud was trapped in the *mid trap* and the images were taken at a fixed TOF for different 'RF knife' frequencies. The cooling process is governed by the formalism given in sec. 1.2.1. It is nice to see the appearance of perturbations in the longitudinal line density; the origin of these perturbations are phase gradients in the trapped cloud, which after TOF translate to the density profile as explained in sec. sec. 3.1.2.

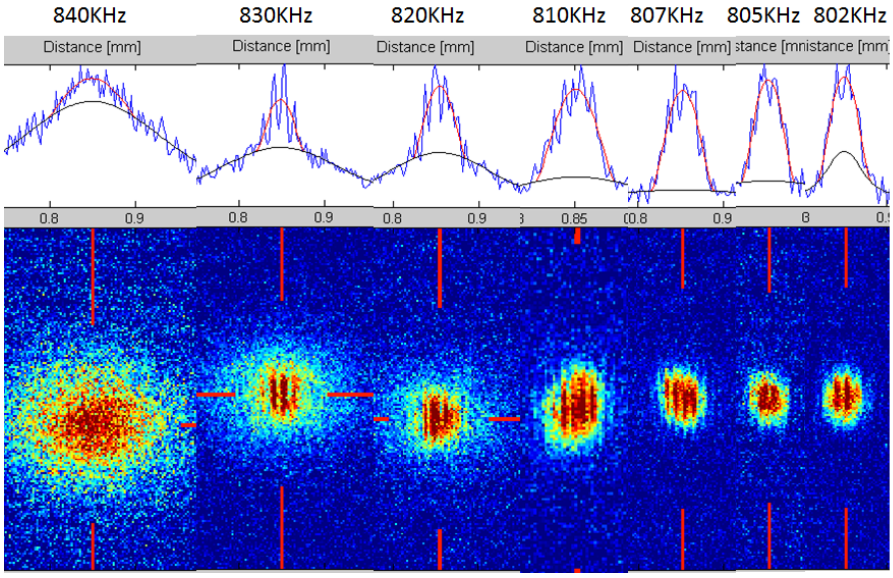

Figure 3.4: A TOF image of an evaporation process starting at a thermal cloud and finishing at a BEC. The temperature decrease is governed by the formula $h\nu_{RF} = \eta k_B T$, where η is given in sec. 1.4. At the top plot the density profile is shown. The thermal part has Gaussian profile where the condensate has a TF profile. This BEC was created in the *mid trap* with aspect ratio $\lambda = 24.5$ it is nice to see the appearance of perturbation in the longitudinal density profile due to the finite thermal length. These perturbations are due to phase gradients in the trapped cloud which translate during TOF to the density profile.

3.2.4 The effect of TOF

Anisotropic $3d/1d$ BEC phase fluctuations in the order parameter destroy the off-diagonal Long-range order, although so at this atomic density the mean field energy is enough to prevent strong perturbations in the density profile of the trapped cloud. In Fig. 3.5 the translation of phase fluctuations into the density profile is shown as function of TOF [78]. BEC originating from the *mid trap* has about 4.2×10^3 atoms and a typical length of $50\,\mu$m. Therefore at the value $\chi = Na_s a_\perp / a_x^2 \approx 1.45$ we passed the cross-over point from $3d$ to $1d$ ($\chi_{cross} \approx 3.73$), but due to the high $1d$ line density we are in the mean field region where the TF approximation is at its limit; hence the radial movement is not fully frozen (see sec. 3.1.1).

Experimental procedure

In this experiment we checked the translation of phase fluctuations to the density profile as a function of TOF. First we cooled the atoms to a BEC in the *mid trap*, then we took a few tens of images for each TOF. From each image we extracted two line vectors; one is the actual density profile, $n(x)$, and the other is the Thomas-Fermi fit

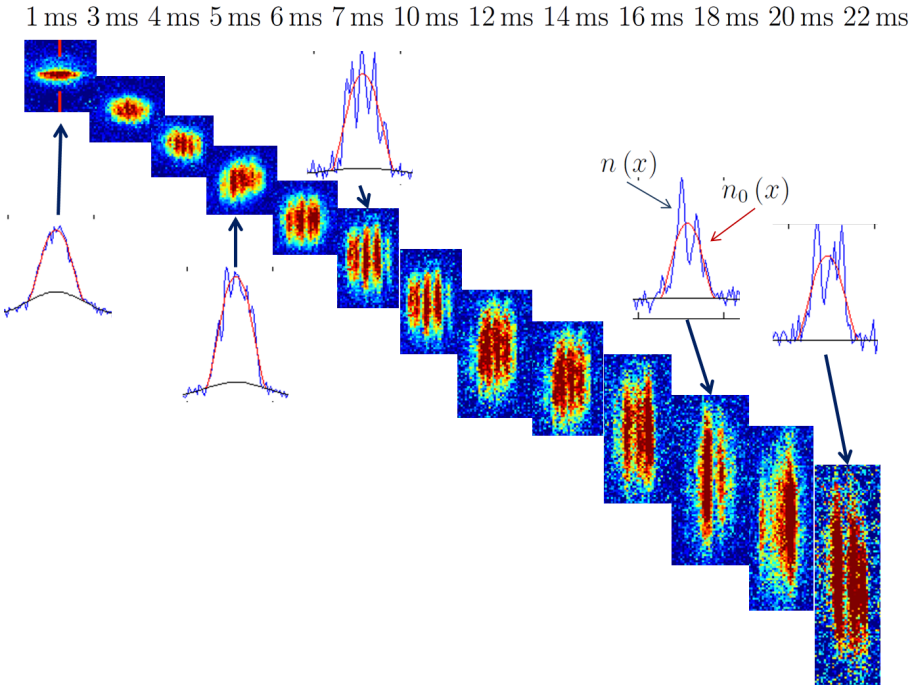

Figure 3.5: TOF images of BEC generated in the *mid trap*. On top the TOF of each image is listed where the longitudinal line density is sporadically shown. In these images the translation of phase fluctuations into density fluctuations during TOF for a BEC in the mean field region is visible [78].

profile, $n_0\,(x)$. These line vectors cross the cloud in its longitudinal direction where each point is binning of few radial pixels. Since the trap is highly anisotropic during time of flight the longitudinal size is almost frozen while the radial size expands rapidly, therefore averaging over $n\,(y)$ gives us greater accuracy in calculation. In Fig. 3.6 and Fig. 3.7 one can see the outcome of these line vectors.

Using the formalism given in sec. 3.1.2, we first calculate the chemical potential by using $\mu = \frac{1}{8}L_x^2 m\omega_x^2 \approx 1\times10^{-30}\,\mathrm{J} = 2\pi\cdot 1.4\,k\mathrm{Hz}$ [82], from which we get the following Thomas-Fermi radius: $R_{TF} = \sqrt{2\mu/m\omega_\perp^2} = 510\,n\mathrm{m}$. The shape of the zero-temperature condensate is $n_{1d}\,(\rho,x) = n_{1d}\,(0)\,(1-\rho^2/R_{TF}^2 - x^2/(L_x/2)^2)$, where using $N = \int n_{1d}\,(\rho,x)$ gives the central 1d line density $n_{1d}\,(0) = \frac{3N}{2L_x} = 125\,atoms/\mu\mathrm{m}$. Another key feature is the characteristic temperature $T_\phi = 15\,(\hbar\omega_x)^2\,N/32\mu k_B = 35\,n\mathrm{K}$ [82].

The phase profile given in the theory section (3.11) holds for time of flight between $\mu/\hbar\omega_x^2 \gg t \gg \mu/\hbar\omega_\perp^2$, hence for $430\,ms \gg t \gg 200\,\mu\mathrm{s}$. Averaging the central part of this profile over many realizations gives the mean squared density fluctuations $\left(\frac{\sigma_{BEC}}{n_0}\right)^2 = \frac{T}{\lambda T_\phi}\sqrt{\frac{\ln(\omega_\perp t)}{\pi}}\left(\sqrt{1+\sqrt{1+\left(\frac{\hbar\omega_\perp^2 t}{\mu\ln(\omega_\perp t)}\right)^2}} - \sqrt{2}\right)$. The fit function in Fig. 3.7 gives the ratio $T/T_\phi = 0.13$; hence $T = 4.6\,n\mathrm{K}$. The latter value is very low

and seems to differ from our experimental conditions; the reason that the standard deviation equation doesn't hold might be the low 1d line density.

Having such low line density and low chemical potential ($\mu = 1.2\hbar\omega_\perp$) can indicate that we are at the low density limit of the Thomas Fermi mean field region. As a result, from the following we cannot use this type of calculation on BECs from the *final trap* since their line density and chemical potential are even lower. In the next chapter we introduce a different technique to measure the coherence and chemical potential of more isotropic BECs where density ripples already appear in the trapped cloud.

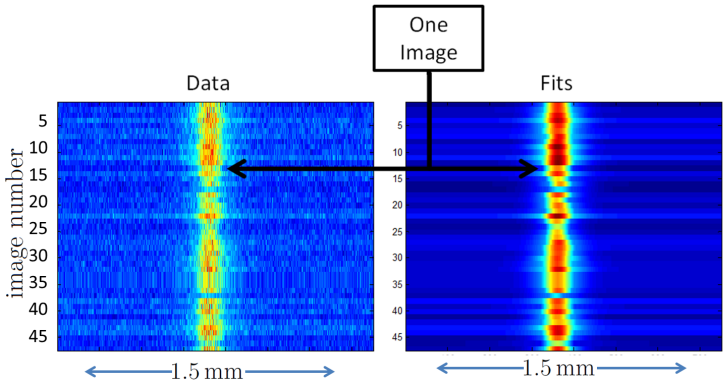

Figure 3.6: The data analysis procedure; the horizontal axis is the pixel number where the vertical axis is the image number. From each image two atomic density line vectors were extracted, one for the real density profile and one for the Thomas-Fermi fit profile. The horizontal direction is along the longitudinal direction of the cloud, where each point is a bin of a few pixels in the cloud's radial direction.

Measuring density fluctuations

Measuring fluctuations in the density distribution by means of absorption imaging [71] is a powerful tool to measure the quantum nature of an atomic sample. Using this technique effects in the scale of the de Broglie wavelength such as atomic bunching can be seen in the difference to other methods that incorporate integration of one of the condensate axes [94, 95]. Quasi-1d gas, i.e., gas in a tight anisotropic confining potential with temperature below critical temperature, T_c, allows integration over the radial axis. In this section we measured the translation of phase fluctuations to density profile during time of flight. The proposed method usually used to measure during in situ images can be utilized here as a useful tool. A full explanation about technical aspects of this type of measurement is given in sec. 4.2. In Fig. 3.8 the atom number variance as a function of mean atom number per pixel for three different times of flight is shown. We can treat the 1 ms time of flight image as an in situ image since in such a short time only very high moment components can translate to the density profile. Hence in this TOF the variance in density is mainly

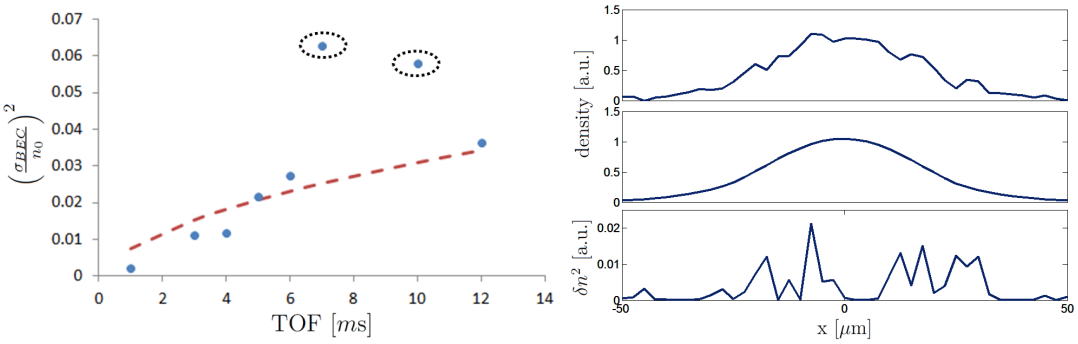

Figure 3.7: Right: Typical density profile of BEC after 3 ms TOF for trap aspect ratio of $\lambda = 24.5$. The top plot is the density profile $n(x)$, the middle is the corresponding fit, $n_0(x)$, and the bottom is their difference squared, $\delta n(x)^2 = (n(x) - n_0(x))^2$. Left: The measured standard deviation, $\left(\frac{\sigma_{BEC}}{n_0}\right)^2$, as a function of time of flight. The dashed line represents the fit function with $T/T_\phi = 0.13$. The two circulated points were not taken into consideration while fitting since the cloud temperature was significantly different.

due to density ripples in the in situ profile. The non-linear increase in the variance (see inset) can show a bosonic bunching behavior that is common for 1d Bose gas. For a 1d cloud in the mean field region we can take the maximal value of density as the center of the cloud; hence we can substitute the maximal variance per TOF in (3.12) to find the cloud temperature. Since we found that the approximation does not hold for our data we cannot use it. A theoretical analysis for the fluctuations in the density distribution as a function of atomic density during time of flight can be done in order to investigate the role of phase fluctuations in reduction of the long-range order in such highly anisotropic Bose-Einstein condensations.

3.3 Summary

In this chapter we have reviewed the theory behind 1d quasi-condensates from both the Bogoliubov framework and the complimentary Luttinger liquid approach. We have shown the experimental path between 3d and 1d elongated condensates and the spacial footprints that complements low dimensionality as a function of both temperature (sec. 3.2.3), and time of flight (sec. 3.2.4). Later we investigated the effect of time of flight on the density profile using two approaches; the first used the standard deviation in atom number at the peak density as a function of TOF (see Fig. 3.7). The second type of measurement was used to find the variance in atom number as a function of the mean atom number per pixel for different TOF (see Fig. 3.8). The latter is a unique way that has usually been used for in situ images [71]; we adapted it to our needs.

In Fig. 3.8 the transition of phase fluctuation to density ripples is highly visible where

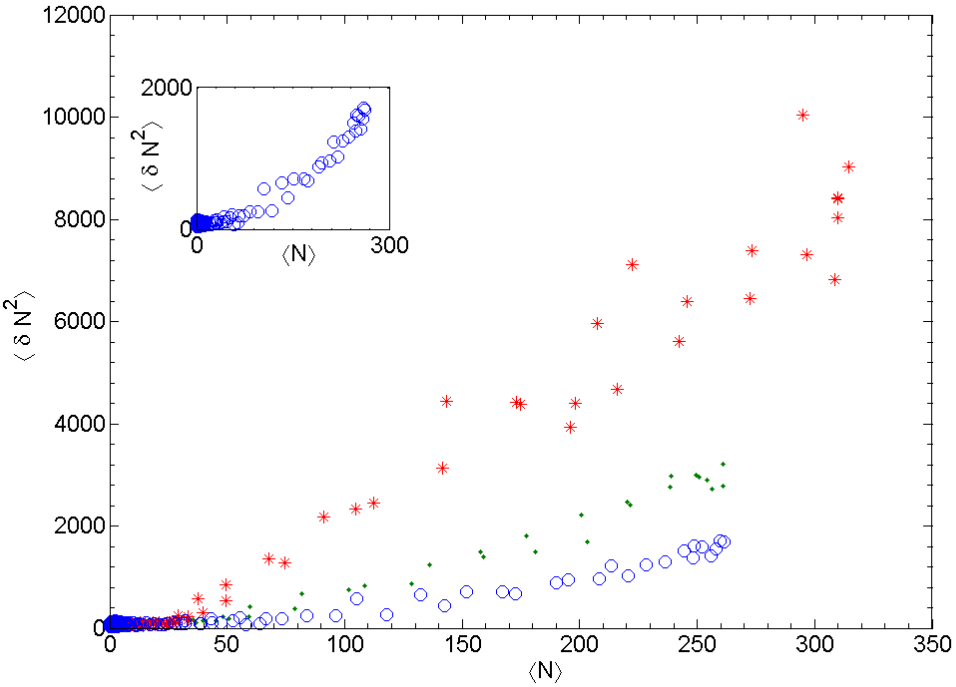

Figure 3.8: Atom number variance as a function of mean atom number per pixel. The variance is defined as $\delta N_i^2(x) = \left[N_i(x) - \alpha_i \bar{N}(x)\right]^2$, see sec. 4.2.1. Open circle corresponds to 1 ms time of flight for which fluctuations are given by the trapped cloud density profile. Dots and stars present 3 ms and 18 ms time of flight, respectively. The increase in the variance as a function of TOF is due to translation of phase fluctuations to the density profile. The inset shows the 1 ms time of flight at different scalings.

the variance for each of the mean densities increases as the flight time increases. A further theoretical analysis can be done on this interesting measurement that directly shows the translation of phase gradients to the density profile for cigar-shaped Thomas-Fermi condensates. The theory and measurements can also go beyond to tighten anisotropic geometries where the mean field energy is low enough that density ripples already appear in the trapped condensate. There the density ripples in the time of flight images will be a combination of phase and density gradients.

4 Density fluctuations in a quasi-1d BEC

In this chapter we explore the quantum behavior of a bosonic sample in an extremely anisotropic trap. We utilize different quantum features such as the variance in mean atom number as a function of temperature and density to learn about the interaction strength and bunching effect. To do so we investigate different imaging techniques, review the literature, and present experimental results.

4.1 Experimental parameters

In a classical gas the amount of fluctuation in atom number inside a small volume will be the square root of the atom number in that volume. We call these fluctuations "shot noise". Photons, on the other hand, are different since "photon bunching" as seen by Hanbury Brown, and Twiss [96, 97] is part of their quantum nature and can increase the fluctuations. Non-condensed Bose gas also has bunching behavior, which increases the fluctuations above shot noise level. In 2005 Fölling et al. observed spatial correlations in a Mott insulator phase of a rubidium Bose gas as it is released from an optical lattice trap [95], where Öttl et al. measured the $g^{(2)}(\tau)$ correlation function of an "atom laser" originated from a weakly interacting Bose Einstein condensate of ^{87}Rb atoms [98] both can be interpreted in terms of HBT effect.

Density fluctuations can be measured by means of absorption imaging; in such a method we integrate one of the clouds axis while imaging. Such integration masks the bunching effect since their correlation length is in the order of the de Broglie wavelength. But in highly isotropic traps for gas at or below zero point energy such integration is not needed. In addition, condensation reduces the bunching effect but $1d$ Bose gas doesn't condense and therefore bunching effects are enhanced. It was seen that once the $1d$ line density is smaller than a critical point $n_T = \left[m\left(k_B T\right)^2/\hbar^2 g_{1d}\right]^{1/3}$ density fluctuations are suppressed by a factor of $\left(n/n_T\right)^{3/2}$ [71].

In our experiment we produced a highly anisotropic trap with an aspect ratio of $\lambda \approx 132$; in such a trap bunching behavior won't appear in a thermal atomic sample $\left(k_B T \approx 10\hbar\omega_\perp\right)$. But as temperature reduces to the order of the radial trapping

energy there is an excess in the atom number variance compared to shot noise; this excess is due to the bosonic nature of the atoms. Using means of local density approximation the atom number fluctuations in the cloud's longitudinal direction are [99, 71]

$$\langle n(x)\, n(x')\rangle - \langle n(x)\rangle^2 = \underbrace{\langle n(x)\rangle\, \delta(x-x')}_{shot\ noise} + \underbrace{\frac{1}{\lambda_{dB}^2}\sum_{i=1}^{\infty}\sum_{j=1}^{\infty}\frac{e^{\beta\mu(i+j)}}{\sqrt{ij}}\frac{e^{-\pi(x-x')^2(\frac{1}{i}+\frac{1}{j})/\lambda_{dB}^2}}{\left[1-e^{-\beta\hbar\omega_\perp(i+j)}\right]^2}}_{bunching} \tag{4.1}$$

where $\beta = 1/(k_B T)$ and $\langle\cdots\rangle$ denotes an average. The first term on the right side of the equation is due to shot noise, and the second to bunching. For the case of a non-degenerate gas ($n_{1d}\lambda_{dB} \ll 1$) we can replace the Bose-Einstein occupation numbers by their Maxwell-Boltzmann approximation so only the term $i = j = 1$ remains and the bunching term reduces to $\langle n(z)\rangle^2 \exp(-2\pi(z-z')^2/\lambda_{dB}^2)\tanh^2(\beta\hbar\omega_\perp/2)$. The exponent donates the Gaussian decay of correlation where the tanh is due to the integration over the transverse states [71]. In our experiment we have limited resolution and therefore we should integrate the latter over the pixel size, Δ, which gives rise to

$$\langle N^2\rangle - \langle N\rangle^2 = \langle N\rangle + \langle N\rangle^2 \frac{\lambda_{dB}}{\sqrt{2}\Delta}\tanh^2(\beta\hbar\omega_\perp/2). \tag{4.2}$$

The integration on the exponent raises the prefactor $\frac{\lambda_{dB}\mathrm{Erf}\left[\frac{\sqrt{2\pi}\Delta}{\lambda_{\mathrm{dB}}}\right]}{\sqrt{2}} \approx \frac{\lambda_{dB}}{\sqrt{2}\Delta}$ for any $\Delta \geq \lambda_{dB}$. The ratio is the inverse of the number of elementary phase space cells occupied by N atoms. In our experiment $n_{1d}(0)\,\lambda_{dB} \gg 1$; therefore we cannot use the Maxwell-Boltzmann approximation and higher i, j terms in (4.2) need to be taken into account.

4.1.1 Chemical potential

The chemical potential of a quasi-condensate can be calculated by the thermodynamic approach, which gives the approximate value

$$\mu(n) = \hbar\omega_\perp\sqrt{1+4a_s n}, \tag{4.3}$$

where $n = N/\Delta$ is the pixel atomic density. Taking into account that the density follows thermal trapped Bose gas, using means of so-called local density approximation the chemical potential reads $\mu(x) = \mu_0 - m\omega_L^2 x^2/2$ [100].

4.1.2 Temperature

The temperature of a $1d$ quasi condensate is hard to find with usual means. During time of flight the transverse direction expands quickly as a function of the trap

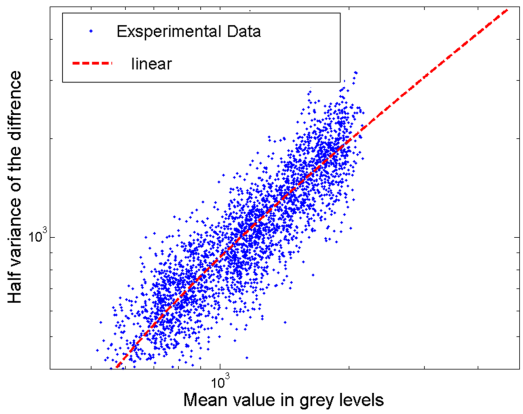

Figure 4.1: Noise measurement with pulsed laser beam. Half the variance of the difference vs. mean value in gray levels. The axes are in log-log scale and the fit line is linear. The fit function gives the conversion coefficient from gray levels to photo-electrons number.

confining potential, while the longitudinal direction changes its size very slowly due to the low temperature. A good way to measure the approximate temperature is by fitting the wings of the longitudinal in situ profile to an ideal Bose gas profile, or in warmer clouds to use Boltzmann fit function for the thermal part. In the following experiment the cloud was quite warm and the normal Popov method [101] wouldn't fit well so we used Boltzmann fit function for the thermal part, which gave temperature of $k_B T = (3-4) \times \hbar\omega_\perp$ (for the cold cloud in Fig. 4.5).

4.1.3 Camera calibration

In chapter 2 sec. 2.4 we have shown how to convert from gray-index to photons and how to find the conversion between photo-electrons to gray index. In the BGU setup the conversion between photons to gray index was done previously. In Fig. 4.1 we checked the linearity of the camera using the same means explained in sec. 2.4. The Image Source DMK 21BU04 we use in Nottingham and the Prosilica GC2450 used in BGU show linear behavior with increase in light intensity as they should.

4.1.4 Cloud height

The height of the cloud can be easily measured by means of Grazing Incidence Imaging. As explained in chapter 2. Once the atomic cloud is in close proximity to the chip a reflection is seen. We can find the exact z position of the cloud and its reflection by using dual fit function [65]. The distance between the center of the two clouds shows the height from the chip by $h = \frac{d}{2\cos\theta}$, where d is the distance and $\theta = 1.5°$ (see Fig. 4.2).

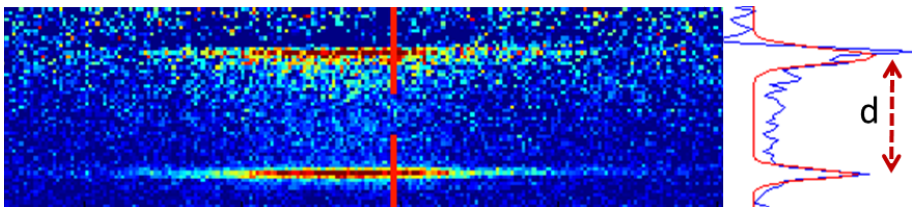

Figure 4.2: Measuring the distance, h, between the chip and the atomic cloud using Grazing Incidence Imaging technique $\left(h = \frac{d}{2\cos\theta}\right)$.

4.1.5 Trap frequency

The trapping frequency is easily measured by the standard technique. We give a little magnetic kick to the cloud in the z direction and release it after different hold times. We measured the cloud position as a function of trap hold time using A fixed time of flight. The frequency of the oscillations in position represent the trapping frequency (see Fig. 4.3).

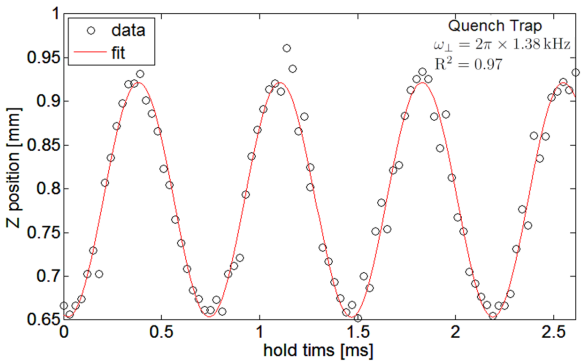

Figure 4.3: Vertical position of the cloud vs. trap hold time after a magnetic kick. The position was measured at fixed times of flight and the oscillation frequency gives the trapping frequency.

4.2 In situ Density Fluctuations

In this section we explain the experimental procedure we used to measure density fluctuations of the trapped condensate.

4.2.1 Finding the variance

Density fluctuations need to be measured while the cloud is trapped or after a very short release time. The measurements are conducted in a highly anisotropic

magnetic trap created by a combination of atom chips and an IP copper trap, as explained in sec. 3.2.2. Using evaporative cooling we obtained cold samples at a temperature of about $(3-4)\times\hbar\omega_{\perp}/k_B$ with an atom number of 4.5×10^3. In situ absorption images were taken with pulse duration of $100\,\mu$s and intensity of one-tenth of the saturation intensity. The effective camera pixel size is $2.3\times2.3\,\mu\mathrm{m}^2$ in the object plane. The camera was calibrated as explained in chapter 2 to match its gray-index to the real photon number.

The photon number in the absorption and flat-field images were called $N_{1,2}^{ph}(x,z)$, respectively. The atom number was given by the absorption per pixel $\left(\ln\left(N_2^{ph}/N_1^{ph}\right)\right)$ and was summed over the radial direction z

$$N(x)=\sum_z \ln\left[N_2^{ph}(x,z)/N_1^{ph}(x,z)\right]\Delta^2/\sigma_e, \tag{4.4}$$

where σ_e is the effective cross-section. Since the sample is optically thick and smaller than pixel height, the light that reaches the CCD is mostly light that bypassed the cloud. Therefore the measurement is not accurate in atom number. There are two techniques to overcome this problem; the first is to shine a long duration imaging pulse so the cloud expands due to thermal heating [71], the second is to release the cloud and let it expand in the radial direction for a few fractions of a ms. We chose the latter while releasing the cloud for $700\,\mu$s before taking the image; in this short time there is almost no change in the longitudinal density profile where the transverse expands as a function of trapping frequency. In addition to that, we corrected the atom number using the effective cross-section, σ_e, by comparing the averaged atom number in in situ and TOF images.

To measure the density fluctuations we followed Esteve et al. [71]; first we took a few hundreds of images (typically 300) at the same experimental conditions. To avoid long-term drifts from time to time we took a series of TOF images and aligned the system to overcome long term drifts of the trap bottom. Measurements were taken only when the system was very stable and only minor changes were needed, if any. To extract the variance we formed the quantity

$$\delta N(x)^2=\left[N(x)-\alpha\bar{N}(x)\right]^2, \tag{4.5}$$

where $\bar{N}$ is the mean atom number per pixel and $\alpha=\sum_x\frac{N(x)}{\bar{N}(x)}$ is a normalization factor. Since we are only interested in the atomic fluctuations, for each variance we reduced the photon shot noise by subtracting $\sum_z\left[1/N_1^{ph}+1/N_2^{ph}\right](\Delta^2/\sigma_e)^2$. We could use the presented approximate quantity for the light shot noise and atom number since imaging light intensity was much below saturation level. Later we have rearranged the data so the x axis would be the mean atom number and the y axis was set to be the mean variance (see Fig. 4.4).

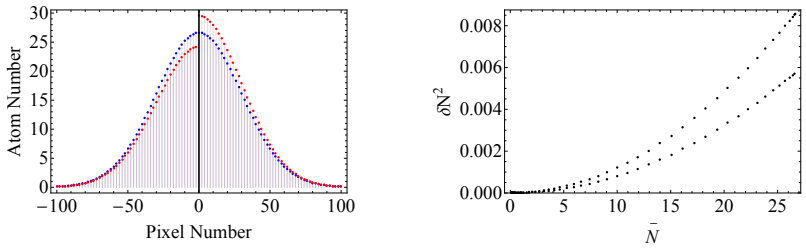

Figure 4.4: Setting the atom number variance as a function of the mean atom number per pixel. Left: Atom number as a function of pixel number. The blue dots represent the mean atom number $\bar{N}(x)$ and the red dots represent a single shot $\left(\bar{N}(x)+\delta N(x)\right)$. Right: Atom number variance as a function of the mean atom number. The x axis is $\bar{N}(x)$ (the values of the blue Gaussian), where the y axis is the variance $\delta N^2\left(\bar{N}\right)$. Each $\bar{N}$ value has two distinct variances (see the the red dots in the left figure) therefore there are two black lines one for the left side of the Gaussian and one for the right.

4.2.2 Thermal fluctuations

The density profile of a "hot" atomic sample behaves as an ideal Bose gas where bunching gives negligible contribution to $\langle\delta N^2\rangle$ (see 4.1). In a "hot" sample the atomic shot-noise fluctuations are observable and the variance increases linearly with mean atom number. In Fig. 4.5 two data sets shown, the thermal data ($k_BT \simeq 10\times\hbar\omega_\perp$) is linearly fitted where the slope $k = 0.19$ and not 1 as expected. The reason is quite obvious. When the pixel size is not bigger than the resolution of the imaging system, each atom can spread over a few pixels; this spread causes a reeducation of the slope. When the pixel size is small enough and the optical thickness is low the slope can be simply approximated by $k \simeq \Delta/\left(2\sqrt{\pi}\delta\right)$, where δ is the RMS width of the optical response, which is supposed to be Gaussian [71]. From the fit function we deduced $\delta = 3.4\,\mu$m, which is in good agreement with our in situ cloud images where the radial direction, which is physically smaller than a micron spreads over 3 horizontal pixels ($\Delta = 2.3\,\mu$m/pixel). Fig. 4.5 shows in a dot dashed line a value calculated from (4.2) (after applying the correct optical response per factor [71]). In our experiment the minimal $n_0\lambda_{dB} \approx 19$, although the gas is highly degenerate. Therefore replacing the Bose-Einstein occupation number $(i,\ j)$ by $i = j = 1$ as done in the Maxwell-Boltzmann approximation shouldn't be valid and higher terms in the sum need to be taken into account.

The atomic variance of the "cold" sample in Fig. 4.5 is higher than that of the thermal one, this is due to bosonic bunching as shown in (4.1); to fully fit this line one must integrate the equation over the transverse states while using the density-dependent chemical potential from (4.3). At high density (not shown in Fig. 4.5) the

measured fluctuations reduce compared to an ideal gas case since the sample enters the Thomas-Fermi region where the inter-atomic interaction increases and density fluctuations decrease.

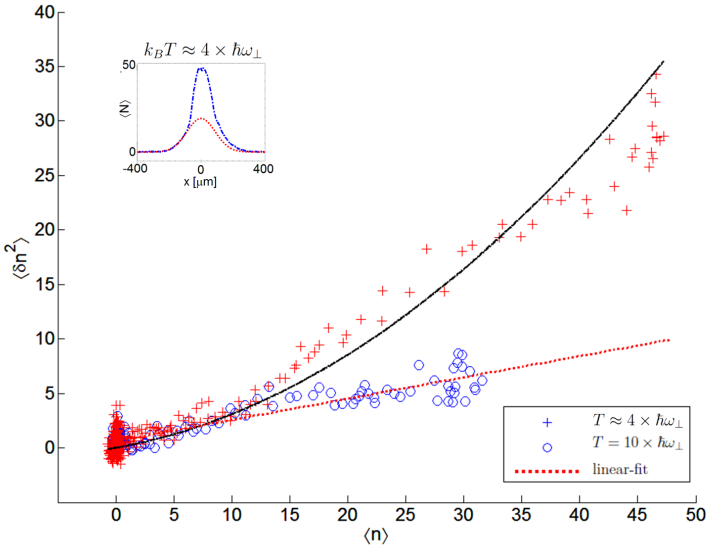

Figure 4.5: Atom number variance as a function of mean atom number per pixel. Open circles correspond to a "hot" sample ($k_BT \simeq 10 \times \hbar\omega_\perp$, $\omega_\perp = 2\pi \times 1190\,\mathrm{Hz}$), for which fluctuations are given by the atomic shot-noise. The plus (+) corresponds to clouds at a temperature of $k_BT \simeq 4 \times \hbar\omega_\perp$. The "cold" sample has excess fluctuations above shot noise due to bosonic bunching. The dot-dashed black line is the Maxwell-Boltzmann approximation using the measured temperature and trap parameters (see 4.2), while the linear line is the shot noise fit. The inset shows the mean atomic cloud density profile in blue; the Boltzmann fit function of the thermal part is in red.

5 Interaction Quenches in One-Dimensional Bose Gas

The coherence of one-dimensional quasi-condensate has algebraic decay along the long axis when the gas temperature is zero as a result of vacuum fluctuations, where in the case of temperatures higher than zero the gas will exhibit exponential decay in coherence. Both algebraic and thermal decay depend on the Luttinger parameter, i.e., the interaction strength of the system. What happens to the long-range correlations when the interaction strength of a system changes abruptly in a *quench* is still an open question. In such case the system needs to adapt to its new Luttinger parameter; the current approach suggests that the system will reach quasi-stationary state after some *prethermalization* time [16, 17, 18, 19, 20, 21].

The idea behind *prethermalization* is that a quantum or classical many body system, after much shorter time than equilibration time, dephases to some quasi-steady state from which the system thermalize to an equilibrium state. Although from earlier experiments it was seen that an integrable one-dimensional system tends not to thermalize over long timescales [23], abrupt changes in interaction strength drive the system to a 'thermalized' state via prethermalization. This phenomenon was seen by the dynamics of a split condensate by Gring et al. [21] and can be explained in the context of Ramsey interferometer as done by Kitagawa et al. [19]. In the case of Ramsey dynamics, slow equilibration is expected since the system consists of uncoupled low energy harmonic oscillators. In the condensate split case the interference contrast, given by the interference pattern of both clouds after a short flight time, can describe the physics of the dynamic of the split condensate. The temperature of a cloud with $T > 0$ is given by the thermal phase fluctuations where the energy distribution is given by the equipartition therm, and for which each momenta mode contains equal energy $k_B T$. When the split is sufficiently fast the energy contained in each momenta mode is independent, since the density difference along the condensate longitudinal axis is uncorrelated behind a distance given by "the spin healing length" [19]. Just after the split the two condensates are very much alike and the interference contrast is high, but after a long time the interference contrast becomes indistinguishable from a thermal condensate at a temperature that equals the splitting energy $k_B T_{\text{eff}} = E_{\text{split}}$. The time evolution of the local relative phase $\hat{\phi}_s(x) = \hat{\phi}_{\text{left}}(x) - \hat{\phi}_{\text{right}}(x)$ per point of the two condensates was examined by an integrable Tomonaga-Luttinger liquid formalism [102, 103]. It could be described in Fourier space as a set of uncoupled oscillators, or sound waves, with collective mode k that changes the density and phase profile of the condensate

in a sinusoidal fashion. Fast splitting equipartition distributes the energy between the k modes and the initial state begins to evolve. The different periods of time of each mode leads to dephasing and randomization of the relative phase.

5.1 Luttinger liquid theory

The 'Luttinger liquids theory' (LL) started as the harmonic liquid approach as formulated mainly by Haldane [104, 105]. LL is actually an alternative approach to approximating $1d$ harmonic fluids. The strength of this theory comes from three aspects, first it can be generalized to a unified treatment to Bosons and Fermions in $1d$ just by using a different structure in the correlation function. Second it is not a mean field theory, and therefore does not break any symmetry. Third it can deal simultaneously with weakly and strongly interaction systems, since the low-energy physics is parameterized by three phenomenological parameters (the particle density and two stiffness parameters). Although there is strength in this approach, it has a few inherent limitations. First since there is a built-in cut-off for high-energy structures it is impossible to describe any high-energy structures or any model-specific (i.e., non-universal) features [103]. Second when the interactions are strong it is difficult to map phenomenological parameters to microscopic ones; in such a case one should use the full derivation given by Bethe ansatz to map them.

5.1.1 The harmonic-fluid approach

In this section we will follow the work of Haldane and Cazalilla [104, 103] and learn the operator language of LL. The idea behind LL is to transform a $1d$ system of real particles to a set of coupled harmonic oscillators. The quanta of these oscillators refer to low energy phase and density fluctuations of the system.

The harmonic-fluid approach assumes a finite system at size L and mostly uses second quantization. This means that there is a Bosonic field operator that obeys $\left[\Psi\left(x\right),\Psi^{\dagger}\left(x'\right)\right]=\delta\left(x-x'\right)$, and commutes otherwise. Therefore $n\left(x\right)=\Psi^{\dagger}\left(x\right)\Psi\left(x\right)$ is the density operator, where n_0 is the ground state density. We first split the density into n_s and n_f, which refer to the 'slow' (long) and 'fast' (short) wavelengths, respectively, while we set a cut-off frequency such that the chemical potential would differentiate the two ($h\nu_{cut}=\mu$). It is convenient to introduce the operator $\Pi\left(x\right)$, defined by $n_s\left(x\right)=n_0+\Pi\left(x\right)$. We also introduce an auxiliary field operator $\Theta\left(x\right)$ with the following relation to density

$$\frac{1}{\pi}\partial_x\Theta\left(x\right)=n_0+\Pi\left(x\right), \tag{5.1}$$

where after integrating over x one gets $\Theta\left(L\right)-\Theta\left(0\right)=\pi N$. Now the Bosonic field

operator can be written as

$$\Psi^{\dagger}(x)=\sqrt{n(x)}\exp\left(-i\phi(x)\right)\sim\left[n_0+\Pi(x)\right]^{1/2}\sum_{m=-\infty}^{+\infty}e^{2mi\Theta(x)}e^{-i\phi(x)}, \tag{5.2}$$

where the sign $\sim$ represents a pre-factor in the field that is set by the cut-off point. Using the field operator and (1.25) the low-energy effective Hamiltonian reads [103]

$$H_{eff}=\frac{v_s}{2}\int_0^L dx\left[\frac{\pi}{K}\Pi^2(x)+\frac{K}{\pi}\left(\frac{\partial}{\partial x}\phi(x)\right)^2\right], \tag{5.3}$$

where v_s is the phase velocity of the low-energy excitations (sound waves), and K is the "Luttinger parameter", which is related to the strength of quantum fluctuations. This is a very strong approach since one can define many different systems using these two parameters.

5.1.2 Luttinger liquid of delta-interacting bosons

In this section we model Bosons with zero-range interacting potential such as s-wave scattering.

The parameters K and v_s need to be set as functions of interaction, γ. For low interaction, $\gamma\ll 1$, the parameters would be equal to

$$\begin{aligned} v_s&=v_F\tfrac{\sqrt{\gamma}}{\pi}\left(1-\tfrac{\sqrt{\gamma}}{2\pi}\right)^{1/2},\\ K&=\tfrac{\pi}{\sqrt{\gamma}}\left(1-\tfrac{\sqrt{\gamma}}{2\pi}\right)^{-1/2}, \end{aligned} \tag{5.4}$$

and for high interactions, $\gamma\gg 1$,

$$\begin{aligned} v_s&=v_F\left(1-\tfrac{4}{\gamma}\right),\\ K&=\tfrac{\pi}{\sqrt{\gamma}}\left(1+\tfrac{4}{\gamma}\right), \end{aligned} \tag{5.5}$$

where $v_F=\hbar\pi n_0/m$ is the Fermi velocity. A crucial point relates to the scaling of the system due to the cut-off in wavelength the system minimal length is the healing length, so for the Tonks-Girardeau gas a minimal cloud length would be $L_{min}=1/n_0\sqrt{\gamma}$.

The long range coherence can be obtained from the off-diagonal correlation in the system simply by using the Hamiltonian and field operator (5.2 and 3.13) such that for $T=0$ the result is [103]

$$\left\langle\Psi^{\dagger}(x)\,\Psi(0)\right\rangle\sim n_0\left(\frac{\xi}{|x|}\right)^{1/2K}, \tag{5.6}$$

where $\xi = \hbar/\sqrt{m\mu}$ is the healing length. At finite temperature T, higher energy modes are accessible and the equation reads

$$\left\langle \Psi^{\dagger}(x)\,\Psi(0)\right\rangle_{T} = -\frac{K}{2}\left(\frac{\pi/L_T}{\sinh(\pi x/L_T)}\right)^{2}. \tag{5.7}$$

In most experiments the cloud length is much longer than the thermal length ($L \gg L_T$); in such case the long distance correlation function can be reduced to

$$\left\langle \Psi^{\dagger}(x)\,\Psi(0)\right\rangle_{T} \sim -\left(\frac{2K\pi^2}{L_T^2}\right)\exp(-2\pi x/L_T), \tag{5.8}$$

where the thermal length is $L_T = \frac{\hbar v_s}{k_B T} = \frac{\hbar^2}{m\xi k_B T}$.

5.2 Theoretical background of the experiments[1]

The basic idea behind our experiment is to implement a quench in a gas of ^{87}Rb 1d quasi-condensate with temperature of $k_B T \lesssim \hbar\omega_\perp$ and atomic line density $n_{1d} < \frac{1}{2a_s}$. After the quench the gas is left to equilibrate and is measured at different relaxation times.

The interaction quench is introduced by a sudden change of the transverse frequency $\omega_{\perp i} \to \omega_{\perp f}$ corresponding to equal relative change in the coupling constant ($g_{1d} = 2\hbar\omega_\perp a_s \propto \omega_\perp$) $g_i \to g_f$. In order to avoid transverse excitations the quench should be slower than $1/\omega_\perp$ but faster than all other timescales. So the change will be adiabatic compared to the transverse frequency, $\omega_\perp$, but sudden for the longitudinal frequency, $\omega_{\shortparallel}$. The experimental observation of interest is the mean variation in atom number as a function of the mean atom number per pixel using in situ absorption imaging (as explained in sec. 4.2).

The excess of fluctuations compared to the shot-noise level of uncorrelated atoms is a function of atomic bunching of ideal Bose gas and hence is a function of temperature and trap parameters (see 4.1). Therefore change in the radial frequency would change the variance; an effective temperature that is time dependent will be our new variable, which directly relates to prethermalization.

5.2.1 Theory for $T = 0$

The Luttinger liquid theory for an ideal Bose gas at $T = 0$ is explained in sec. 5.1. As stated, the ground state correlation function decays algebraically $\left\langle \Psi^{\dagger}(x)\,\Psi(0)\right\rangle \sim n_0\left(\frac{\xi}{x}\right)^{1/2K}$. In the case of sudden quench the interaction strength changes $g_i \to g_f$.

[1] This theory part is based on collaboration with Ehud Altman and Susanne Pielawa from Weizmann Institute.

Right after the quench each Luttinger mode will be in a squeezed state of the new Hamiltonian (3.13), with squeezing parameter

$$r = \operatorname{artanh}\left(\frac{1-\sqrt{g_i/g_f}}{1+\sqrt{g_i/g_f}}\right). \tag{5.9}$$

It is important to mention that the squeezing parameter does not depend on momentum q, and so the quench pushes the same "number" of excitations into each mode. This is different from the split condensate case presented before since there the number of excitations per mode follows the equipartition function as in thermal distribution.

We will look now at two-point correlation function oscillations in time at a momentum q. The function showing the noise of the quadratures (between having reduced uncertainty and having large uncertainty), each with its own frequency

$$\langle\varphi_q\varphi_{-q}(t)\rangle = \frac{\pi}{2|q|K_f}\left[e^{2r}\sin^2(v_s q t) + e^{-2r}\cos^2(v_s q t)\right], \tag{5.10}$$

where we can define the phase velocity as $v_s = \sqrt{\frac{n_{1d}g_{1d}}{m}}$ and the Luttinger parameter as $K = \pi\hbar\sqrt{\frac{n_{1d}}{mg_{1d}}}$ [106]. It is possible to get the form of the correlation functions analytically as a function of time, see [107], and one sees that for a finite system it oscillates in time, i.e., there should be revivals.

To describe the transient state after a long enough time scale so the system dephases, we can average over the sine and cosine so that

$$\langle\varphi_q\varphi_{-q}(t)\rangle \to \frac{\pi}{2|q|K_f}\cosh(2r) = \frac{\pi}{2|q|K_f}\frac{(g_i+g_f)}{2\sqrt{g_i g_f}} \tag{5.11}$$

and the correlation will decay with a new exponent

$$\left\langle\hat{\psi}^\dagger(x)\hat{\psi}(0)\right\rangle = n_0\left(\frac{\xi}{|x|}\right)^{\frac{1}{2K_f}\cosh(2r)} = n_0\left(\frac{\xi}{|x|}\right)^{\frac{1}{2K_{\text{eff}}}}. \tag{5.12}$$

The effective Luttinger parameter and effective interaction can now be defined in the sense that the two-point correlation function after dephasing will look to be the ground state correlation function of a Bose gas with these parameters:

$$\begin{aligned} K_{\text{eff}} &= K_f\frac{2\sqrt{g_i g_f}}{g_i+g_f} \\ g_{\text{eff}} &= \frac{g_i}{4}\left(1+\frac{g_f}{g_i}\right)^2 = \frac{g_f}{4}\left(\sqrt{\frac{g_i}{g_f}}+\sqrt{\frac{g_f}{g_i}}\right)^2. \end{aligned} \tag{5.13}$$

This dephased ground state can be called a prethermalized state with typical dephasing time of $\tau_{pre} = L/c$, where L is the condensate length and $c = \sqrt{2\hbar\omega_\perp n_{1d}a_s/m}$ is the speed of sound. The system in this prethermalized state has excess energy that still needs to be distributed, the way and timescale in which this energy is distributed is still an open question. Where these time scales are expected to be much longer [19].

5.2.2 Finite temperature

Our experiment is performed at a minimal finite temperature that is still $T > 0$. As explained, algebraic decay is generated by vacuum fluctuations of the zero temperature condensate but at higher temperatures; exponential decay dominates at sufficiently long scales. The correlation decay function according to Imambekov et. al. is [108]

$$g_1(x,0) = \frac{\left\langle \hat{\psi}^\dagger(x)\,\hat{\psi}(0)\right\rangle}{n_{1d}} = \exp\left(-\frac{1}{2K}\pi\frac{x}{\xi}\frac{k_BT}{\mu}\right), \tag{5.14}$$

as long as $x \gg \xi\frac{\mu}{k_BT}$. If $k_BT > \mu$ we can define the thermal length as $L_T = \frac{2K\xi\mu}{\pi k_BT}$, which is linearly dependent on K. Some thermalization time after the quench the excitations introduced by the quench will reduce the decay length according to the effective Luttinger parameter. It is still an open question if the decay length now will be governed by the same K_{eff} as in the $T = 0$ case, or that at finite temperature other processes become dominant.

5.3 Experimental results

In this section we present the partial experimental results we accumulated. An atomic cloud of ^{87}Rb atoms in the $|F = 2,\ m_F = 2\rangle$ state was trapped in a highly anisotropic magnetic trap ($\lambda = 132$) using a combination of the atom chip and understructure wires, the first for the radial confinement, the second for the longitudinal one (as explained in sec. 3.2). We could tune the transverse frequency between 1 and 1.5 kHz while keeping the longitudinal frequency at a value of about 9 Hz. We cooled the sample using evaporative cooling in the final trap and let it relax for 15 ms reaching temperatures as cold as $3.2\hbar\omega_\perp/k_B$ and atom number of 4.5×10^3 atoms. The cloud length was about 300 μm and had a transverse length before release of about 300 nm; after 1 ms the cloud reaches a radial size of about 2.5 μm, which is about the effective pixel size. At this radial cloud width the light wont bypass the cloud in the transverse direction while imaging. To apply the quench a current of 1.5 A was pushed through the chip wire holding the cloud at a distance of 105 μm from the chip. Without changing any other parameter we reduced the current in the chip wire to 0.8 A within 5 ms such that the change is adiabatic compared to the transverse frequency, but sudden for the longitudinal one. In Tab. 5.1 the trap an cloud values are presented where one can see the change in the traps aspect ratio, λ, and distance from the chip, h, during the quench. While in Fig. 5.1 there is a simulation of the change in the trap.

We measured the change in the atomic variance as a function of time before and after the quench. After reaching BEC in the final trap we let the atomic sample equilibrate for 15 ms; data were taken at this point (see Fig. 5.2). We quenched the

Trap	$\omega_\perp$	ω_L	$\bar{N}$	L_x	λ	h
Final	$2\pi \cdot 1190\,\mathrm{Hz}$	$2\pi \cdot (9)$ Hz	$4.5\,k$	$300\,\mu$m	132	$105\,\mu$m
Quench	$2\pi \cdot 1380\,\mathrm{Hz}$	$2\pi \cdot (9)$ Hz	$4.5\,k$	$300\,\mu$m	153	$29\,\mu$m

Table 5.1: Measured (theoretical) trapping frequencies and atom numbers for the two magnetic traps. L_x represents the typical full longitudinal length, $\lambda = \frac{\omega_\perp}{\omega_x}$ is the aspect ratio, and h is the cloud's distance from the chip.

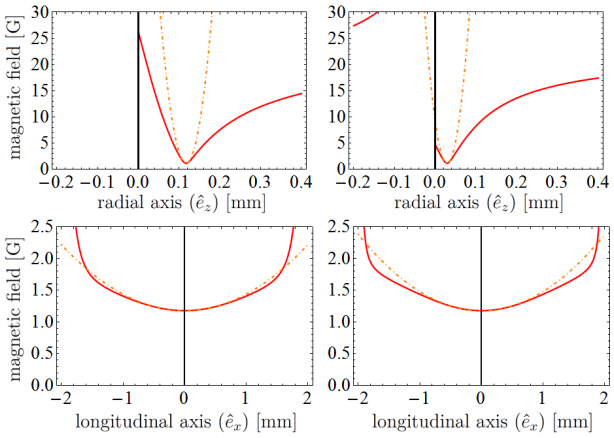

Figure 5.1: A simulation of the magnetic field before and after the quench. Point z=0 represents the chip where x=0 is the center of the under structure IP z trap. In red is the total magnetic field and in orange is the harmonic approximation. Left: the "final" trap. Right: the "quench" trap. The change was done at a rate of 200 Hz (5 ms), which is adiabatic compared to the transverse trapping frequency and abrupt for the longitudinal one.

trap as previously explained and took two sets of data at 2 ms and 5 ms dark times after the quench is complete. The data in Fig. 5.2 was taken using in situ images ($t_{\mathrm{TOF}} = 0$) with imaging pulse duration of 100 μs. It is interesting to see that shortly after the quench the variance reduced just slightly, where for longer time one can see a real reduction of the variance. This phenomenon can point to the fact that shortly after an abrupt change in interaction ($g_f/g_i = 1.16$) there is almost no change in the variance since the system hasn't thermalized in an observable way, where after 5 ms dark time the large decrease probably was due to per-thermalization processes.

In Fig. 5.4 we used a different type of measurement. Here we released the cloud from the trap and let it freely evolve for 1 ms; during this short time of flight the radial size of the cloud increased such that the resolution would fit the actual cloud size. As previously explained, in such short time scales the longitudinal density profile almost does not change. In this figure we present three data sets. The bottom one is the thermal reference ($\circ$), which is linear where the red and black ($\triangle$ and $\Diamond$) present 0 ms and 5 ms dark time after the quench is complete, respectively. We know from the previous profile that shortly after the quench the variance does not

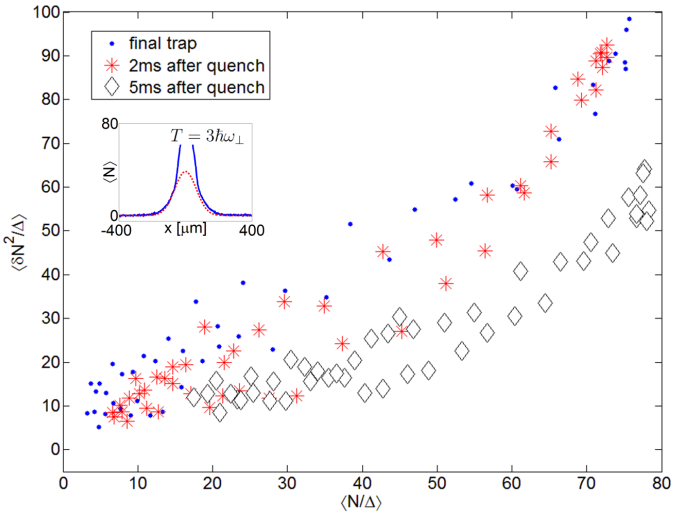

Figure 5.2: Atom number variance as a function of mean atom number per pixel at three different times. The first data set ($\cdot$) is for the final trap after 15 ms dark time. We then quickly shifted the cloud to the quench trap and a data set was taken after 2 ms dark time ($\star$). The third data set ($\Diamond$) was taken with a hold time of 5 ms both after the quench is complete. One can see that there is almost no change in the atomic variance right after the quench, but as function of time the variance decreases. The inset shows the cloud temperature before quenching.

change. Here, since the resolution is better, we can see that for high density the red curve ($\triangle$) starts to flatten out. This is due to an increase in mean field energy that reduces bunching. Since the sample can be treated as nearly integrable system a per-thermalization plateau will appear where the system relax to a non-thermal steady state [109].

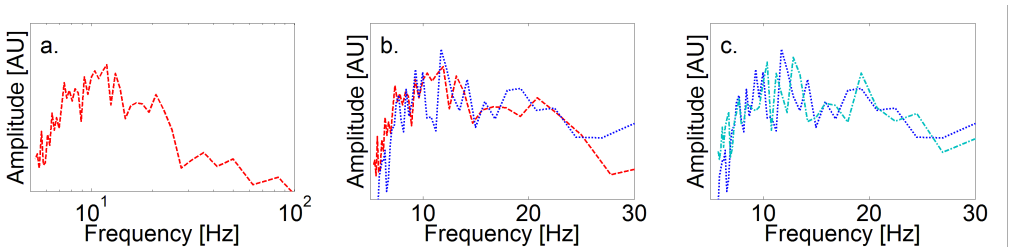

Figure 5.3: A mean Fourier transform of the in situ density profile investigated in Fig. 5.2. a. shows the final trap. b. shows the final trap (dashed) and quench trap after 2 ms dark time (dot). c. shows the quench trap after 2 ms and 5 ms dark time (dot and dot dash, respectively).

In Fig. 5.3 a Fourier transform of the in situ density profile from Fig. 5.2 is presented.

The transformation was done as follows, each cloud image was converted to a single vector for which we binned the transverse direction, from which we have calculated the variance as exsplained in sec. 4.2.1. Then we transformed the variance using *FFT* function in matlab, the conversion between wavelength to frequency was found using the correct speed of sound $\left(c=\sqrt{2\hbar\omega_{\perp}n_{1d}a_s/m}\right.$ i.e. using the right value of $\omega_{\perp}$). For each dark time we have transformed a large number of images, these transformed vectors were averaged to a single mean vector, $\langle FT\left[\delta N\left(x\right)\right]\rangle$. Later each of these mean vectors was normalized by its area, $\langle FT\left[\delta N\left(x\right)\right]\rangle / \int\langle FT\left[\delta N\left(x\right)\right]\rangle dx$.

The minimal frequency is about 5 Hz, which is $\frac{1}{2}\nu_{\parallel}$ as it should be. At plot (a) the final trap FT is shown on a log scale with frequencies of $5-100$ Hz. The main contribution is of modes up to $3\times\hbar\omega_{\parallel}$, where higher modes carry almost no energy. Once the quench is applied three changes happen. First, the interaction strength increases, second excess energy is added to the system, and third the speed of sound changes. In plot (b) a shift in frequency domain is visible, although the variance in Fig. 5.2 stayed constant. This shows the excess energy given to modes of the system. If we compare the change as a function of dark time after the quench is complete, in plot (c) the shift of the peaks is very clear. We attribute this change to the decoherence process of the different modes as also seen in the variance.

We still don't know the mechanism that governs this thermalization process due to lack of experimental data. Although we believe that as many different processes in nature where the equilibrium point changes, here excess energy adds to the system along with change in the interaction parameter. The system might reach its new equilibrium state as a damped harmonic oscillator. The quench gives excess energy to all reachable modes (up to a cutoff), as explained in sec. 5.2, where these uncoupled modes now need to dephase. As part of their dephasing process such damped harmonic oscillator behavior might be seen in the value of $\langle\delta N^2\left(\langle N\rangle,t\right)\rangle$ as a function of dark time [110].

5.4 Experimental outlook

In this chapter we investigated the theoretical and experimental aspects of interaction quench on a quasi-condensate. The system of interest was a highly anisotropic atomic cloud with temperature as cold as $k_BT=3\hbar\omega_{\perp}$. The measurements were part of a joint project with Ron Folman's atom chip lab in BGU. Unfortunately, the project had to be paused before gathering the full experimental spectrum and later could not be continued before replacing the chip, due to a technical problem in the atom chip setup. Therefore a full experimental analysis could not be done, although we have a good understanding that needs to be proven theoretically or experimentally on the expected behavior of such systems followed by interaction quench.

We believe that there are many different processes in nature where the equilibrium

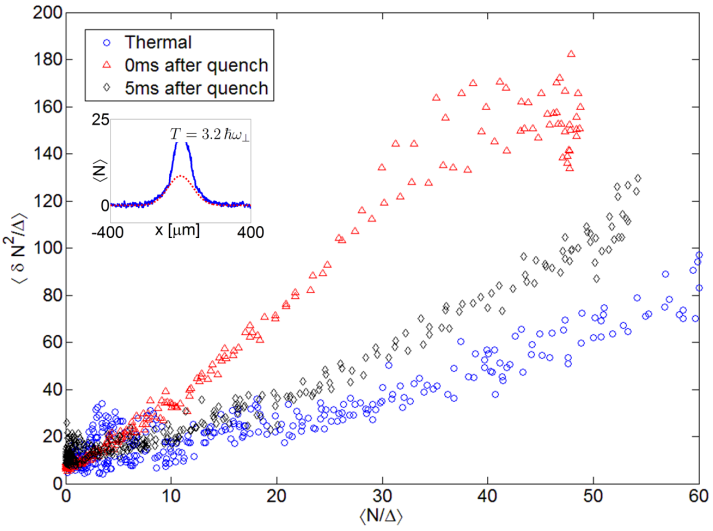

Figure 5.4: A plot similar to Fig. 4.5. Here we present the atomic variance at two different dark times after the quench is complete with a thermal reference. The images were taken after a short time of flight of 1 ms. The inset shows the cloud temperature before quenching.

point changes as a result of excess energy that is added to the system along with change in the interaction parameter. The system will find its new equilibrium state as a damped harmonic oscillator. The quench gives excess energy to all reachable modes (up to a cutoff) as explained in sec. 5.2, where these uncoupled modes now need to dephase. As part of their dephasing process such damped harmonic oscillator behavior might be seen [110]. Therefore with sufficient experimental data the evolution of the system following quench in the interaction strength parameter would be able to be observed. We believe that following an interaction quench oscillations in the in the density of the gas will occur, these oscillations will persist until the system will reach a new steady state value. This behavior can be seen by the atomic variance which in such case should change its value as given by the well-known damped harmonic oscillators equation $\frac{d^2\langle \delta N^2(N,t)\rangle}{dt^2} + 2\zeta\omega_0 \frac{d\langle \delta N^2(N,t)\rangle}{dt} + \omega_0^2 \langle \delta N^2(N,t)\rangle = 0$, where ω_0 is the undamped angular frequency of the oscillator and ζ is the dumping ratio. The value of ζ will play a critical role here, since for any $\zeta > 1$ the system will be overdamped and will decay to its new value exponentially, where for $\zeta < 1$ the system will oscillate to its new position. Further experimental and theoretical effort needs to be done to reach a final conclusion.

6 Zippers and Quantum Mechanics: A proposal for measuring the dynamical Casimir effect

Time-dependent manipulations of Bose-Einstein condensation is a new and evolving field. New technological methods allow the creation of local manipulation at a smaller scale than the condensate length by precise and local means as extremely focused laser beams [111], atom chips [26], and rf splitting [29, 84]. In this chapter we present a new atom chip design that can create local time-dependent rf split of an elongated atomic cloud along its quantization axis. The interference picture of such unique split condensate after some time of flight can grant us the opportunity to investigate effects that are unique for quantum mechanics, such as the dynamical Casimir effect [112], Hawking radiation [113], and vacuum energy.

A surprising outcome of quantum field theory is that the vacuum space is not empty, but a field with couples of correlated virtual particles and anti-particles flitting in and out of existence. These quantum fluctuations seem to have a cross-effect on many other fields such as the Lamb shift [114] of the atomic spectra, or modification to the magnetic moment of the electron [115]. A more direct theory was presented about 40 years ago by Moore [116], where he suggested that a conductive mirror undergoing a relativistic motion can excite the vacuum and convert virtual photons into real ones. Later this effect was called Dynamical Casimir Effect (DCE).

In 1984 Casimir suggested that a pair of mirrors or conductive plates can measure vacuum fluctuations [112]. Casimir predicted that two parallel conducting metal plates in a vacuum will experience attractive force. The reason is that in a vacuum the sum of virtual ground state modes is almost infinite $E_{\text{vacuum}} = \sum \frac{1}{2}\hbar\omega_{\text{v}}$, where placing a pair of parallel plates creates boundary conditions that allow only $\omega_{\text{plates}} = \frac{2\pi c}{L}\left(n + \frac{1}{2}\right)$ modes to exist in-between, where L is the distance between the plates and c is the speed of light. The vacuum radiation pressure between the plates is lower than the pressure outside, generating a force (although it can be also explained by means of Van der Waals force). This force is called the static Casimir effect and is due to a mismatch of vacuum modes in space. On the other hand, the dynamical Casimir effect is a mismatch of vacuum modes in time, since the plate by its movement changes the spatial mode structure of the vacuum. In order that the movement will create a non-adiabatic change in the Vacuum, v/c should be non-negligible, otherwise the EM field can smoothly adapt to the new boundary

condition. A simplified way to understand the DCE is by treating the two conductive plates as having zero sum charged particles, which enforce the boundary condition by a screening effect of the external EM field. If the plates oscillate in an EM field the screening current will emit EM radiation, similar to an antenna. Classically, if the external EM field will be taken to zero the radiation dumping will also reduce to zero, but since there are vacuum fluctuations the plates will continue to emit real photons as a response to the vacuum modes.

Creating such an experiment is not feasible as seen by Braggio et al. [117], who calculated that for a microwave antenna that moves at a frequency of 2 GHz and with a displacement of 1 nm (gives v/c ratio of 10^{-7}), the emission rate will be approximately one photon per day. Another problem he saw was that the device needs to be cooled to a temperature as cold as 20 mK, where the mechanical energy needed for the system is 100 MW. Other projects have been suggested such as nano mechanical resonators or surface acoustic waves [118, 119, 120, 121, 122, 123, 124, 125, 126]. A successful experiment was done in 2010 by Wilson et al. [127] where they used a SQUID device to modulate the electrical properties of a cavity. The SQUID acts as a parametric inductor whose value can be tuned by applying a magnetic flux through the SQUID loop.

In this proposal we suggest a method to investigate the dynamical Casimir effect, Hawking radiation, and the effect of dynamic split on the phase pattern of a quasi-1d condensate.

The proposed experiment is part of a collaboration with Serena Fagnocchi, Ehud Altman, and Eugene Demler.

6.1 Analogue model

Quantum particle production induced by the motion of boundary conditions is a longstanding issue of quantum field physics [116]. The literature about DCE is enormous [128, 129, 130, 131, 132, 133, 134]. The original example of DCE is in quantum electrodynamics, where photons are emitted due to the motion of the conducting surfaces, but more generically it has referred to all the time-dependent changes of the system geometry or of the properties of the medium, and therefore the fields where it finds applications are extremely wide (quantum optics [135, 136, 137], cold atoms [25, 24, 138], gravity [139], super-conducting materials [123, 124, 140], and more). DCE is a milestone of Quantum Field Theory appearing whenever motion of a boundary condition is able to excite the quantum vacuum. This can be seen both as a particle creation for non-adiabatic change of the boundary conditions of quantum fields, or as parametric excitation from vacuum of quantum field modes. The spectrum of the emission depends strictly on the motion of the boundary. This is in fact a kinematic effect, related essentially to the mode propagation (and reflection), and therefore substantially independent from the micro-physical theory describing

the specific system. Observable effects of quantum particle emission would open a window on the properties of quantum vacuum at a macroscopic level.

In particular, in semi-classical gravity the motion of a reflecting boundary is able to mimic the key features of the black holes' evaporation process (Hawking radiation [113]). In fact, both Hawking effect and any other effect predicted within the semi-classical theory of gravity have no experimental observation. This analog model type of experiment should shed light on the behavior of quantum black holes, and on the underlying formalism itself.

In this proposal we suggest a new framework for testing DCE in the context of matter interferometer physics with a Bose-Einstein condensate [141].

6.1.1 Theoretical analysis

Let us consider an extremely elongated Bose-Einstein condensate (BEC) with constant density flowing into a Y-junction and splitting into two arms (see Fig. 6.1). After the split the two arms evolve as two independent condensates. Therefore away from the splitting (or merging) point, the phase difference $\hat{\varphi}(x,t) = \hat{\varphi}_1(x,t) - \hat{\varphi}_2(x,t)$ is described by the following action

$$S(\varphi) = -\frac{K}{2}\int dtdx\left[(\partial_x\hat{\varphi})^2 - \frac{1}{c^2}(\partial_t\hat{\varphi})^2\right], \tag{6.1}$$

where K is the Luttinger parameter, and c is the sound velocity, which will be set equal to 1 hereafter. While in the case of the one-time full split, the phase difference

Figure 6.1: Scheme of the split condensate through a Y-junction.

between the two arms is completely randomly defined. Here the junction point merging the two arms forces this difference to vanish, providing a strict constraint. Moreover, this boundary condition moves while unzipping the condensate. In fact, in the rest frame of the condensate, the splitting point can be seen as moving along a particular trajectory $x_b(t)$, which is experimentally controlled. The unzipping process is able excite low energy phonons by means of this non-trivial time-dependent boundary condition in a perfect reproduction of the boundary-induced radiation proposed by Moore [116]. In fact, from (6.1) the equation describing $\hat{\varphi}(x,t)$ is the D'Alembertian equation

$$\left(\partial_t^2 - \partial_x^2\right)\hat{\varphi} = 0 \tag{6.2}$$

with the following boundary conditions

$$\hat{\varphi}|_{x_m(t)} = 0 \tag{6.3}$$

$$\partial_x \hat{\varphi}|_{x=0} = 0. \tag{6.4}$$

The first is due to the vanishing of $\hat{\varphi}$ at junction point $x_m(t)$. The second comes from requiring zero current at the edge of the two arms of the condensate[1] ($x = 0$). In this proposal the splitting point and the edge of the condensate play the role of perfectly reflecting boundaries, and their relative motion is able to generate quasi-particle excitations (phonon modes). The presence of emitted quasi-particles will be observed in an interference experiment, once the split cloud is released from the trap and expands and overlaps [142]. After the trap release, the cloud is imaged using light sheet imaging [67], and the resulting interference pattern is recorded providing insight of the quantum DCE emission, for example in the coherence or in the total contrast, both strictly dependent on the relative phase two-point correlater.

6.1.2 Generic trajectory

The solution of (6.2, 6.3, and 6.4) is not known for general unzipping trajectories $x_b(t)$. Yet if one starts with a condensate with an initial non-vanishing unzipped part, or waits long enough to get the split part longer than the healing length, one can then assume the split part is sufficiently big to set at infinity the BEC edge (initially set at $x = 0$). The problem will be reduced to just considering the phase difference $\hat{\varphi}$ as a quantum scalar field (6.2) in a (half-)infinite space with the only boundary condition (6.4) at the junction point $x_b(t)$. In this situation the constant velocity unzipping would not be distinguishable from the static solution, because of the Galilean invariance under constant velocity change of the reference frame. The correlaters reduce to the vacuum ones without producing excitations. In the single-boundary case non-uniformly accelerated motion of the boundary is necessary to get field excitations [139]. In this situation it will be convenient to think in terms of right- and left-moving modes. Therefore let's choose the set of coordinates $U = t - x$ and $V = t + x$ appropriate for describing left $e^{-i\omega f(U)}$ and right $e^{-i\omega g(V)}$ moving modes, f, g being appropriate functions depending on the motion of the boundary. The problem (6.2, 6.3) then translates to

$$\hat{\varphi}_\omega = \frac{1}{\sqrt{4\pi\omega}} \left(e^{-i\omega V} - e^{-i\omega V_b(U)} \right) \quad \omega > 0, \tag{6.5}$$

which is manifestly the solution of (6.2). In this context a quantity that is of particular interest is

$$e^{i\langle \hat{\varphi}(x) - \hat{\varphi}(x') \rangle} = e^{i\langle \hat{\varphi}(x)\hat{\varphi}(x') \rangle - 1/2 \left\langle \hat{\varphi}(x)^2 \right\rangle - 1/2 \left\langle \hat{\varphi}(x')^2 \right\rangle} = e^{A(x,x')} \tag{6.6}$$

[1] It is also possible to fix $\hat{\varphi}|_{x=0} = 0$, reproducing exactly the situation described by Moore [116]. Nevertheless we check that there is no essential change in the results.

where we have defined A as the argument in the exponent. A is a good quantity once the split part is long enough to neglect the edge of the condensate, as a result we can also neglect $\left\langle e^{\hat{\varphi}(x)} \right\rangle$ left moving particles since they would not have their phase fixed by the boundary "mirror" reflection that ensures that $\left\langle e^{\hat{\varphi}(x)} \right\rangle = 0$. (6.1) for semi-infinity-long condensate (space-time) can be computed by knowing that $e^{\langle \hat{\varphi}(U,V)\hat{\varphi}(U',V')\rangle}$ is given by [143]

$$\langle \hat{\varphi}(U,V)\hat{\varphi}(U',V')\rangle = -\frac{1}{4\pi K} \ln \frac{(V_b(U) - V_b(U'))(V - V')}{(V_b(U) - V'))(V - V_b(U'))}. \tag{6.7}$$

One can also get $\langle \hat{\varphi}(x)^2 \rangle$ (to calculate A) by taking the double limit $t' \to t,\ x' \to x$ of the previous (6.6), then inserting everything into (6.6) and taking the limit $t' \to t$ to get the answer (see example in the following section).

6.1.3 Still split point

For a zero time split the quantity in (6.6) can be computed by substituting $V_b(U) = U$ into (6.7):

$$\langle \varphi(U,V)\varphi(U',V')\rangle = -\frac{1}{4\pi K} \ln \frac{(U - U')\,(V - V')}{(U - V')\,(V - U')} = -\frac{1}{4\pi K} \ln \frac{(x - x')^2}{(x + x')^2}. \tag{6.8}$$

Now we can evaluate $\langle \hat{\varphi}(x)^2 \rangle$ by taking the double limit in (6.8)

$$\left\langle \hat{\varphi}(x)^2 \right\rangle = \lim_{x' \to x,\, t' \to t} -\frac{1}{4\pi K} \ln \frac{(x - x')^2}{(x + x')^2} = -\frac{1}{4\pi K} \ln \frac{\xi^2}{2x^2} \tag{6.9}$$

since the healing length is approximately the minimal distance between two points. Therefore A reads

$$A_{StillSplit} = -\frac{1}{4\pi K} \ln \left(\frac{(x - x')^2}{\xi^2} \cdot \frac{2xx'}{(x + x')^2} \right), \tag{6.10}$$

where ξ is the healing length, and from which the coherence (Fig. 6.2)

$$e^{i\langle \hat{\varphi}(x) - \hat{\varphi}(x')\rangle} = \left(\frac{\xi}{x - x'} \cdot \frac{x + x'}{\sqrt{2xx'}} \right)^{1/(2\pi K)}. \tag{6.11}$$

The $\left(\frac{\xi}{x-x'}\right)^{1/(2\pi K)}$ part is the vacuum one that dominates far from the split point, the other is a correction due to the presence of the boundary that indeed breaks the translational invariance.

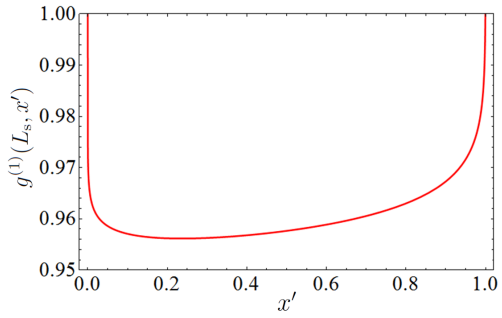

Figure 6.2: $g^{(1)}(L_\mathrm{s}, x')$ plot for the still split in 1d ^{87}Rb cloud at a temperature of 82 nK and trap frequency of 3.3 kHz. The calculations take into account clouds that are released just after the split (trap data taken from [84]).

6.1.4 Constant velocity split

The case of the constant velocity (CV) trajectory $x_b(t) = vt$, where $v < 1$ (c), is the velocity at which the split point moves apart, translates to the U, V coordinates simply by $V_b(U) = \alpha U$, where $\alpha = (1+v)/(1-v)$ is a constant too. Inserting this trajectory into (6.7) and evaluating the coincidence limit one gets A to be:

$$A_{ConstV} = -\frac{1}{4\pi K} \ln\left(\frac{(x-x')^2}{\xi^2} \cdot \frac{(V-\alpha U)(V'-\alpha U')}{(V-\alpha U')(V'-\alpha U)}\right) \tag{6.12}$$

For $v = 0$, $\alpha = 1$ and this reduced to eq. (6.7). From (6.12) the coherence becomes (Fig. 6.3)

$$e^{i\langle\hat{\varphi}(x)-\hat{\varphi}(x')\rangle}(\mathrm{CV}) = \left(\frac{\xi}{x-x'}\right)^{1/(2\pi K)} \cdot \left(\frac{1-\alpha\frac{(t-x)(t-x')+(t+x)(t-x')}{(t+x)(t+x')+\alpha^2(t-x)(t-x')}}{1-\alpha\frac{(t-x')(t+x')+(t-x)(t+x)}{(t+x)(t+x')-\alpha^2(t-x)(t-x')}}\right)^{1/(2\pi K)}, \tag{6.13}$$

where it is clearly separated the vacuum contribution and the correction, which reduces to 1 for a large split part (or long times).

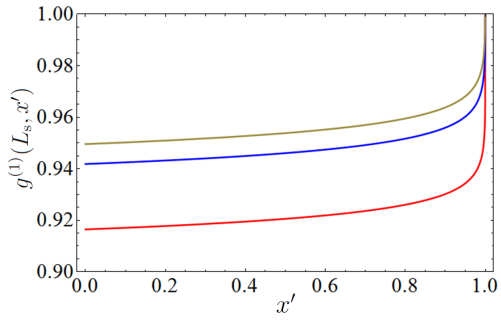

Figure 6.3: $g1(L_s, x')$ plot for constant velocity split. The trap values are similar to Fig. 6.2. The barrier speeds (v_b) are 0.1c, 0.5c, and 0.9c and the time is $t = L_s/v_b$. The coherence drops with speed. For $t = 0$ and $v_b = 0$ the figure is identical to Fig. 6.2.

In this trajectory it is interesting to see that the higher the split velocity the lower the coherence. This is because when the split velocity is adiabatically low the system has time to communicate (via interaction) and adapt, where for fast trajectories the change becomes non-adiabatic and the coherence reduces in a more drastic way. If the split time is long, such that the distance between the two boundaries can be set to be infinite, the system becomes Galileo invariant under constant velocity transformation of the reference frame. In this case the system will be considered as static, and therefore given no excitations.

6.1.5 Exponential junction trajectory

Now we focus on a very special boundary trajectory: $V_b(U) = -ae^{-\kappa U}$, where a and κ are constants and κ has the dimension of a frequency. Inserting this trajectory into (6.7) and evaluating the coincidence limit considering $e^{-\kappa U} - e^{-\kappa U'} \sim k\xi e^{-\kappa U}$, one gets A to be:

$$A_{exp} = -\frac{1}{4\pi K} \ln\left(\frac{2\sinh(\kappa(U'-U)/2)}{\xi}\right) \times (\text{correction}) \tag{6.14}$$

where the correction reads:

$$\frac{\sqrt{ae^{-\kappa U} - V}\sqrt{V - ae^{-\kappa U}}\sqrt{ae^{-\kappa U'} - V'}\sqrt{V' - ae^{-\kappa U'}}}{(ae^{-\kappa U} - V')(V - ae^{-\kappa U'})} \sim 1 \tag{6.15}$$

for late times when $\kappa t \gg 1$ (and $\mid e^{-\kappa U} \mid \ll \mid V \mid$). Therefore in the late times limit the coherence becomes (Fig. 6.4)

$$e^{i\langle\hat{\varphi}(x) - \hat{\varphi}(x')\rangle}(\text{Exp}) = \left(\frac{\xi}{2\sinh(\kappa(x-x')/2)}\right)^{1/(4\pi K)} \tag{6.16}$$

showing a behavior very different from the one shown by the vacuum.

The peculiar exponential decay of the correlations for the right movers U-modes reflected by the junction point is a clear signature of the thermal production rate, induced by the exponential motion of the boundary. Such a signal in an interference experiment would be clear evidence of DCE, but its relevance would go beyond the pure DCE associated with it. This would provide the first observation of a quantum process that is analogous to the Hawking radiation in black holes.[2].

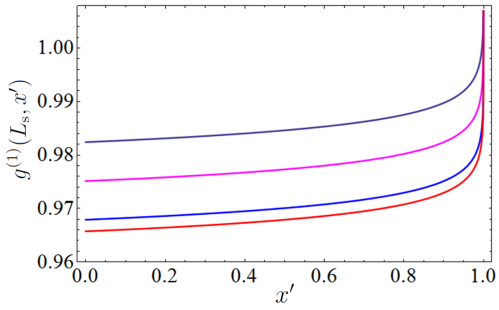

Figure 6.4: $g1(L_s, x')$ plot for exponential split. The trap values are similar to (Fig. 6.2). The values of κ are 0.1, 1, 10, 20 where as κ gets larger as the coherence drops.

6.1.6 Hyperbolic split

In the case of hyperbolic trajectory $t^2 - x^2 = -\alpha^2$, $\alpha^2 > 0$ a constant, translates into $UV_b = -\alpha^2$, then $V_b(U) = -\frac{\alpha^2}{U}$. Inserting this trajectory into (6.7) and evaluating the coincidence limit one gets A to be

$$A_{Hyp} = -\frac{1}{4\pi K} \ln\left(\frac{(x-x')^2}{\xi^2} \cdot \frac{(UV+\alpha^2)(U'V'+\alpha^2)}{UV'+\alpha^2)(U'V+\alpha^2)}\right). \tag{6.17}$$

The first term is the usual vacuum one, while the part after the $\cdot$ is a correction in the late time limit $t > \alpha$, and therefore $|UV| \gg \alpha^2$ reduces to 1. As a consequence, the coherence at late times reduces to the vacuum coherence.

[2]Hawking radiation is indeed a thermal flux of particles arising after the horizon of a black hole has formed. Early time Minkowskii modes convert into non-trivial ones due to the distortion of space-time for the collapsing body. Regardless the specific details of the collapse, the red-shift that modes suffer close to the horizon is always exponential: $-\frac{1}{\kappa}e^{-\kappa U}$ with a geometrical parameter called "surface gravity" on the horizon [139]. The very same distortion, and therefore the same thermal particle production, is obtained by the mode refection on a boundary following the exponential trajectory $\left(V_b(U) = -ae^{-\kappa U}\right)$ with $a = 1/\kappa$. This can represent a very powerful tool to explore the mechanism behind one of the most famous and elusive predictions of QFT in curved spaces, and can even provide the first validation for the formalism itself. [by SF]

6.2 Experimental outline

In our scheme we intend to time-dependently spatially split a cigar shape quasi-1d BEC cloud of ^{87}Rb atoms by changing the trapping potential from a single to a double-well. We do so by extending a confining potential along the cloud longitudinal direction while creating a Y-shape split cloud (Fig. 6.1). For this kind of experiment the energy barrier should be high enough to prevent tunneling between the two split arms. In order to create such a "moving barrier," or dynamic split, we use spatial and time dependent rf dressed potential, which will be explained later. Atom chips are good candidates for such experiments since the smoothness of their micro-wires allows creation of very accurate spatially dependent potentials. So by applying alternating current through a series of fabricated adjacent ⊔ shaped micro-wires on the atom chip surface one can create such moving rf dressed potential.

Our condensate is created by a combination of magnetic fields from currents in Z-shaped micro-wires on an atom chip surface and external bias fields. In addition, we use two parallel straight micro-wires, which will reduce the longitudinal confinement (Fig. 6.6 c). Such combination can create relatively straight quadrupole cigar shape trapping potential with a non-zero minimal field at the cloud center, known as an Ioffe field. In the case of quasi-1d BEC, the chemical potential μ should be less than the trap's transverse confinement ($\hbar\omega_\perp$) and $\omega_\perp$ should be high enough so the cloud radii would be in the order of the healing length, although preventing creation of vortexes ($a_\perp \leq 2\xi$ see sec. 3.2.1). In the theory part we treat the cloud temperature as low enough so the length of the cloud won't be longer than the 1d coherence length. Hence there will be no defenestration at the microscopic level.

While the ^{87}Rb Atoms are magnetically trapped at their $|F = 2,\, m_F = 2\rangle$ state, the level spacing of adjustment Zeeman levels due to the Ioffe field will be 0.7 MHz/G (at first order). Double-wells can be created by raising an energy barrier mainly along the center of the cloud in its transverse direction. Such double-well potential can be created by coupling the atoms (which will be at the $|2,\, 2\rangle$ state) with σ_+ rf field. The field should be red detuned enough ($\Delta \sim -200\,\mathrm{kHz}$ at $1\,\mathrm{G}$) from the actual transition frequency between $|2,\, 2\rangle$ and $|2,\, 1\rangle$ Zeeman states so there would be very low transition probability between the states $\left(P_{max} = \frac{\Omega^2}{\Omega^2+\Delta^2}\right)$, where Ω is the Rabi frequency. The amplitude of the trapping potential is very steep in the radii direction, so the effective energy separation between the levels is steeply increasing as well; we use this phenomenon since the rf coupling decreases with detuning almost quadratically. The effective adiabatic potential V_{eff} at the position $\mathbf{r}$ that governors the interaction in the dressed state picture is [29]

$$V_{eff}(\mathbf{r}) = \mu_\mathrm{B}\, m_F\, g_F \sqrt{\left(\frac{\beta_+}{2}\right)^2 + \left(B_Z - \frac{\hbar\,\omega_{RF}}{\mu_\mathrm{B}\, g_F}\right)^2}. \tag{6.18}$$

Here μ_B is the Bohr magneton, m_F is the magnetic quantum number of the state, g_F is the Landé factor, B_Z is the amplitude of the static trapping field, ω_{rf} is the

frequency of the rf field. β_+ is the σ_+ component amplitude of the rf field in relation to the local direction of the static trapping field. The direction dependence between B_Z and β_+ implies both the polarization and the actual formation of the double-well potential.

In our experiment it is also important to split the cloud in a way that the minimum energy along its center will be constant in the three branches of the Y shape. So the first thing we should consider is how to keep not only the magnetic field at the trap minimum as constant as possible, but also keeping the cloud at a constant height so there will be no differences in potential energy due to gravity. The shape of the splitting as seen from the effective potential is related to the relation between the direction of the quadrupole trapping magnetic field and the direction of the **k** vector of the rf field (Fig. 6.6 d). To create the wanted splitting direction under the central trapping Z wire we need the rf $\hat{\mathbf{k}}$ vector to be in the y direction. This direction of the $\hat{\mathbf{k}}$ vector can be achieved by applying equally powered counter-propagating currents in each parallel ⊔-shaped structures on the chip surface (see Fig. 6.6). The time-dependent splitting or "unzipping" is produced by increasing the currents in each of the parallel structures one after the other in a sequence such that a running rf dressed potential is created. One major problem with such a technique is that due to the coupling between the atoms and rf dressed potential, although minimal, the ground state energy of the "arms" will be a bit higher than the ground state energy of the "root"; this can be compensated for in two ways (Fig. 6.6 e-h). One is to dynamically tilt the cloud upwards using the bias field in its longitudinal direction, while the other is by applying low alternating current in each of the ⊔-structures that lift the potential minimum along the cloud. We have chosen the latter.

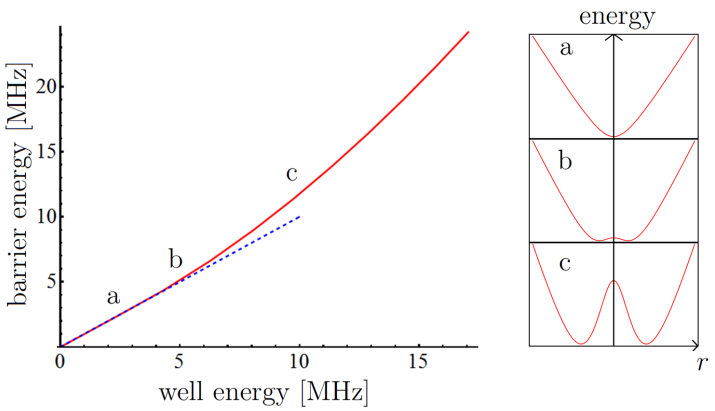

Figure 6.5: The energy of the barrier as a function of the well minimal energy. For low currents (a) The cloud doesn't split; the min and max energies increase simultaneously (see fitted dashed line); (b) Split cross-over point; (c) Once the split starts, the max energy increases non-linearly compared to the well bottom.

In Fig. 6.5 one can see the energy at the top of the barrier as a function of the minimum energy point. Until the cloud splits the energy difference is naturally

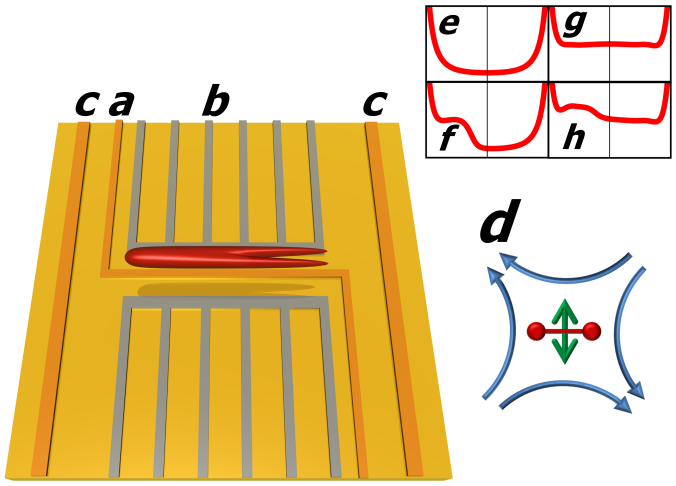

Figure 6.6: Left: Figure of the atom chip with the Y-split cloud hovering above. (a) The Z trap micro-structure. (b) The ⊔ rf carrying micro-structure. (c) Current carrying micro-structure used to reduce the cloud banding. **(d)** Blue: the d.c. magnetic trapping field; Green: the rf field k vector; Red: the cloud splitting direction. **(e-h)** Center trap energy vs. x; (e) The energy without rf. (f) The energy with current in the first two ⊔ structures; this can cause a reduced density in the split part compared to the unsplit part. (g) Low current is applied in all rf structures, the cloud is split but tunneling occurs. (h) Unzip the cloud by removing the tunneling.

zero, but as the split occurs the barrier increases faster than the minimum energy point. We wish to utilize this effect to prevent differences in energy between the split and unsplit parts of the cloud. The way to do so is by applying high enough rf field in all the ⊔ structures so that the cloud will be semi-split, but low enough so tunneling will occur. By allowing tunneling the phase will be fixed (see Fig. 6.6 g), then the extra energy needed to prevent tunneling, and split the cloud, almost won't increase the trap minimum. There will be an even number of minimum energy points along the could length (see inset h).

After the split, as seen in Fig. 6.6, the cloud will be released from the magnetic trap and freely expand. The two "legs" of the Y-junction will interfere as explained by Bistritzer et al. [144]. To get the full interference pattern of such dynamic splitting, one should image the condensate from below parallel to the plane of the chip after sufficient time of flight. A very good imaging technique that allows single atom resolution from below after some time of flight is the "light sheet imaging" technique, which was presented by R. Bucker et. al. in 2009 [67]. From the interference pattern one can build a density correlation function $g_1(x1, x2)$, which will be analyzed. In the theoretical section the coherence is $g_1(L_s, x')$, where L_s is the split part length, and $0 < x' < L_s$.

6.3 Summary

In this chapter we presented a new chip design that allows dynamic splitting of a cold anisotropic atomic sample. The range of possibilities with such a chip is very broad and interesting. The first proposed use for such a chip is as a tool for a gravitational analogous model using atomic samples. Another interesting use for such a chip is to create unusual spatial forms of atoms such as elliptic rings (see Fig. 6.7) or spacial dynamically changing shapes.

In this chapter we proposed a new framework system to investigate the DCE, where quasi-particle excitations are created as a result of a barrier moment in a Y-junction shaped BEC. The possibility to engineer the unzipping trajectory gives rise to many types of measurements as explained. A theory for the coherence properties of ultra-cold atomic samples has developed and is ready to be fitted to upcoming experimental results.

We want to thank again Serena Fagnocchi, Ehud Altman, Susanne Pielawa, and Eugene Demler for their time and efforts.

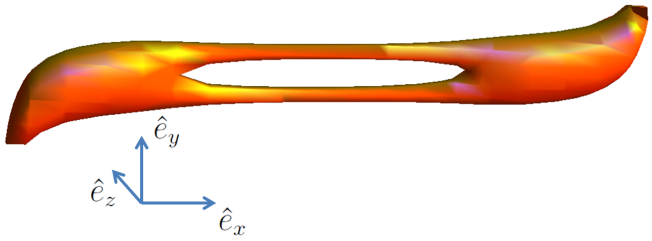

Figure 6.7: A simulation of elliptic ring type BEC that can be created by applying rf field from the center ⊔ rf carrying micro-structures.

Outlook

This thesis describes experiments on the quantum nature of cold atoms. Starting with optimization of absorption imaging (chapter 2), we have calculated and measured the quantum noise in absorption imaging as a function of light intensity and atomic column density. Knowing the noise and atomic density we have developed a method to optimize the light intensity as a function of the atomic density. Absorption imaging is our main tool in cold atom experiments; therefore high SNR in imaging has great importance. A change in magnitude as shown can increase the reliability of both precise measurement type of experiments and imaging of extremely dense atomic clouds such as in in situ imaging. As part of this work using 10^8 ^{87}Rb atoms in a MOT we have sampled a large range of density and intensities and established our theoretical hypothesis. Further research can be done in two directions, first checking if while using detuned light the formalism still holds experimentally. The second direction relates to image mimicking of dense and small objects, such as in situ clouds where the effective pixel size (at the object plane) is larger than the sampled cloud. In such a scenario some of the light bypasses the sides of the cloud and the measured absorption does not reflect the real atomic density. To overcome this problem in chapter 5 we have used two techniques, we either let the cloud fall for very short TOF, or heated the cloud using the imaging light. Both ways expand the atomic cloud to the effective pixel size where the first should more precise in 1d type of experiments, since the cloud expands mainly along its radial axis in a short time. A full analysis is important to improve the accuracy of in situ experiments.

A one-dimensional quasi-BEC was formed at the BGU2 setup as part of a joint project. First we loaded a BEC at the cross-point between Thomas Fermi and quasi-1d BEC, where the radial motion is not completely frozen. Our main indicator was that the in situ density profile was almost homogenous, where other factors such as χ indicated a bit below the cross-over point χ_{cross} (see sec. 3.1.5). In this region the evolution during time of flight of the longitudinal line density is mainly affected by two related factors. The first is phase fluctuations in the order parameter that destroy the off diagonal long-range order, and the second is the mean free energy that depresses in situ density fluctuations. As the atomic line density decreases, the mean free energy decreases; as a result the density profile is not homogenous anymore. In chapter 3 we have measured the variance in atom number as a function of the mean atomic density for different times of flight. The evolution of the atomic density along its quantization axis is shown in Fig. 3.8 for small range of values. We suggest performing a larger scale experiment for clouds at χ above and below the $3d/1d$ cross-over region. In such an experiment we could measure and develop a general

understanding of the TOF evolution of the density profile along the quantization axis. Such a theory will incorporate the contribution interaction strength, coherence Length, and atomic line density of the evolution of density during time of flight.

In chapter 5 we measured the effect of interaction quench on 1d Bose gas. The experimental data showed a clear change in the atomic variance as a function of the mean atom number for different dark times before and after interaction quench. In Fig. 5.2 the experimental data shows a clear signature of the prethermalization process since there was almost no change in the variance before and $2\,ms$ after the quench, where at a later time a significant change is seen. In the Fourier plane analysis of the first two there is a change that is not seen in the variance (see Fig. 5.3). At a later measurement we checked the time evolution using a different imaging technique that gave clearer results (see Fig. 5.4). We have assumed that the variance as a function of dark time after interaction quench should change its value as a dump oscillator. We suggest repeating the experiment with a variety of dark times. This measurement can teach us a great deal about the mechanism behind prethermalization.

In the last chapter, "Zippers and Quantum Mechanics: A proposal for measuring the dynamical Casimir effect" (chapter 6), we suggested a new type of experiment that will connect atomic physics with quantum fields theory. The proposed experiment treats a 1d quasi-BEC as 1d Minkowski space where phase modes are treated as vacuum modes. This type of experiment creates a non-trivial bridge between the quantum field theory community and the cold atoms community. Such a connection can bring new ideas and understanding for both communities.

Last but not least is the ability to create non-trivial geometries using our newly designed atom chip (see Fig. 6.6). The ability to create spatially flexible time-dependent rf dressed potentials can open new fields of opportunities such as time-dependent 1d ring BEC, measurements of super currents in 1d by applying perturbation on an oval ring, and looking at the effect of tunneling, using interference pictures. Other geometries could mimic Josephson tunneling by creating a narrow passage between two separate BECs and measure the differential phase between the clouds as function of dark time and geometry. Many more ideas can be utilized using this versatile chip that waits to be explored.

Bibliography

[1] William D Phillips. Nobel Lecture: Laser cooling and trapping of neutral atoms. *Reviews of Modern Physics*, 70(3):721–741, July 1998.

[2] Steven Chu. Nobel Lecture: The manipulation of neutral particles. *Reviews of Modern Physics*, 70(3):685–706, July 1998.

[3] M H Anderson, J R Ensher, M R Matthews, C E Wieman, and E A Cornell. Observation of bose-einstein condensation in a dilute atomic vapor. *Science*, 269(5221):198–201, 1995.

[4] C C Bradley, C A Sackett, J J Tollett, and R G Hulet. Evidence of Bose-Einstein Condensation in an Atomic Gas with Attractive Interactions. *Phys. Rev. Lett.*, 75(9):1687–1690, August 1995.

[5] K. B. Davis, M. O. Mewes, M. R. Andrews, N. J. van Druten, D. S. Durfee, D. M. Kurn, and W. Ketterle. Bose-Einstein Condensation in a Gas of Sodium Atoms. *Phys. Rev. Lett.*, 75(22):3969–3973, 1995.

[6] F Schreck, L Khaykovich, K L Corwin, G Ferrari, T Bourdel, J Cubizolles, and C Salomon. Quasipure Bose-Einstein condensate immersed in a Fermi sea. *Physical Review Letters*, 87(8):4, 2001.

[7] S N Bose. Plancks Gesetz und Lichtquantenhypothese. *Zeitschrift Für Physik*, 26(1):178–181, 1924.

[8] A. Einstein. Quantentheorie des einatomigen idealen gases. *Sitzungsber. Preuss. Akad. Wiss., Bericht*, (22):261–267, 1924.

[9] EC-FET. iSense -Integrated Quantum Sensors.

[10] Immanuel Bloch. Ultracold quantum gases in optical lattices. *Nature Physics*, 1(1):23–30, 2005.

[11] D Jaksch, C Bruder, J I Cirac, C W Gardiner, and P Zoller. Cold bosonic atoms in optical lattices. *Physical Review Letters*, 81(15):4, 1998.

[12] Michael Albiez, Rudolf Gati, Jonas Foelling, Stefan Hunsmann, Matteo Cristiani, and Markus K Oberthaler. Direct Observation of Tunneling and Nonlinear Self-Trapping in a single Bosonic Josephson Junction. *Physical Review Letters*, 95(1):1–4, 2004.

[13] M Bartenstein, A Altmeyer, S Riedl, S Jochim, C Chin, J Hecker Denschlag, and R Grimm. Crossover from a molecular Bose-Einstein condensate to a degenerate Fermi gas. *Physical Review Letters*, 92(12):5, 2004.

[14] C Chin, M Bartenstein, A Altmeyer, S Riedl, S Jochim, J Hecker Denschlag, and R Grimm. Observation of the pairing gap in a strongly interacting Fermi gas. *Science*, 305(5687):1128–1130, 2004.

[15] M W Zwierlein, J R Abo-Shaeer, A Schirotzek, C H Schunck, and W Ketterle. Vortices and Superfluidity in a Strongly Interacting Fermi Gas. *Nature*, 435(7045):1047–1051, 2005.

[16] J Berges, Sz Borsanyi, and C Wetterich. Prethermalization. *Phys. Rev. Lett.*, 93(14):4, 2004.

[17] Ryan Barnett, Anatoli Polkovnikov, and Mukund Vengalattore. Prethermalization in quenched spinor condensates. *Physical Review A*, 84(2):7, 2010.

[18] L Mathey and A Polkovnikov. Light cone dynamics and reverse Kibble-Zurek mechanism in two-dimensional superfluids following a quantum quench. *Physical Review A*, 81(3):14, 2009.

[19] Takuya Kitagawa, Adilet Imambekov, Jörg Schmiedmayer, and Eugene Demler. The dynamics and prethermalization of one-dimensional quantum systems probed through the full distributions of quantum noise. *New Journal of Physics*, 13(7):073018, July 2011.

[20] Takuya Kitagawa, Susanne Pielawa, Adilet Imambekov, Jörg Schmiedmayer, Vladimir Gritsev, and Eugene Demler. Ramsey interference in one dimensional systems: The full distribution function of fringe contrast as a probe of many-body dynamics. *Physical Review Letters*, 104(25):5, 2009.

[21] M Gring, M Kuhnert, T Langen, T Kitagawa, B Rauer, M Schreitl, I Mazets, D Adu Smith, E Demler, and J Schmiedmayer. Relaxation and Prethermalization in an Isolated Quantum System. *Science*, 337(6100):1318–1322, September 2012.

[22] Xiao Yin and Leo Radzihovsky. Quench dynamics of a strongly interacting resonant Bose gas. *Phys. Rev. A*, 88(6):63611, December 2013.

[23] Toshiya Kinoshita, Trevor Wenger, and David S Weiss. A quantum Newton's cradle. *Nature*, 440(7086):900–3, April 2006.

[24] Iacopo Carusotto, Roberto Balbinot, Alessandro Fabbri, and Alessio Recati. Density correlations and dynamical Casimir emission of Bogoliubov phonons in modulated atomic Bose-Einstein condensates. pages 1–12.

[25] Iacopo Carusotto, Serena Fagnocchi, Alessio Recati, Roberto Balbinot, and Alessandro Fabbri. Numerical observation of Hawking radiation from acoustic black holes in atomic Bose-Einstein condensates. *New Journal of Physics*, 10(10):103001, 2008.

[26] Ron Folman and Peter Krüger. Microscopic atom optics: from wires to an atom chip. 356:1–47, 2002.

[27] József Fortágh and Claus Zimmermann. Magnetic microtraps for ultracold atoms. *Reviews of Modern Physics*, 79(1):235–289, February 2007.

[28] Peter Krüger. *Coherent matter waves near surfaces*. PhD thesis, University of Heidelberg, 2004.

[29] T. Schumm, S. Hofferberth, L. M. Andersson, S. Wildermuth, S. Groth, I. Bar-Joseph, J. Schmiedmayer, and P. Krüger. Matter-wave interferometry in a double well on an atom chip. *Nature Physics*, 1(1):57–62, September 2005.

[30] Anton Piccardo-Selg. *PhD. Thesis*. PhD thesis, The university of Nottingham, 2013.

[31] S. N. Bose. Planck's law and the light quantum hypothesis (English). *Journal of Astrophysics and Astronomy*, 15:3–7, 1994.

[32] A. Einstein. Quantentheorie des einatomigen idealen gases. ii. *Sitzungsber. Preuss. Akad. Wiss., Bericht*, 1:3–14, 1925.

[33] Claude N Cohen Tannoudji. Nobel Lecture: Manipulating atoms with photons. *Reviews of Modern Physics*, 70(3):707–719, July 1998.

[34] K B Davis, M O Mewes, and W Ketterle. An analytical model for evaporative cooling of atoms. *Appl Phys B*, 60(2-3):155, 1995.

[35] Wolfgang Ketterle and N.J. Van Druten. Evaporative Cooling of Trapped Atoms. *Advances In Atomic, Molecular, and Optical Physics*, 37:181–236, 1996.

[36] H J Metcalf and P Van Der Straten. *Laser Cooling and Trapping*, volume 39 of *Graduate Texts in Contemporary Physics*. Springer, 1999.

[37] H J Metcalf and P van der Straten. Laser cooling and trapping of atoms. *J. Opt. Soc. Am. B*, 20(5):887–908, May 2003.

[38] R Folman, P Krüger, D Cassettari, B Hessmo, T Maier, and J Schmiedmayer. Controlling cold atoms using nanofabricated surfaces: Atom chips. *Physical Review Letters*, 84(20):4749, 2000.

[39] J. Reichel. Microchip traps and Bose-Einstein condensation. *Appl. Phys. B*, 75:469, 2003.

[40] SAES getters. Alkali Metal Dispensers. Technical report, 2007.

[41] William D. Phillips Steven Chu, Claude Cohen-Tannoudji. The Nobel Prize in Physics 1997, 1997.

[42] J. Dalibard and C. Cohen-Tannoudji. Laser cooling below the Doppler limit by polarization gradients: simple theoretical models. *Journal of the Optical Society of America B*, 6(11):2023, November 1989.

[43] Evan Salim and Heather Lewandowski. Laser Cooling and Trapping for Advanced Teaching Laboratories. Technical report, JILA NISTCU; ColdQuanta Inc., 2012.

[44] Luciano Majorana, Ettore and Maiani. *Ettore Majorana Scientific Papers - A symmetric theory of electrons and positrons*. Springer Berlin Heidelberg, 2006.

[45] David E Pritchard. Cooling Neutral Atoms in a Magnetic Trap for Precision Spectroscopy. *Physical Review Letters*, 51(15):1336–1339, 1983.

[46] Piet O Schmidt, Sven Hensler, Jörg Werner, Thomas Binhammer, Axel Görlitz, and Tilman Pfau. Doppler cooling of an optically dense cloud of trapped atoms. *Journal Of The Optical Society Of America B Optical Physics*, 20(5):8, 2002.

[47] London Fröhlich. The λ phenomenon of liquid helium and the bose-einstein degeneracy. *Nature*, 141:643–644, 1938.

[48] London Fröhlich. On the Bose-Einstein Condensation. *Physical Review*, 54(11):947–954, 1938.

[49] Eric A. Cornell. Nobel Lecture: Bose-Einstein Condensation in a Dilute Gas; The First 70 Years and Some Recent Experiments, 2012.

[50] Wolfgang Ketterle. Nobel Lecture: When Atoms Behave as Waves: Bose-Einstein Condensation and the Atom Laser, 2012.

[51] Carl E. Wieman. Nobel Lecture: Bose-Einstein Condensation in a Dilute Gas; The First 70 Years and Some Recent Experiments, 2012.

[52] Oj Luiten, Mw Reynolds, and Jt Walraven. Kinetic theory of the evaporative cooling of a trapped gas. *Physical Review A*, 53(1):381–389, 1996.

[53] A. Griffin, D. W. Snoke, and S. Stringari. *Bose-Einstein Condensation*. 1996.

[54] Lev Pitaevskii and Sandro Stringari. *Bose-Einstein Condensation*, volume 116. Oxford University Press, 2003.

[55] Dmitry Budker, Derek Kimball, and David DeMille. *Atomic physics An exploration through problems and solutions*. Oxford University Press, 2008.

[56] H Ott, J Fortagh, G Schlotterbeck, A Grossmann, and C Zimmermann. Bose-Einstein Condensation in a Surface Micro Trap. *Physical Review Letters*, 87(23):4, 2001.

[57] W Hänsel, P Hommelhoff, T W Hänsch, and J Reichel. Bose-Einstein condensation on a microelectronic chip. *Nature*, 413(6855):498–501, 2001.

[58] S Schneider, A Kasper, Ch Vom Hagen, M Bartenstein, B Engeser, T Schumm, I Bar-Joseph, R Folman, L Feenstra, and J Schmiedmayer. Bose-Einstein Condensation in a simple Microtrap. *Physical Review A*, 67(2):4, 2002.

[59] M. P. A. Jones. *Bose-Einstein Condensation on an Atom Chip*. PhD thesis, University of Sussex, 2002.

[60] C G Townsend, N H Edwards, C J Cooper, K P Zetie, C J Foot, A M Steane, P Szriftgiser, H Perrin, and J Dalibard. Phase-space density in the magneto-optical trap. *Physical Review A*, 52(2):1423–1440, 1995.

[61] Herman Feshbach. Unified theory of nuclear reactions. *Annals of Physics*, 5(4):357–390, 1958.

[62] Thomas Volz, Stephan Dürr, Sebastian Ernst, Andreas Marte, and Gerhard Rempe. Characterization of elastic scattering near a Feshbach resonance in 87Rb. *Physical Review A*, 68(1):1–4, July 2003.

[63] P S Julienne, F H Mies, E Tiesinga, and C J Williams. Collisional Stability of Double Bose Condensates. *Physical Review Letters*, 78(10):1880–1883, 1997.

[64] C. J. Pethick and Smith Henrik. *Bose-Einstein Condensation in Dilute Gases*. Cambridge University Press, 2002.

[65] David A. Smith, Simon Aigner, Sebastian Hofferberth, Michael Gring, Mauritz Andersson, Stefan Wildermuth, Peter Krüger, Stephan Schneider, Thorsten Schumm, and Jörg Schmiedmayer. Absorption imaging of ultracold atoms on atom chips. *Optics Express*, 19(9):8471, April 2011.

[66] Shimon Machluf. *Building a BEC on an atom chip apparatus*. PhD thesis, Ben Gurion, 2009.

[67] R Bücker, a Perrin, S Manz, T Betz, Ch Koller, T Plisson, J Rottmann, T Schumm, and J Schmiedmayer. Single-particle-sensitive imaging of freely propagating ultracold atoms. *New Journal of Physics*, 11(10):103039, October 2009.

[68] Sony. Sony ICX098BL CCD Image Sensor.

[69] Super-HAD-CCD. Sony ICX625 CCD Image Sensor.

[70] M Pappa, P C Condylis, G O Konstantinidis, V Bolpasi, a Lazoudis, O Morizot, D Sahagun, M Baker, and W von Klitzing. Ultra-sensitive atom imaging for matter-wave optics. *New Journal of Physics*, 13(11):115012, November 2011.

[71] J. Esteve, J.-B. Trebbia, T. Schumm, a. Aspect, C. Westbrook, and I. Bouchoule. Observations of Density Fluctuations in an Elongated Bose Gas: Ideal Gas and Quasicondensate Regimes. *Physical Review Letters*, 96(13):1–4, April 2006.

[72] Y. Jiang, O. Jedrkiewicz, S. Minardi, P. DiTrapani, a. Mosset, E. Lantz, and F. Devaux. Retrieval of spatial shot-noise in the full dynamic range of calibrated CCD cameras. *The European Physical Journal D - Atomic, Molecular and Optical Physics*, 22(3):521–526, March 2003.

[73] Franco Dalfovo, Stefano Giorgini, Lev P Pitaevskii, and Sandro Stringari. Theory of Bose-Einstein condensation in trapped gases. *Reviews of Modern Physics*, 71(3):463–512, 1999.

[74] M R Andrews, C G Townsend, H J Miesner, D S Durfee, D M Kurn, and W Ketterle. Observation of Interference Between Two Bose Condensates. *Science*, 275(5300):637–641, 1997.

[75] E W Hagley, L Deng, M Kozuma, M Trippenbach, Y B Band, M Edwards, M Doery, P S Julienne, K Helmerson, S L Rolston, and W D Phillips. Measurement of the Coherence of a Bose-Einstein Condensate. *Physical Review Letters*, 83(16):3112–3115, 1999.

[76] J Stenger, S Inouye, A P Chikkatur, D M Stamper-Kurn, D E Pritchard, and W Ketterle. Bragg spectroscopy of a Bose-Einstein condensate. *Physical Review Letters*, 82(23):4, 1999.

[77] DS Petrov, GV Shlyapnikov, and JTM Walraven. Regimes of quantum degeneracy in trapped 1D gases. *Physical review letters*, (October):3745–3749, 2000.

[78] S. Dettmer, D. Hellweg, P. Ryytty, J. Arlt, W. Ertmer, K. Sengstock, D. Petrov, G. Shlyapnikov, H. Kreutzmann, L. Santos, and M. Lewenstein. Observation of Phase Fluctuations in Elongated Bose-Einstein Condensates. *Physical Review Letters*, 87(16):14–17, October 2001.

[79] P Hohenberg. Existence of Long-Range Order in One and Two Dimensions. *Physical Review*, 158(2):383–386, 1967.

[80] N D Mermin and H Wagner. Absence of Ferromagnetism or Antiferromagnetism in One- or Two-Dimensional Isotropic Heisenberg Models. *Physical Review Letters*, 17(22):1133–1136, 1966.

[81] Zoran Hadzibabic, Peter Krüger, Marc Cheneau, Baptiste Battelier, and Jean Dalibard. Berezinskii-Kosterlitz-Thouless crossover in a trapped atomic gas. *Nature*, 441(7097):1118–21, June 2006.

[82] D Hellweg, S Dettmer, P Ryytty, J J Arlt, W Ertmer, K Sengstock, D S Petrov, G V Shlyapnikov, H Kreutzmann, L Santos, and M Lewenstein. Phase fluctuations in Bose Einstein condensates. *Applied Physics B*, 73(8):781–789, 2001.

[83] S. Richard, F. Gerbier, J. Thywissen, M. Hugbart, P. Bouyer, and a. Aspect. Momentum Spectroscopy of 1D Phase Fluctuations in Bose-Einstein Condensates. *Physical Review Letters*, 91(1):10–13, July 2003.

[84] S Hofferberth, I Lesanovsky, B Fischer, T Schumm, and J Schmiedmayer. Non-equilibrium coherence dynamics in one-dimensional Bose gases. *Nature*, 449(7160):324–7, September 2007.

[85] S Stringari. Dynamics of Bose-Einstein condensed gases in highly deformed traps. *Physical Review A*, 58(3):2385, 1998.

[86] Elliott H Lieb and Werner Liniger. Exact Analysis of an Interacting Bose Gas. I. The General Solution and the Ground State. *Physical Review*, 130(4):1605–1616, 1963.

[87] Lewi Tonks. The Complete Equation of State of One, Two and Three-Dimensional Gases of Hard Elastic Spheres. *Physical Review*, 50(10):955–963, 1936.

[88] M Girardeau. Relationship between Systems of Impenetrable Bosons and Fermions in One Dimension. *Journal of Mathematical Physics*, 1(6):516, 1960.

[89] D. Petrov. *Bose-Einstein Condensation in Low-Dimensional Trapped Gases*. PhD thesis, 2003.

[90] V N Popov, J Niederle, and L Hlavaty. *Functional Integrals in Quantum Field Theory and Statistical Physics*. Mathematical Physics and Applied Mathematics Series. Springer London, Limited, 2001.

[91] F Gerbier. Quasi-1D Bose-Einstein condensates in the dimensional crossover regime. *Europhysics Letters (EPL)*, 66(6):771–777, June 2004.

[92] Chiara Menotti and Sandro Stringari. Collective oscillations of a one-dimensional trapped Bose-Einstein gas. *Physical Review A*, 66(4):1–6, 2002.

[93] E Lucioni, B Deissler, L Tanzi, G Roati, M Modugno, M Zaccanti, M Larcher, F Dalfovo, M Inguscio, and G Modugno. Observation of subdiffusion of a disordered interacting system. *Physical Review Letters*, 106(23):8, 2010.

[94] M Greiner, C A Regal, J T Stewart, and D S Jin. Probing pair-correlated fermionic atoms through correlations in atom shot noise. *Physical Review Letters*, 94(11):110401, 2005.

[95] Simon Fölling, Fabrice Gerbier, Artur Widera, Olaf Mandel, Tatjana Gericke, and Immanuel Bloch. Spatial quantum noise interferometry in expanding ultracold atom clouds. *Nature*, 434(7032):481–4, March 2005.

[96] R Hanbury Brown and R Q Twiss. Interferometry of the intensity fluctuation in light I. *Proc Roy Soc London Series A*, 242(1230):300, 1957.

[97] R Hanbury Brown and R Q Twiss. Interferometry of intensity fluctuations in light II. *Proceedings of the Royal Society of London Series A Mathematical and Physical Sciences*, 243(1234):291–319, 1958.

[98] Anton Öttl, Stephan Ritter, Michael Köhl, and Tilman Esslinger. Correlations and Counting Statistics of an Atom Laser. *Physical Review Letters*, 95(9):4–7, August 2005.

[99] M Naraschewski and R J Glauber. Spatial coherence and density correlations of trapped Bose gases. *Physical Review A*, 59(6):25, 1998.

[100] J.-B. Trebbia, J. Esteve, C. Westbrook, and I. Bouchoule. Experimental Evidence for the Breakdown of a Hartree-Fock Approach in a Weakly Interacting Bose Gas. *Physical Review Letters*, 97(25):250403, December 2006.

[101] S. Cockburn, a. Negretti, N. Proukakis, and C. Henkel. Comparison between microscopic methods for finite-temperature Bose gases. *Physical Review A*, 83(4):043619, April 2011.

[102] S Tomonaga. Remarks on Bloch's Method of Sound Waves applied to Many-Fermion Problems. *Progress of Theoretical Physics*, 5(4):544–569, 1950.

[103] M a Cazalilla. Bosonizing one-dimensional cold atomic gases. *Journal of Physics B: Atomic, Molecular and Optical Physics*, 37(7):S1–S47, April 2004.

[104] F D M Haldane. Effective Harmonic-Fluid Approach to Low-Energy Properties of One-Dimensional Quantum Fluids. *Physical Review Letters*, 47(25):1840–1843, 1981.

[105] F D M Haldanef. Luttinger liquid theory of one-dimensional quantum fluids: I . Properties of the Luttinger model and their extension to the general 1D interacting spinless Fermi gas. *Physics*, 14(September):2585–2609, 1981.

[106] A Recati, P O Fedichev, W Zwerger, J Von Delft, and P Zoller. Atomic quantum dots coupled to a reservoir of a superfluid Bose-Einstein condensate. *Physical Review Letters*, 94(4):040404, 2005.

[107] M. Cazalilla. Effect of Suddenly Turning on Interactions in the Luttinger Model. *Physical Review Letters*, 97(15):1–4, October 2006.

[108] A. Imambekov, I. Mazets, D. Petrov, V. Gritsev, S. Manz, S. Hofferberth, T. Schumm, E. Demler, and J. Schmiedmayer. Density ripples in expanding low-dimensional gases as a probe of correlations. *Physical Review A*, 80(3):1–14, September 2009.

[109] Marcus Kollar, F Alexander Wolf, and Martin Eckstein. Generalized Gibbs ensemble prediction of prethermalization plateaus and their relation to nonthermal steady states in integrable systems. *Phys. Rev. B*, 84(5):54304, August 2011.

[110] Anatoli Polkovnikov, Krishnendu Sengupta, Alessandro Silva, and Mukund Vengalattore. Colloquium: Nonequilibrium dynamics of closed interacting quantum systems. *Reviews of Modern Physics*, 83(3):863–883, August 2011.

[111] P Bouyer and A Aspect. Density Modulations in an Elongated BEC Released from a Disordered Potential: What Can We Learn? pages 1–4, 2008.

[112] H. B. G. Casimir. On the attraction between two perfectly conducting plates. *Proc. Kon. Nederland. Akad. Wetensch.*, B51(793), 1948.

[113] S W Hawking. Black hole explosions? *Nature*, 248(5443):30–31, 1974.

[114] Marlan O Scully and M Suhail Zubairy. *Quantum Optics*. Cambridge University Press, 1 edition, September 1997.

[115] Walter Greiner and Stefan Schramm. Resource Letter QEDV-1: The QED vacuum. *American Journal of Physics*, 76(6):509, 2008.

[116] Gerald T Moore. Quantum Theory of the Electromagnetic Field in a Variable-Length One-Dimensional Cavity. *Journal of Mathematical Physics*, 11(9):2679, 1970.

[117] C Braggio, G Bressi, G Carugno, C Del Noce, G Galeazzi, A Lombardi, A Palmieri, G Ruoso, and D Zanello. A novel experimental approach for the detection of the dynamic Casimir effect. *Europhysics Letters*, 70(6):4, 2004.

[118] E Yablonovitch. Accelerating reference frame for electromagnetic waves in a rapidly growing plasma: Unruh-Davies-Fulling-DeWitt radiation and the nonadiabatic Casimir effect. *Physical Review Letters*, 62(15):1742–1745, 1989.

[119] Yu. E. Lozovik, V. G. Tsvetus, and E. A. Vinogradov. Femtosecond parametric excitation of electromagnetic field in a cavity. *JETP Lett.*, 61(723), 1995.

[120] V V Dodonov, A B Klimov, and D E Nikonov. Quantum phenomena in nonstationary media. *Phys. Rev. A*, 47(5):4422–4429, May 1993.

[121] Simone De Liberato, Cristiano Ciuti, and Iacopo Carusotto. Quantum vacuum radiation spectra from a semiconductor microcavity with a time-modulated vacuum Rabi frequency. *Physical Review Letters*, 98(10):103602, 2006.

[122] G Günter, A A Anappara, J Hees, A Sell, G Biasiol, L Sorba, S De Liberato, C Ciuti, A Tredicucci, A Leitenstorfer, and R Huber. Sub-cycle switch-on of ultrastrong light-matter interaction. *Nature*, 458(7235):178–181, 2009.

[123] J R Johansson, G Johansson, C M Wilson, and Franco Nori. Dynamical Casimir effect in a superconducting coplanar waveguide. *Physical Review Letters*, 103(14):4, 2009.

[124] J R Johansson, G Johansson, C M Wilson, and Franco Nori. Dynamical Casimir effect in superconducting microwave circuits. *Phys. Rev. A*, 82(5):52509, November 2010.

[125] C M Wilson, T Duty, M Sandberg, F Persson, V Shumeiko, and P Delsing. Photon generation in an electromagnetic cavity with a time-dependent boundary. *Physical Review Letters*, 105(23):5, 2010.

[126] P D Nation, J R Johansson, M P Blencowe, and Franco Nori. Colloquium: Stimulating uncertainty: Amplifying the quantum vacuum with superconducting circuits. *Rev. Mod. Phys.*, 84(1):1–24, January 2012.

[127] C M Wilson, G Johansson, A Pourkabirian, J R Johansson, T Duty, F Nori, and P Delsing. Observation of the Dynamical Casimir Effect in a Superconducting Circuit. *Nature*, 479(7373):18, 2010.

[128] V. V. Dodonov. Nonstationary Casimir Effect and analytical solutions for quantum fields in cavities with moving boundaries. *Advances*, 0(1):64, 2001.

[129] V. V. Dodonov and A. V. Dodonov. Quantum harmonic oscillator and nonstationary Casimir effect. *Journal of Russian Laser Research*, 26(445), 2005.

[130] V V Dodonov. Current status of the dynamical Casimir effect. *Physica Scripta*, 82(3):38105, 2010.

[131] M. Bordag, U. Mohideen, and V.M. Mostepanenko. New developments in the Casimir effect, 2001.

[132] Alejandro W. Rodriguez, Federico Capasso, and Steven G. Johnson. The Casimir effect in microstructured geometries, 2011.

[133] R. Jaffe. Casimir effect and the quantum vacuum, 2005.

[134] L Rizzuto, R Passante, and F Persico. Nonlocal properties of dynamical three-body Casimir-Polder forces. *Physical review letters*, 98(24):240404, 2007.

[135] Astrid Lambrecht, Marc-Thierry Jaekel, and Serge Reynaud. Motion Induced Radiation from a Vibrating Cavity. *Physical Review Letters*, 77(4):4, 1996.

[136] Michael Uhlmann, Günter Plunien, Ralf Schützhold, and Gerhard Soff. Resonant cavity photon creation via the dynamical Casimir effect. *Physical review letters*, 93(19):193601, 2004.

[137] Astrid Lambrecht. Electromagnetic pulses from an oscillating high-finesse cavity: possible signatures for dynamic Casimir effect experiments. *Journal of Optics B Quantum and Semiclassical Optics*, 7(3):S3, 2005.

[138] J.-C. Jaskula, G. B. Partridge, M. Bonneau, R. Lopes, J. Ruaudel, D. Boiron, and C. I. Westbrook. Acoustic Analog to the Dynamical Casimir Effect in a Bose-Einstein Condensate. *Physical Review Letters*, 109:220401, 2012.

[139] N.D. Birrel and P.C.W. Davies. *Quantum fields in curved spaces*. Cambridge University Press, 1982.

[140] Pasi Lähteenmäki, G S Paraoanu, Juha Hassel, and Pertti J Hakonen. Dynamical Casimir effect in a Josephson metamaterial. *Proceedings of the National Academy of Sciences of the United States of America*, 110(11):4234–4238, 2013.

[141] Alexander D Cronin, Jörg Schmiedmayer, and David E Pritchard. Optics and interferometry with atoms and molecules. *Rev. Mod. Phys.*, 81(3):1051–1129, July 2009.

[142] Anatoli Polkovnikov, Ehud Altman, and Eugene Demler. Interference between independent fluctuating condensates. *Proceedings of the National Academy of Sciences of the United States of America*, 103(16):6125–9, April 2006.

[143] Robert D Carlitz and Raymond S Willey. Reflections on moving mirrors. *Phys. Rev. D*, 36(8):2327–2335, October 1987.

[144] R Bistritzer and E Altman. Intrinsic dephasing in one-dimensional ultracold atom interferometers. *Proceedings of the National Academy of Sciences of the United States of America*, 104(24):9955–9959, 2007.